With the support of the Erasmus+ Programme of the European Union

Master Thesis
Master of Science
Marine Technology
Hydrodynamics for Ocean Engineering

Modelling Multi-Directional Cyclic Loading on Foundations for Offshore Wind Turbines

Submitted on 21st August 2024

by

John Ekene AKUDORO

Supervisors:

Dr. Christelle N. Abadie
Dr. Ana M. Page

TABLE OF CONTENTS

LIST OF TABLES

LIST OF FIGURES

NOMENCLATURE

General Notations

p	Lateral Soil Reaction
y	Pile Displacement
P_u	Peak Lateral Soil Reaction
y_{50}	Deflection of Pile at 50 % P_u
L	Pile Embedded Length
D	Diameter of Monopile
ϵ^P	Plastic Strain
$\dot{\epsilon}^P$	Plastic Strain Rate
ϵ_r	Strain at Reversal Point
λ	Plastic Multiplier
g	Plastic Potential Function; Acceleration due to Gravity
σ	Stress Tensor
σ_r	Stress at Reversal Point
f	Yield Function
α	Back-stress/ Internal Kinematic Hardening Variable
$\dot{\alpha}$	Back-stress Rate
C	Material Stiffness Constant
d	Dissipation Function
N	Number of Yield Surfaces
r	Continuous Hardening Parameter
H_R	Reference Lateral Force
M_R	Reference Moment
u_R	Reference Displacement
θ_R	Reference Rotation
H_s	Significant Wave Height
T_p	Peak Wave Period
f	Frequency
f_p	Peak Frequency i.e. the Inverse of T_p
γ	Peak Enhancement Factor (3.3 for JONSWAP)
σ_u	Standard deviation of the longitudinal wind speed fluctuations
L_u	Turbulence Length Scale
U	Mean Wind Speed
C_d	Wave Drag Coefficient
C_m	Inertia Coefficient
θ_{wave}	Wave Direction
$S(f)$	JONSWAP Spectrum
$S_d(f, \theta_{wave})$	Directional JONSWAP Spectrum
$S_u(f)$	Kaimal Spectrum

HARM Notations

N_s	Number of Yield Surfaces
k	Hardening Strength
k_n	Yield stress threshold for each spring-slider
k_U	Upper Value of k_n;
H	Hardening Modulus
H_0	Initial Modulus
H_n	Hardening Moduli
ϵ	Total Strain

α_n	Internal Strain Variables (Plastic Strains)
$\dot{\alpha}_n$	Rates of Plastic Strains
α_r	Ratcheting Strain
$\dot{\alpha}_r$	Ratcheting Strain Rate
f	Helmholtz Free Energy
g	Gibbs free energy
$\bar{\chi}_n, \chi_n, \bar{\chi}_r, \chi_r$	Generalized stress/Back-stress for each plastic strain variable
E	Elastic Stiffness
$S()$	Signum Function
R_n	Ratcheting Parameters
R_0	Initial Value of Ratcheting Parameter
c	Ratcheting Constraint
β	Hardening Parameter
β_0	Initial Value of Hardening Parameter
m_r	Ratcheting Exponent
m_s	Stress Exponent

REDWIN Notations

J_2	Deviatoric stress tensor's second invariant
r	Yield Surface Radius
$\boldsymbol{K}$	Elastic Stiffness Matrix
$\boldsymbol{K}^p$	Plastic Stiffness Matrix
K^T, K_T	Tangent Stiffness
K^p, K_p	Hardening Stiffness
S	Hardening Strength
ϵ^e	Elastic Strain
ϵ^p	Plastic Strain
H_x, H_y	Lateral Horizontal Forces
M_x, M_y	Moments in Horizontal Plane
u_x, u_y	Lateral Displacements
θ_x, θ_y	Lateral Displacements
W^p	Plastic Work-done
s	Ratio of Elliptical Axes
β	Yield Surface Orientation
g	Plastic Potential Surface
f	Yield Function
μ	Function of Plastic Multiplier
G^p	Plastic Shear Modulus
A	Plastic Resistance
Ξ	Plastic resistance matrix with several components
s_u	Undrained Shear Strength (cohesive soil)
tol	Tolerance
R	Linear Transformation Matrix
R^T	Transpose of R

CLAP Notations

ϵ^R	Ratcheting Displacement/Strain
ϵ^P	Plastic Displacement/Strain
ϵ_e	Elastic Displacement/Strain
ϵ	Total Displacement/Strain
R_{kj}	Ratcheting Parameter.
R_0	Initial Ratcheting Parameter

β_r	Hardening Strain
β_0^r	Initial Hardening Strain
α	Back-stress at the end of the step
α_0	Back-stress at the beginning of the step
σ	Force/stress at the end of the step
σ_0	Force/stress at the beginning of the step
K_{Pl}	Plastic Stiffness Matrix.
K_P	Spring stiffness for a given yield surface.
S	Spring-slider strength for a given yield surface (radius of the yield surface)
λ_j	Plastic multiplier for a given yield surface.
$\frac{\partial \mathrm{g}}{\partial \sigma}$	The gradient of the yield function with respect to force.
K_e^T	Elastic Stiffness Matrix
R_{fac}	Number of Cycles to Skip in Cyclic Acceleration Scheme
$\boldsymbol{\kappa}$	Ratcheting distortion correction factor

Acronyms

GHG	Greenhouse Gas
OWT	Offshore Wind Turbine
HARM	Houlsby-Abadie Ratcheting Model
REDWIN	REDucing cost in offshore WINd by integrated structural and geotechnical design
TRL	Technology Readiness Level
SSI	Soil-Structure Interaction
SLS	Serviceability Limit State
FLS	Fatigue Limit State
ULS	Ultimate Limit State
FEA	Finite Element Analysis
FE	Finite Element
PISA	Pile Soil Analysis
DNV	Det Norske Veritas
API	American Petroleum Institute
0D, 2D, 3D, 4D	Zero dimensional, Two-dimensional, Three-dimensional, Four-dimensional
DOF	Degrees of Freedom
CLAP	Cyclic Loading & Analysis of Piles
MSKH	Multi-Surface Kinematic Hardening/Multi-Surface Plasticity Framework
KH	Kinematic Hardening
SHM	Structural Health Monitoring
OC6	Offshore Code Comparison, Collaboration, Continued, with Correlation and unCertainty
WAS-XL	Wave Loads and Soil Support for Extra Large Monopiles
LDM	Logarithmic Decrement Method
NGI	Norwegian Geotechnical Institute
DSM	Degradation Stiffness Model
OCR	Over-Consolidation Ratio
B-SDM	Bounding Surface Stiffness Degradation Method
DEM	Discrete Element Method
NREL	National Renewable Energy Laboratory
SMM	Structural Mechanics Module in COMSOL
SIM	SSI Module in COMSOL

DECLARATION OF AUTHORSHIP

Declaration of Authorship

I declare that this thesis and the work presented in it are my own and have been generated by me as the result of my own original research.

Where I have consulted the published work of others, this is always clearly attributed.

Where I have quoted from the work of others, the source is always given. With the exception of such quotations, this thesis is entirely my own work.

I have acknowledged all main sources of help.

Where the thesis is based on work done by myself jointly with others, I have made clear exactly what was done by others and what I have contributed myself.

This thesis contains no material that has been submitted previously, in whole or in part, for the award of any other academic degree or diploma.

I cede the copyright of the thesis in favour of the Université de Liege and Ecole Centrale de Nantes.

Date: 21st August, 2024 Signature

ABSTRACT

The offshore wind energy sector is growing rapidly as a means to achieve the target net zero GHG (Greenhouse gas) emission by 2050. This technology has been expanded to the offshore wind turbines (OWTs) both bottom-fixed and floating foundations. The foundations of such structures have to be optimized geometrically such that they are robust and resilient against environmental loads from wind, waves and currents which are usually cyclic, multidirectional and complex in nature.

Accurate modelling of the foundation behavior for bottom-fixed and floating OWTs is critical in predicting the global response of the system. This aspect of the integrated design of the entire OWT system is not very much understood in design software programs, typically resulting in empirical modelling to represent the constitutive behavior of the foundation or, in extreme cases, models that assume the foundation is infinitely rigid (fixed) in many structural and geotechnical engineering applications.

The foundation modeling for OWTs requires considering accumulated rotational deformations due to combined cyclic and sustained loading, which affects the foundation stiffness. Additionally, it needs to account for the coupling of loads from different directions. Such effects have rarely been accounted for comprehensively with simple numerical models.

However there exist certain specialized models like the Houlsby-Abadie Ratcheting Model (HARM) strongly rooted in the kinematic hardening principles within the hyperplasticity (thermo-mechanical) framework, which enables capturing of the accumulated deformations over many cycles (typically millions) of cyclic loadings. Then, there is the REDWIN model which is an acronym referring to “REDucing cost in offshore WINd by integrated structural and geotechnical design”, and it account for the multidirectional load coupling.

This research focuses on programming, improving, and developing a novel constitutive model called CLAP an acronym for “Cyclic Loading & Analysis of Piles”. The output of this work can be further enhanced and used for various applications and case studies on complex multidirectional cyclic loading in the offshore industry.

Keywords: Offshore Wind Turbine; Monopile Foundation; Cyclic Loading; Accumulated Deformation (Ratcheting); Hyperplasticity Theory; Constitutive Model; Kinematic Hardening; Mathematical Modelling & Implementation; Macro-element Modelling; Multidirectional Loading.

1. CONTEXT AND MOTIVATION

1.1 Offshore Wind & Foundation Design

Modern-day society needs, require energy savings and de-carbonization of the built environment. Alternative and renewable energy sources are becoming more attractive and new ways for energy harvesting are been explored. Wind energy is considered a sustainable and renewable energy which is growing fast in Europe and globally. To take advantage of high wind speeds, offshore wind turbines (OWTs) are now built and there are plans for these to be extended into deeper waters.

Although this is a very promising green energy technology, there are still some challenges to be overcome. New OWTs to be built in deeper waters require taller and more slender towers which are more sensitive to lateral loads from wind and sea waves. Moreover, alternative foundation techniques need to be explored which consider multidirectional load and large values of base shear and bending moment. In many cases, the natural frequencies of vibration of these OWTs are close to the various forcing frequencies that are imposed on them, and therefore detrimental resonance and dynamic amplification may be possible.

OWT structures vary depending on the foundation/support platform fixity. The fixed foundation types are the gravity base, suction bucket monopile, monopile, tripod, jacket, etc., while the floating foundation types are the tension leg platform, spar buoy, and semi-submersible. The technology readiness level (TRL) for OWT supported on the monopile foundation is quite very high as the technology is already well established in the offshore industry. The monopiles account for about 75 – 80 % of foundations installed offshore, thus, this project is focused on application to OWT supported on monopile foundations.

Monopile foundations for OWTs experience significant moments and horizontal loads, with relatively small vertical loads, unlike foundations in the oil and gas industry. The horizontal-to-vertical load ratio (H/V) for OWT ranges from 1.5–2.5 compared to about 0.25 in the oil and gas sector. OWTs are flexible structures with low stiffness and natural frequency, making them sensitive to dynamic loadings. The choice of foundation system (deep or shallow) can affect the natural frequencies of the wind turbine system, which change with cyclic or dynamic loading. For strain-hardening sites (loose to medium-dense sand), natural frequency tends to increase, while for strain-softening sites (normally consolidated clay), it tends to decrease. Existing design guidelines for offshore oil and gas installations cannot be directly applied to OWT foundations due to two main reasons – OWT foundations must resist large overturning moments that are much higher than the vertical loads, and the structures are dynamically sensitive, with fatigue being a critical design factor (Letcher, 2017).

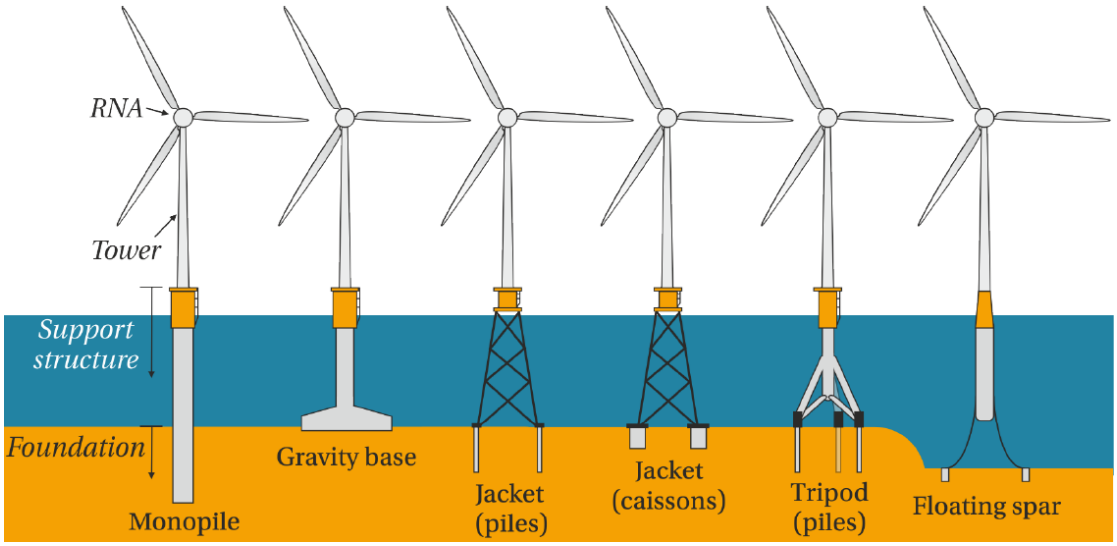

Figure 1. 1. Offshore Wind Turbines Foundation/Platform Types (Richards, 2019).

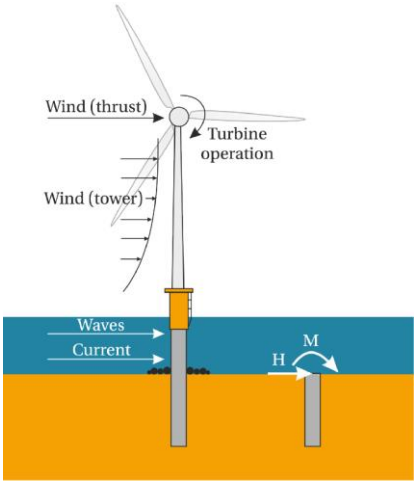

Figure 1. 2. Lateral Load Acting on OWT Supported on Monopile Foundation (Richards, 2019).

OWT foundations are subjected to significant environmental loads arising from current, wind, and wave actions. These environmental forces result in combined moment and horizontal loading that is both cyclic and complex, varying continuously in amplitude, direction, and frequency. The accumulation of rotation due to cyclic loading, known as ratcheting, is a key concern for monopile designers. The environmental loads on these structures change direction over their service life, making it essential to consider load directionality in the design and construction of OWT foundations.

Despite the dominance of monopile foundations in offshore installations, their design can be optimized using integrated time-domain multidirectional loading analysis. OWTs must meet specific design requirements, including tight tolerances concerning their natural frequencies and minimal permanent rotation by the end of their service life. The response of monopiles, assessed through macro-element modeling, is crucial for meeting these requirements.

Throughout the typical 20-year lifespan of an OWT, its foundation is subjected to various forms of cyclic and dynamic loading, including wind, waves, currents, storms, typhoons, tsunamis, and earthquakes. These loads can degrade the foundation, posing significant risks to OWT operation. Soil-structure interaction (SSI) between the monopile and the soil during cyclic loading leads to permanent deformation build-up in saturated soil, along with an increase in pore water pressure. This accumulated deformation, coupled with sustained loading, results in a rotational phenomenon known as ratcheting, which can cause the foundation to tilt.

From the perspective of the serviceability limit state (SLS), it is essential to ensure that the foundation remains within the operational tolerance of 0.25° throughout its lifespan. However, there is no consensus in the applicable codes of practice on universally accepted methods for evaluating the SLS. The monotonic and cyclic loadings experienced by OWTs can also lead to pore pressure evolution in liquefiable soil, significantly reducing the soil's strength and stiffness and affecting the structural dynamic response.

Overall, the design and optimization of OWT foundations must account for the complex and cyclic nature of environmental loads, the directionality of these loads, and the critical SSI effects to ensure long-term structural integrity and operational performance.

1.2 Design to Cyclic Loading

This section presents some of the most commonly used methods for design to cyclic loading applied to OWT supported on monopile, applicable to both unidirectional and multidirectional loadings.

1. Macro-element Method: The Macro-element method is a 0D model that simplifies the complex soil-foundation interaction by representing the soil as a single element with equivalent stiffness and damping properties. In other words, it is a reduced element modelling approach of representing a significant portion/component of a system by a super-element to assess the response/behavior of the system at that location. This approach typically assumes the soil behaves

as a homogeneous, elastic material. The entire monopile-soil interaction is represented by a constitutive model at the seabed level (mudline). This method provides a simplified representation of the soil behavior around a foundation, which is crucial for offshore monopile foundations.

The macro-element method can simulate the monopile response with almost the same accuracy as finite element analysis (FEA) but with a considerable reduction in computational effort. However, this simplified model may not capture all the complexities of SSI and requires calibration against more detailed models or experimental data (Page et al., 2019a).

2. Winkler Foundation Method (p-y models): The Winkler foundation method models soil as a series of independent springs and dashpots, using p-y curves to describe soil behavior. These curves relate the lateral soil reaction (p) to the foundation displacement (y), capturing the nonlinear elastic nature of soil response. This method, though an approximation, provides satisfactory results comparable to more precise methods and is particularly relevant for modeling soil-structure interaction in offshore foundations.

Empirical representation of the model-based Matlock (1970) under static loading is given in the equation below;

$$P(y) = \begin{cases} P_u \times 0.5\left(\frac{y}{y_{50}}\right)^{\frac{1}{3}} & \text{for } y \leq 8y_{50} \\ P_u & \text{for } y > 8y_{50} \end{cases}$$

Where P_u is the peak lateral load, and y_{50} is the deflection of the foundation at 50 % P_u.

Application and Limitations

In current practice, the design of offshore piles to resist lateral loading employs the nonlinear Winkler modeling approach, commonly known as the p-y method. This framework, originally derived from large-scale field tests on long, flexible piles for the oil and gas industry, relies on accurately defining the local soil reaction at each point down the pile. The governing law for each uncoupled spring, p(x, y), depends on depth (x) and pile displacement (y) and is determined based on field test data (Abadie, 2015).

However, the p-y method has limitations when applied to offshore wind monopiles. It was developed for flexible piles and high embedded length-to-diameter (L/D) ratios, which may not accurately represent the rigid pile response typical of monopiles. Recent design guidelines recommend complementary finite element (FE) calculations for rigorous design due to these limitations.

Specific Issues and Considerations

Presented below are some of the most important issues and considerations when using the Winkler model;

- Hysteretic Behavior and Soil Damping: The p-y method does not account for the hysteretic behavior of the soil, leading to poor consideration of soil damping. This is crucial for accurately predicting the response under cyclic loading conditions.
- Loading Conditions: The loading conditions for oil and gas structures differ significantly from those for wind turbines. Horizontal loads on oil and gas piles are minor compared to vertical loads, whereas lateral cyclic loading is more critical for wind turbines.
- Cyclic Loading Effects: The method poorly addresses the effects of cyclic loading, which is essential for predicting permanent deformations, soil stiffness, and damping due to both long-term operational and short-term storm events. Empirical cyclic degradation factors may be over- or underestimated depending on site-specific conditions.
- Soil Stiffness and Pile Diameter: The original p-y formulations focus on soil strength parameters rather than stiffness parameters and do not adequately consider the impact of pile diameter on stiffness. This can lead to an over-conservative design.
- Operational Conditions: The soil response under operational conditions is poorly addressed. The original p-y formulations do not focus on the small-strain response experienced during normal operations, nor do they consider long-term effects on stiffness or provide guidelines for estimating soil-pile damping.

The Winkler model based on p-y curves provides a simplified approach for modeling SSI but has notable limitations, especially for OWT monopiles. These limitations include inadequate representation of cyclic loading effects, soil stiffness, and damping. Consequently, standard design calculations using this method may be overly conservative, potentially leading to uneconomical designs. Complementary methods, such as FE analysis, are recommended to ensure accurate and reliable design outcomes for OWT foundations.

3. Finite Element Method: This method is a numerical approach used to simulate soil-foundation behavior by discretizing the soil and foundation into small elements. The method solves the equations of motion for each element, capturing the entire soil continuum and the complete monopile-soil interaction. It is a powerful tool that handles complex geometries, varied loadings, and diverse material properties, making it adaptable to the detailed and comprehensive design requirements of OWT development projects. While this approach offers high accuracy and flexibility, it can be computationally intensive, particularly for large or complex problems. Additionally, effective use of FEM requires a solid understanding of the underlying principles and numerical techniques.

4. Physical Modelling based on 1 g Test: Physical modeling under a 1 g gravitational field involves conducting small-scale experiments in a laboratory setting to study soil-foundation behavior. This type of geotechnical testing uses scale models to investigate how structures respond to different loading conditions under normal gravity. Although 1 g modeling provides valuable insights, it may not fully capture the complexities of real-world conditions due to scaling issues. Therefore, it is often complemented by other testing methods, such as centrifuge testing, to gain a more comprehensive understanding of the structure's behavior.

5. Physical Modelling based on Centrifuge Test: Centrifuge testing simulates prototype conditions by conducting small-scale experiments in a centrifuge, which applies a high gravitational field to reduce scale effects. This method can replicate full-scale stress levels, offering a more realistic representation of SSI, particularly for OWT foundations under actual loading conditions. Despite its effectiveness, centrifuge modeling is both expensive and time-consuming. It also requires specialized equipment and expertise, making it a resource-intensive testing method.

Table 1. 1. Summary Outline of Advantages and Disadvantages of Design to Cyclic Loading Methods.

Methods	Advantages	Disadvantages
Macro-element Method	– Efficient computation – Easy to implement	– May oversimplify soil behavior – Accuracy is dependent on calibration input based on load-displacement curves
Winkler Model (p-y curves)	– Simple and widely used – Easy to implement	– Assumes soil behaves independently, neglecting soil-foundation interaction – Limited accuracy, neglects soil nonlinearity and heterogeneity – Too conservative design for OWT
Finite Element Method	– Accurate and flexible – Can model complex soil behavior and nonlinear effects	– Computationally expensive – Requires expertise in FEM and geotechnical engineering
1 g Modelling	– Cost-effective and easy to conduct – Provides valuable insights into soil behavior	– Scale effects: small-scale models may not accurately represent prototype behavior – Limited accuracy due to simplifications and idealizations
Centrifuge Modelling	– Improved accuracy compared to 1 g tests – Reduced scale effects	– Expensive and complex setup – Limited availability of centrifuge facilities

1.3 PISA Method

In recent years, the PISA (Pile Soil Analysis) joint industry project developed a generalized form of the Winkler approach to accurately capture the response of rigid piles under monotonic loading. The PISA project was aimed at capturing the monotonic curve typically referred to as the backbone curve. This section presents a literature review of the PISA method.

1.3.1 Literature Review on the PISA Method

The PISA project has significantly advanced the understanding of monopile foundations for OWTs, particularly under monotonic and cyclic loading conditions. This literature review synthesizes key findings from various studies within the project, linking their contributions to the overall understanding of monopile behavior.

Cyclic Loading Effects

Byrne et al. (2020a) studied the cyclic loading effects on pile response under varying conditions; and investigated both one-way and two-way loading scenarios with different load levels (amplitudes and frequencies) under the PISA project, including cyclic loading response features like ratcheting phenomena, stiffness change, and damping. Testing included cyclic loading on piles of different diameters and lengths. Emphases were on the monotonic capacity and cyclic loading effects, with the resulting experimental campaign leading to new cyclic modeling approaches for monopile foundations. Results from the paper indicated that one-way cyclic loading showed ratcheting behavior with plastic displacement reduction, while two-way cyclic loading produced symmetric load-displacement responses with reduced stiffness.

Beuckelaers (2015) presented an innovative approach to the enhancement of the wind turbine fatigue life prediction based on a kinematic hardening soil model with the incorporation of improved material damping for a realistic foundation response in the sand. The paper addresses the uncertainties and lack of soil damping evaluation for each load simulation, and the need for tuning damping coefficients in design methods. The author underscored the significance of accurately estimating material damping that is amplitude-dependent, derived from the response of pile-soil interaction. This is vital for reducing the risk of failure due to fatigue achieved by avoiding resonance and improving the damping on the structure. The paper further discussed various damping components on the structure – structural damping, hydrodynamic damping, aerodynamic damping, tower oscillation damping, and soil damping, of which soil damping is identified as the component with the most uncertainty.

Beuckelaers et al. (2017) described the implementation of a kinematic hardening model based on macro-element for soil reaction at both lateral directions by the soil reaction curves based on the design guide (API/DNV). The model is applied in the SSI of monopiles with a focus on capturing effectively the increase in damping, and decrease in stiffness at increasing amplitudes of loading. This model has been integrated under a coupled aero-elastic model in time-domain dynamic analysis. The kinematic hardening model, when applied to the design method for wind turbine monopiles installed in sand, improved predictions of amplitude-dependent material damping derived from the pile-soil response. This eliminated the need for re-evaluating soil damping for each load simulation and tuning of damping coefficients. In essence, it included large strain material damping from the soil in the calculation process – enabling a better understanding of damping estimation, response prediction, and fatigue calculation.

Field Testing and Model Validation

McAdam et al. (2020) studied reduced-scale field testing of monopiles in dense marine sand with structural optimization as part of the PISA project and analyzed the response (load-displacement behavior for piles of varying diameters and length-to-diameter (L/D) ratios, bending moments, and inclinations) using fiber optic strain gauges and inclinometers. These are field tests performed in dense sand at Dunkirk for wind turbines, thus, supporting a new design approach for monopile foundations for OWTs. The paper investigated the influence of loading rate on monopiles in sand. Strain softening behaviour is observed in short medium-diameter piles at the Dunkirk site for sand, not seen in Cowden clay tests; strength and stiffness metrics increase with length in medium-diameter piles; loading rate influences strength enhancement in sand monopiles; time-dependent effects due to creep is apparent in all monotonic loading tests; gaps around piles influenced unload-reload behaviour due to pore pressure suctions; the tests were conducted onshore, thus,

not representative of offshore conditions; and the field data is used for validation of FEA for design – with high repeatability observed in pile tests to supports data verification for models. The data obtained from the test campaign support the development of the new 1D model in the design of OWTs supported on monopile foundations.

Byrne et al. (2020b) analyzed the monotonic lateral pile field testing in stiff (heavily over-consolidated) glacial clay till as part of the PISA project conducted on piles with varying diameters (0.273 m, 0.762 m, and 2.0 m), varying L/D between 3 – 10 and loading conditions, and assessed bending moments, inclinations, and lateral displacements of piles. The authors aimed to develop improved design methods for monopile foundations for OWTs with the creation of a new 1D modeling approach. The field tests, soil characteristics, and FE modeling were discussed, thus, supporting the interpretation of Cowden site tests with a 3D FE model. This is a sequel to the tests conducted on dense sand at the Dunkirk site. The study further aimed at addressing the lack of reliable strain data from extensometers in the existing literature, furthermore, extensometer data reliability issues led to reliance on fiber optic data. Also, Glacial tills are challenging to replicate accurately in laboratory model testing. Collected data serve as a database for specifically supporting the validation of lateral loading of monopiles at vertical elevation above the ground level on over-consolidated clay. Creep effects and loading rate influence are investigated via the application of monotonic loading with the incorporation of constant (sustained) load periods.

Design Implications

Byrne et al. (2017) summarized the principal project findings on the PISA project with implications for design discussed and elaborated with examples taken from the Cowden stiff clay soil profile. The authors aimed at reducing conservatism in monopile design for OWT foundations with the potential for substantial savings in selected design scenarios and generated a new industry standard database for design models in clay and sand validation with application to larger L/D piles and suction caisson foundations. Furthermore, the paper aimed at attempting to address research gaps concerning uncertainties in p-y curve calibration for OWT monopiles, lack of consideration for cyclic loading effects on monopile foundations, and the challenges in modeling installation effects on pile response.

Findings indicated that the field testing (medium-scale) gathered substantial data on pile response and soil profiles and that the soil data confirmed lower undrained strength in the top 2 m. Also, new laboratory testing programs have been commissioned to examine strength and stiffness. The new design method enhances monopile foundation accuracy and reduces conservatism. Bespoke soil reaction curve calibration is informed by 3D FE analysis. Limitations of the study are the consideration of two specific soil profiles for offshore wind farm sites, focus on monotonic loading only, neglecting cyclic loading interpretation; and neglect of effects of installation on pile response due to modeling challenges.

Development of 1D Computational Models

Burd et al. (2019) described a 1D computational model for lateral loading analysis and design of OWTs supported on monopiles, focusing on the application of the model to predict monopile performance in marine sand. Calibration of the model is informed by 3D FEA for accuracy which was done over a calibration space comprising of the geometries of the piles, loading configuration, and relative densities of the soil spanning typical values for design. The model is represented in the form of soil reaction curves (based on specially formulated functions – conic function) due to an idealized embedded beam used for monopile design in marine sand with homogeneous assumptions under drained loading conditions. Soil reaction components are incorporated for improved performance, while the Winkler assumption and p-y method are discussed.

There are research gaps in the lack of calibration for cyclic loads in constitutive parameters, and model not validated for soil layering and cyclic loading. Practical implications of the study are in the aspect of rapid design calculations for OWT monopile foundations, application to homogeneous sand sites with accurate performance predictions with the possibility of extension to cyclic loading and layered soil profiles, and calibration process can be done based on soil conditions at the PISA Dunkirk sand site for realistic model. The model applies to monopiles with uniform wall thickness. Findings indicate PISA model prediction of monopile performance closely matched the 3D FE models with the accuracy metrics showing close agreement between 1D and 3D models. The PISA model is limited to homogeneous soil and monotonic loading, though extensions to layered soil and cyclic loading are possible. In addition, spatial coupling within the soil is

ignored, leading to scatter (variability) in data plots for depth variations based on normalized soil reaction curves due to distributed loads along the pile, thus, the model cannot accurately depict the interaction between the monopile and soil at every point along the pile.

Burd et al. (2020) performed 3D analyses on monopiles in layered soils (with varying characteristics) showing strength variations; with comparative analysis indicating that the PISA design model matches closely with 3D FEA. The PISA model is extended to effectively analyze monopiles in layered soil configurations; while the 3D analyses validate the PISA model for monopile behavior in various scenarios. The paper contributes to design model calibration for high-fidelity monopile performance representations. The practical implication of the study is on the improved performance of the model in most layered soil configurations; furthermore, deep-lying stiff layers can enhance monopile strength in certain soil combinations, though not yet incorporated in the PISA design model according to the period of article publication. The study also aimed at addressing research gaps in the lack of consideration for very soft clay and very dense sand, plus the absence of a deep-lying stiff layer which benefits the PISA design model.

Findings indicated that the PISA model applies well to layered soils, except for soft clay-dense sand combinations. Soil layering impacts monopile performance, with varying strength and stiffness. The PISA model closely matches 3D FE data for monopile behavior. PISA model limitations are in very soft clay and dense sand, as well as a lack of uplift capacity assessment for deep-lying stiff layers.

The PISA project has substantially improved the understanding and design of monopile foundations for OWTs. Key contributions include enhanced models for cyclic loading effects, validated field test data, and the development of advanced 1D computational models. While significant progress has been made, ongoing research is needed to address limitations related to cyclic loading, soil layering, and site-specific soil conditions to further refine and optimize monopile design methodologies for OWTs.

1.4 Gaps of Knowledge & Proposed Model

1.4.1 Gap of Knowledge

Accurately modeling the behavior of OWT foundations under multidirectional cyclic loading is crucial for optimizing their design and ensuring long-term structural integrity. However, current design software programs often rely on empirical modeling or overly simplistic assumptions, such as fixed boundary conditions, which fail to capture the complex interaction between the foundation, soil, and environmental loads. One significant knowledge gap lies in understanding the cumulative effect of rotational deformations induced by combined cyclic and sustained loading on foundation stiffness. While specialized models like the HARM model address the accumulation of deformations over millions of cycles under unidirectional loading, they may not fully encompass the multidirectional aspect, especially about coupled loads. Conversely, models like REDWIN, designed for integrated multidirectional load coupling, might not explicitly account for the long-term cyclic degradation of foundation stiffness due to strain accumulation.

Therefore, a comprehensive approach that integrates both the accumulated rotational deformations due to cyclic loading and the multidirectional nature of environmental forces is needed to advance the accuracy and reliability of OWT foundation models. Coupled with the fact that there's limited entry of macro-element models into the design practice.

1.4.2 Premise for a Novel Model

HARM and REDWIN models address the complexities of multidirectional cyclic loading on OWT foundations in distinct ways. HARM excels at capturing the accumulation of deformations (ratcheting) caused by millions of load cycles, a crucial aspect of OWT foundations subjected to continuous wave and wind actions. Based on kinematic hardening principles within the hyperplasticity framework, HARM effectively simulates the progressive, irreversible deformation under cyclic loading, making it highly suitable for simulating the long-term effects of cyclic loading on foundation settlement and rotation. However, its primary focus on accumulated deformation may not fully encompass the complexities of coupled multidirectional loading scenarios.

The REDWIN model directly addresses the coupling of multidirectional loads. Generally, this model aims at "reducing cost by integrated design" focusing on optimizing the overall system response to multidirectional loading via macro-element representation of foundation behavior while capturing the essential interactions between wind, wave, current, and foundation response. This model excels in simulating the combined effects of loads from various directions, which is critical for accurate representation of real-world conditions. However, the model does not explicitly account for the long-term, cyclic degradation of foundation stiffness due to ratcheting.

In summary, HARM provides a detailed, material-centric perspective on cyclic loading effects, while REDWIN offers a more holistic, system-level approach to multidirectional load interaction. Combining the strengths of both models at the macro-element level could lead to a more comprehensive understanding and accurate prediction of OWT foundation behavior under realistic loading conditions. A comprehensive model is needed to integrate the strengths of both models to fully capture the complexities of multidirectional cyclic loading on OWT foundations. Thus, a novel model called the CLAP (Cyclic Loading & Analysis of Piles) model is proposed to account for these deficiencies and gaps in research knowledge.

1.5 Aims and Objectives

The objective of the project is to assess the possibility of coupling the HARM and REDWIN models to create a single novel model capable of predicting the OWT foundation response comprehensively, with the ultimate goal of developing an open-source program. The expected tasks include:

- Developing a comprehensive understanding of both the HARM and REDWIN models based on plasticity principles through an extensive literature review, focusing on modeling offshore piles under multidirectional cyclic loadings, constitutive models, and hardening laws.
- Investigating the theoretical, mathematical, and numerical development of both models to enable coupling, leading to a single program accessible to OWT designers and engineers for assessing foundation response to various loading conditions. This may include presenting the model as a user manual for future use.
- Verifying and validating the resulting model against numerical data from existing REDWIN and/or HARM publication(s).

The project primarily focuses on programming and developing a new constitutive model, with potential applications to demonstrate the program's capabilities in simple or complex cases. This could lead to advancements in the design and structural prognosis of OWT foundations.

2. CONSTITUTIVE MODELLING

2.1 Hyperplasticity Framework

The hyperplastic framework is a research field immersed in complex and rigorous mathematical formulations. The essence of this study is not to dive fully into the mathematical details but to present the theoretical and numerical applications to the constitutive behavior of the OWT supported on a monopile foundation based on macro-element modelling. The framework is a modern approach to plasticity theory that is firmly rooted in thermodynamic principles. It allows for the derivation of constitutive models for irreversible behavior entirely from two scalar potential functions. It ensures that the models developed obey the first and second laws of thermodynamics. This guarantees that the energy dissipation and storage are consistent with physical laws. The entire material response is derived from two potential functions say the Helmholtz free energy (or Gibbs' free energy) and the dissipation potential also known as the dissipation function.

The hyperplasticity framework has the advantages of model consistency i.e. the use of thermodynamic principles ensures that the models are physically consistent and reliable; model flexibility i.e. it allows for the interchange of dependent and independent variables, making it adaptable to different applications; and model simplicity i.e. models definition, classification, and development are simplified via the use of potential functions. Though, the framework simplifies the formulation of models, the underlying mathematics can be complex and may require advanced knowledge in thermodynamics and continuum mechanics.

The framework adheres to the Ziegler orthogonality principle (Ziegler, 1977) which is related to energy dissipation particularly the second law of thermodynamics. The orthogonality principle can be viewed as a stronger statement than the second law of thermodynamics in terms of the assumption that the dissipation function acts as a potential, leading to the concept that the "dissipative generalized stress" is orthogonal to the level surfaces of the dissipation (Houlsby & Puzrin, 2006). This principle requires that the rate of change of the back-stress is orthogonal to the yield surface, thus, ensuring that the dissipation is maximal. This maximal dissipation assumption can be viewed as a stronger form of the second law of thermodynamics which requires that energy be dissipated, but the orthogonality principle goes further by requiring that the dissipation be maximal. This principle is particularly useful in constitutive modeling as it ensures that the material's response is thermodynamically consistent and that the energy dissipation is maximized under given constraints.

2.1.1 Influence of the Dissipation Potential in Plasticity Models

The dissipation potential is a concept used to describe irreversible processes in a thermodynamic system. It represents the rate at which energy is dissipated as heat or other forms of energy loss due to irreversible processes such as friction, viscosity, or plastic deformation (Houlsby, 2014). In plasticity and hyperplasticity, the dissipation potential is used to derive the constitutive equations that describe a material's behavior. It is a non-negative function of the generalized velocities, such as the plastic strain rate, and ensures that the second law of thermodynamics is satisfied, meaning that entropy production is always non-negative. These two potential functions (energy potential and dissipation potential) allow for a concise and systematic formulation of constitutive models. Emphasis is placed on the derivation of incremental response, which is necessary for numerical analysis. This allows for the accurate prediction of material behavior under varying loading conditions.

In plasticity theory, the dissipation potential is intimately related to the yield surface and the flow rule. The yield surface defines the stress states at which a material begins to plastically deform, and the dissipation potential helps in defining this surface. The flow rule describes the relationship between the plastic strain rate or plastic strain increment and the stress state. The dissipation potential can be expressed as a function of the generalized velocities, and its gradient with respect to these velocities gives the dissipative forces used in the flow rule. This approach allows for a systematic and thermodynamically consistent formulation of constitutive models for materials undergoing irreversible processes.

The dissipation potential can be used in both rate-dependent (viscoplastic) and rate-independent (plastic) models. In viscoplastic models, the dissipation potential is a smooth function of the plastic strain rate, allowing for the description of time-dependent behavior. In classical plasticity models, the dissipation potential is often non-smooth, corresponding to rate-independent behavior. This potential quantifies the energy dissipated during plastic deformation, which is crucial for predicting the fatigue life of materials under cyclic loading, as it helps in understanding how energy is lost and how it affects the material's mechanical response.

2.1.2 Flow Rule in Plasticity Models

The flow rule is a fundamental concept in plasticity theory that describes how materials deform plastically under applied loads. Here, the total strain in a material is decomposed into an elastic part, which is recoverable upon unloading, and a plastic part, which represents permanent deformation. When the stress state reaches the yield surface, plastic deformation occurs. The flow rule then determines the direction and magnitude of the plastic strain increment, mathematically expressed as:

$$d\epsilon^P = \lambda \frac{\partial g}{\partial \sigma}$$

Where $d\epsilon^P$ is the plastic strain increment, λ is the plastic multiplier, g is the plastic potential function, and σ is the stress tensor. The two main types of flow rules are the associated flow rule and the non-associated flow rule. In the associated flow rule, the plastic potential function g is the same as the yield function f, meaning the plastic strain increment is normal to the yield surface. This ensures that the material's behavior is consistent with the principle of maximum plastic dissipation. In the non-associated flow rule, the plastic potential function g is different from the yield function f, allowing for more flexibility in modeling materials that exhibit different dilation and shear behaviors say soils and granular materials. The choice of flow rule affects the predicted material behavior under different loading conditions and is essential in calculating plastic strain increments during incremental response in simulations.

The hyperplasticity model provides a common basis for the formulation and comparison of many existing plasticity models, and it incorporates an introduction to elasticity, plasticity, thermodynamics, and their interactions (Houlsby & Puzrin, 2006). Energy potential say Helmholtz free energy measures the useful work obtainable from a system at constant temperature and is minimized at equilibrium; while dissipation potential describes the rate of energy dissipation due to irreversible processes and ensures thermodynamic consistency in constitutive modelling.

Overall, the dissipation potential ensures thermodynamic consistency, defines the yield surface and flow rule for plastic deformation, applies to both viscoplastic and classical plasticity models, and quantifies energy dissipation during plastic deformation. This understanding is essential for developing accurate and reliable constitutive models for materials undergoing irreversible processes.

2.2 Kinematic Hardening Plasticity Models

2.2.1 Multi-Surface Kinematic Hardening (MSKH) Model Assumptions

The multi-surface kinematic hardening (MSKH) model is based on the assumption that plastic deformation in materials can be described using multiple nested yield surfaces, each associated with its own kinematic hardening (KH) rule. Some key assumptions and features of the MSKH model are:

- Multiple yield surfaces: Instead of a single yield surface, the material behavior is described using several yield surfaces. Each of these surfaces can move in the stress space to represent the accumulation of plastic strain.
- Kinematic hardening: Each yield surface follows a KH rule, which means that the center of each yield surface can translate in the stress space as the material undergoes plastic deformation. This helps in accurately capturing the Bauschinger effect, where the material exhibits different yield strengths in tension and compression after cyclic loading.

- No interaction between surfaces: The yield surfaces are assumed to act independently of each other. Each surface moves according to its KH rule without direct interaction or intersection with the other surfaces.
- Incremental plasticity framework: The model operates within an incremental plasticity framework, where the stress-strain response is updated incrementally based on the current state of the material and the applied loading.
- Elastic-plastic decomposition: The total strain is decomposed into elastic and plastic components. The elastic part follows Hooke's law, while the plastic part is governed by the movement of the yield surfaces.
- Associative flow rule: The plastic strain increment is normal to the yield surface.

2.2.2 Prager, Ziegler, and Mróz Models Assumptions in Constitutive Modelling

In constitutive modelling especially regarding materials in offshore foundations under cyclic loading, the selection of the specific assumption plays a critical role in the behavior of the constitutive model especially in how yield surfaces behave during hardening. The Prager, Ziegler, and Mróz model assumptions are presented here.

The Prager's model (Prager, 1949) is one of the simplest KH models. It assumes linear KH i.e. the yield surface translates in the stress space without changing its size or shape, and the movement is proportional to the plastic strain increment; the evolution rule is linear i.e. the back-stress α, which represents the translation of the yield surface, evolves linearly with the plastic strain; and the model typically uses a single yield surface, which limits its ability to accurately capture complex cyclic loading behaviors. Below is Prager's equation:

$$\dot{\alpha} = C.\dot{\epsilon}^P$$

Where $\dot{\alpha}$ is the rate of change of the back-stress, C is a stiffness constant, and $\dot{\epsilon}^P$ is the plastic strain rate.

The Ziegler's model (Ziegler, 1959) extended the Prager model by introducing a nonlinear evolution of the back-tress. It assumes nonlinear KH i.e. the yield surface still translates in the stress space, but the movement is now governed by a nonlinear function of the plastic strain increment; the evolution rule is nonlinear i.e. the back-stress evolves nonlinearly, providing a better fit for materials that exhibit nonlinear hardening behavior; and it typically uses a single yield surface, similar to the Prager model. It is worth noting that the model is based on the orthogonality principle described earlier which ensures that the direction in which the yield surface translates does not affect its shape nor size. It has the characteristic of thermodynamic consistency i.e. ensuring that the model is consistent with the principles of thermodynamics. Below is Ziegler's equation:

$$\dot{\alpha} = C.(\sigma - \alpha).\dot{\epsilon}^P$$

Where σ is the stress tensor. Note that the total strain is the elastic strain plus the plastic strain.

The Mróz's model (Mróz, 1967) introduces multiple yield surfaces. It assumes multiple yield surfaces i.e. the material behavior is described using several nested yield surfaces, each with its own KH rule; the yield surfaces can expand and contract, and each surface can yield sequentially. This allows for a more accurate representation of complex cyclic loading; each yield surface follows a bilinear KH rule, allowing for better capture of the Bauschinger effect and other cyclic plasticity phenomena; and the plasticity framework is incremental i.e. the stress-strain response is updated incrementally, similar to the MSKH model. The model can capture more complex behaviors such as cyclic softening/hardening and ratcheting.

The selection of specific assumptions in constitutive modeling significantly influences the predicted behavior of offshore foundations under cyclic loading. This includes how the yield surfaces move and evolve which affects the model's ability to capture cyclic plasticity, ratcheting, and shakedown behaviors; the rules governing back-stress evolution determine how well the model can simulate the Bauschinger effect and the material's response to load reversals; models with multiple yield surfaces are better suited for complex loading paths encountered in offshore environments, where loads can be multidirectional and varying in amplitude; assumptions about hysteresis and energy dissipation affect the model's ability to predict damping and long-term settlement or tilt of offshore foundations; and the choice of model and its assumptions directly impact the accuracy of predictions for foundation performance, influencing design decisions and safety assessments for offshore structures.

2.2.3 Hierarchy of Kinematic Plasticity Models

The hierarchy of KH models ranges from single-yield surface models to more complex models incorporating multiple and even infinite yield surfaces. This hierarchy provides a progressively more nuanced understanding of material behavior, with each model building upon the principles established by its predecessors. This section delineates these models and their respective formulations.

The yield surface in a von Mises material, for example, can be represented by the equation:

The simplest KH model involves a single yield surface that translates in the stress space as plastic deformation occurs. This model is pivotal in understanding basic KH where the yield surface moves without changing its size or shape. This model is characterized by the energy potential say Gibbs free energy (or Helmholtz free energy), the dissipation function, yield function, and the evolution of the internal kinematic variable (back-stress). The general equations are presented below.

$$g = g(\sigma_{ij}, \alpha_{ij})$$
$$d = d(\dot{\epsilon}_{ij}^{P})$$
$$f = f(\sigma_{ij}, \alpha_{ij}) = 0$$

The specific Gibbs free energy function g is a function of the stress tensor σ_{ij} and a single internal kinematic variable tensor α_{ij}. The dissipation function d relates to the plastic strain rate tensor $\dot{\epsilon}_{ij}^{P}$. The yield function f defines the yield surface in the stress space, while the evolution of the internal kinematic variable α_{ij} is governed by the KH rule often attributed to Prager's rule is given by:

$$\dot{\alpha}_{ij} = C.\dot{\epsilon}_{ij}^{P}$$

Where C is a stiffness constant which can be interpreted as the plastic stiffness matrix. The single yield surface model results in a bilinear elastoplastic response, with stiffness controlled by elastic moduli within the yield surface and hardening moduli at the surface. For simplicity, α_{ij} will be referred to as the internal variable.

Next in the hierarchy is the multiple yield surfaces KH models. This concept, introduced by Iwan (1967) and Mróz (1967), extends the single yield surface model by incorporating several yield surfaces. Introduction of models with multiple yield surfaces allows to better capture the nonlinear and cyclic behavior of materials. These models use a finite number of yield surfaces, each associated with its internal variables which also implies each associated with a different level of plastic deformation. Each yield surface in this model is defined similarly to the single yield surface model. The general equations are presented below.

$$g = \sum_{n=1}^{N} g_n(\sigma_{ij}, \alpha_{ij}^{n})$$
$$d = \sum_{n=1}^{N} d_n(\dot{\epsilon}_{ij}^{P,n})$$
$$f_n = f_n(\sigma_{ij}, \alpha_{ij}^{n}) = 0$$
$$\dot{\alpha}_{ij}^{n} = C.\dot{\epsilon}_{ij}^{P,n}$$

Here the Gibbs free energy is presented for N yield surfaces, the dissipation function incorporates multiple internal variables α_{ij}^{n}, f_n for each yield surface, and α_{ij}^{n} for the evolution of each internal variable α_{ij}^{n}. This approach reduces the size of the true linear elastic region and allows for a piecewise linear approximation of the material's nonlinear behavior. It also introduces a memory of stress reversals, reflected in the configuration of the yield surfaces. This model is capable of capturing the Bauschinger effect and provides greater accuracy in modeling cyclic plasticity, as each yield surface can move independently, representing different stages of material hardening.

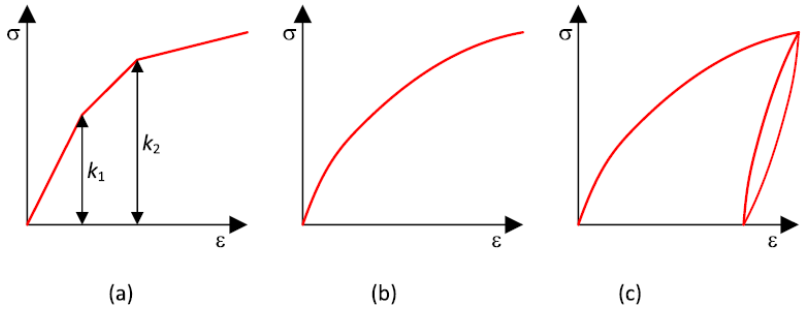

Figure 2. 1. KH Models Plasticity Model (a) $N = 2$; (b) $N = \infty$; (b) Hysteresis Loop (Houlsby et al., 2017).

Ultimately in the hierarchy is the infinite number of yield surfaces which is continuous KH based on hyperplasticity, and it's the most advanced in the hierarchy of KH models. To take the concept of multiple yield surfaces to its logical conclusion, an infinite number of yield surfaces is introduced, allowing for a smooth transition between elastic and plastic behavior, thus, providing a detailed representation of material response. This continuous approach leads to models with a continuous field of yield surfaces. Here g is taken as "potential functional" and d as "dissipation functional" – instead of the discrete internal variables, internal functions $\alpha_{ij}(r)$ are used, where r represent a continuous parameter, thus, $\alpha_{ij}(r)$ denotes a continuous distribution of back-stress tensors.

$$g = \int_0^1 g\,(r, \sigma_{ij}, \alpha_{ij}(r))dr$$

$$d = \int_0^1 d\,(r, \dot{\epsilon}_{ij}^P, \alpha_{ij}(r))dr$$

The yield surface function becomes a continuous function. Likewise, the evolution of the internal function is given below.

$$f = f\left(r, \sigma_{ij}, \alpha_{ij}(r)\right) = 0$$

$$\dot{\alpha}_{ij}^n(r) = C(r).\dot{\epsilon}_{ij}^P$$

This approach offers a highly accurate representation of nonlinear material behavior across a wide range of strain amplitudes, with the added advantage of a reduced number of material parameters. It is the most effective in capturing complex behaviors such as smooth hysteresis loops and gradual transitions between loading and unloading paths. However, it requires the specification of certain continuous functions, adding complexity to the model.

The hierarchy of KH models progresses from single-yield surface models to multiple-yield surfaces, culminating in continuous KH hyperplasticity models. Each level of this hierarchy offers increased accuracy in modeling material behavior at the cost of increased complexity in the formulation and computation. The selection of appropriate model complexity depends on the specific requirements of the material behavior to be captured. Typically, for balance in accuracy and efficiency, the multiple-yield surfaces models are usually sufficient.

2.3 Kinematic Hardening in Series and Parallel

The illustration of the behavior of the MSKH model based on the translation of the yield surfaces is shown in Figure 2.2. below, followed by the definition and description of KH models in series and parallel.

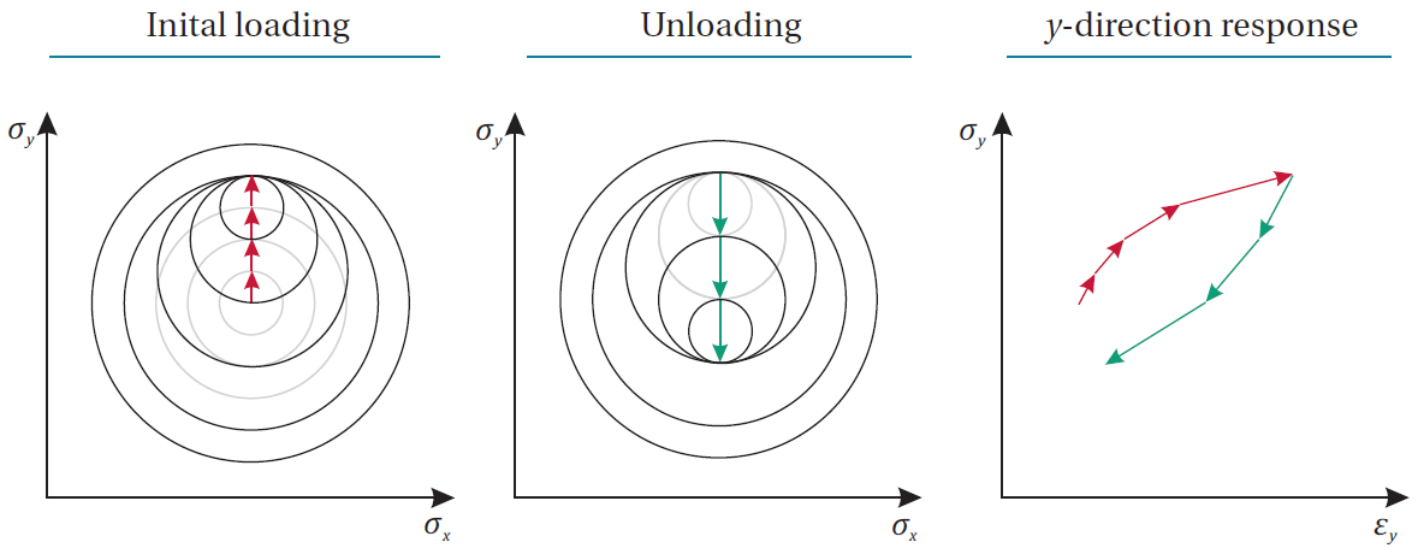

Figure 2. 2. Evolution of the Yield Surface in MSKH – Loading & Unloading (Richards, 2019).

The series and parallel models in the context of KH represent two different ways of combining individual elements i.e. springs-sliders units to model the behavior of a material under stress. The difference between the two arrangements is presented below:

(1) Series Model: In the series model, the elements are arranged end-to-end, like a chain. The same force is applied to all elements, but the total strain (deformation) is the sum of the strains in each element. This model is often used when the deformation of the material is more important than the force applied.

(2) Parallel Model: In the parallel model, the elements are arranged side-by-side. The same strain is applied to all elements, but the total stress (force) is the sum of the stresses in each element. This model is often used when the force applied to the material is more important than the deformation.

In terms of the KH model, the hardening strength (k) and hardening modulus (H) parameters have different physical interpretations in the series and parallel models. In the series model, k_n represents the stress at each breakpoint and H_n represents the hardening modulus at each stage (nth). In the parallel model, k_n can be thought of as the yield stresses of the individual parallel elements, and H_n as their hardening moduli. The choice between the series and parallel model depends on the specific application and the properties of the material being modeled including rate dependency.

2.3.1 S-Kinematic Hardening Formulation: Using Helmholtz Free Energy Function & Dissipation Function Approach (Rate Independent Method)

Derivation of KH in series (S-Kinematic Hardening) based hyperplasticity framework according to the work of Houlsby et al. (2017) is presented here.

$$S(x) = sign(x) = \begin{cases} 1 & if\ x > 0 \\ 0 & if\ x = 0 \\ -1 & if\ x < 0 \end{cases}$$

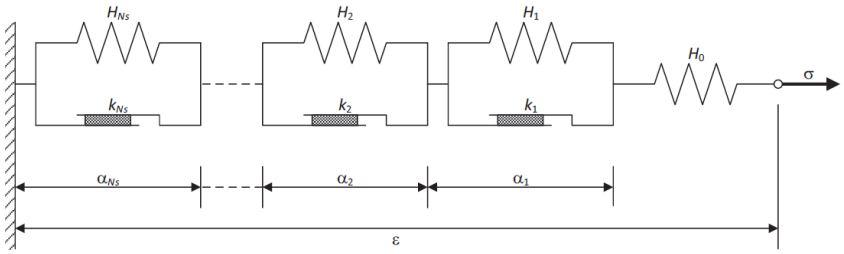

Figure 2. 3. KH Model in Series (Houlsby et al., 2017).

Step-by-step derivation and explanation:

(1) Helmholtz Free Energy Function: The Helmholtz free energy definition for a kinematic hardening model in series is given as,

$$f = \frac{H_0}{2}\left(\epsilon - \sum_{n=1}^{N_s} \alpha_n\right)^2 + \sum_{n=1}^{N_s} \frac{H_n}{2}\alpha_n^2$$

Where H_0 is the initial modulus, ϵ is total strain, α_n is internal strain variables (plastic strains) and H_n is the hardening moduli. At this stage, the ratcheting term in the form of ratcheting strain α_r does not come into play. This function represents the stored elastic energy. The first term penalizes the deviation of the total strain from the sum of the plastic strains, and the second term penalizes the magnitude of individual plastic strains.

(2) Dissipation Function: Likewise, the dissipation function is given as,

$$d = \left(\sum_{n=1}^{N_s} k_n \left|\dot{\alpha}_n\right|\right)$$

Where k_n is yield stress threshold for each spring-slider unit (dissipation coefficients) and $\dot{\alpha}_n$ is rates of plastic strains. This function represents the rate of energy dissipation due to plastic deformation. Again, the ratcheting contribution is eliminated at this stage. This will be added in the HARM formulation.

(3) Governing Equations: Stress-strain relationship derived from the Helmholtz free energy,

$$\sigma = \frac{\partial f}{\partial \epsilon} = H_0\left(\epsilon - \sum_{n=1}^{N_s} \alpha_n\right)$$

Back-stress for each plastic strain variable:

$$\bar{\chi}_n = -\frac{\partial f}{\partial \alpha_n} = H_0\left(\epsilon - \sum_{n=1}^{N_s} \alpha_n\right) - H_n\alpha_n = \sigma - H_n\alpha_n \qquad n = 1 \ldots N_s$$

(4) Incremental Formulation: The incremental stress-strain relationship,

$$\delta\sigma = H_0\left(\delta\epsilon - \sum_{n=1}^{N_s} \delta\alpha_n\right)$$

Yield condition (assuming a linear KH model):

$$|\sigma - H_n\alpha_n| < k_n \Rightarrow \delta\alpha_n = 0$$
$$|\sigma - H_n\alpha_n| = k_n \Rightarrow \delta\alpha_n \neq 0$$

Consistency condition:

$$\delta\sigma = H_n\delta\alpha_n$$

These relationships allow to update the stress and plastic strain variables incrementally.

(5) Stress-Strain Curve and Tangent Moduli: Given a stress-strain ($\sigma - \varepsilon$) curve based on the KH model in series form formulation as input, the breakpoints in the piece-wise stress-strain curves and the tangent moduli are defined by;

$$\sigma_n = k_n \qquad n = 1 \dots N_s$$
$$\epsilon_n = \sum_{i=0}^{n-1} \left(\frac{k_n - k_i}{H_i} \right) \qquad n = 1 \dots N_s$$

Defining;

$$k_0 = 0$$
$$\frac{1}{E_n} = \sum_{i=0}^{n} \left(\frac{1}{H_i} \right) \qquad n = 0 \dots N_s$$

From the above KH equations in series, calibration parameters like k_n, H_n and N_s can be easily extracted. These parameters help in calibrating the model to match experimental or FEA data accurately. They enable the reproduction of the constitutive relation of the backbone curve to any level of accuracy needed.

2.3.2 P-Kinematic Hardening Formulation: Using Helmholtz Free Energy Function & Dissipation Function Approach (Rate Independent Method)

Derivation of KH in parallel (P-Kinematic Hardening) based hyperplasticity framework according to the work of Houlsby et al. (2017) is presented here.

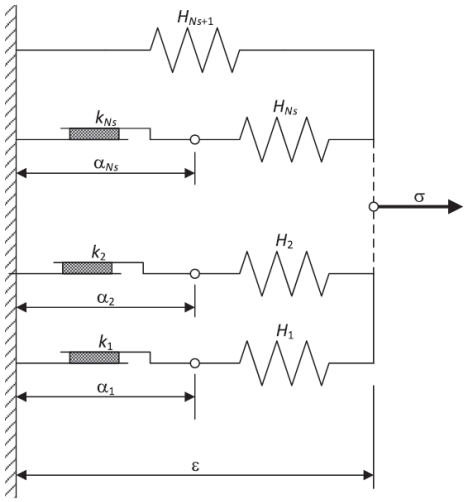

Figure 2. 4. KH Model in Parallel (Houlsby et al., 2017).

Step-by-step derivation and explanation:

(1) Helmholtz Free Energy Function: The KH formulation in parallel is the same as the series model in terms of the output for a case of a one-dimensional model. Therefore, either approach can be used for 1D analysis. The Helmholtz free energy definition for a KH model in parallel is given as;

$$f = \sum_{n=1}^{N_s} \frac{H_n}{2} (\epsilon - \alpha_n)^2 + \frac{H_{N_s+1}}{2} \epsilon^2$$

Where H_n is the initial modulus for plastic strain components, $H_{N_s+1}$is hardening modulus for elastic strain component. This function represents the stored energy due to both the elastic and plastic components of the strain.

(2) Dissipation Function:

$$d = \left(\sum_{n=1}^{N_s} k_n \left| \dot{\alpha}_n \right| \right)$$

This function represents the rate of energy dissipation due to plastic deformation. Just like in the series formulation, ratcheting terms are not included at this stage of the model.

(3) Governing Equations: Stress-strain relationship derived from the Helmholtz free energy,

$$\sigma = \frac{\partial f}{\partial \epsilon} = \sum_{n=1}^{N_s} H_n \left(\epsilon - \alpha_n \right) + H_{N_s+1} \epsilon$$

Back-stress for each plastic strain variable:

$$\bar{\chi}_n = -\frac{\partial f}{\partial \alpha_n} = H_n (\epsilon - \alpha_n) \qquad n = 1 \dots N_s$$

(4) Incremental formulation: The incremental stress-strain relationship,

$$\delta\sigma = \sum_{n=1}^{N_s} H_n \left(\delta\epsilon - \delta\alpha_n \right) + H_{N_s+1} \delta\epsilon$$

Yield condition:

$$|\sigma - H_n(\epsilon - \alpha_n)| < k_n \Rightarrow \delta\alpha_n = 0$$
$$|\sigma - H_n(\epsilon - \alpha_n)| = k_n \Rightarrow \delta\alpha_n \neq 0$$

Consistency condition:

$$\delta\sigma = H_n \delta\alpha_n$$

(5) Stress-Strain Curve and Tangent Moduli: Given a stress-strain ($\sigma - \varepsilon$) curve based on the KH model in parallel form formulation as input, the breakpoints in the piece-wise stress-strain curves and the tangent moduli are defined by;

$$\sigma_n = \sum_{i=1}^{n} k_i + \sum_{i=n+1}^{N_s+1} H_i \epsilon_n = \sum_{i=1}^{n} k_i + \left(\frac{k_n}{H_n} \right) \sum_{i=n+1}^{N_s+1} H_i \qquad n = 1 \dots N_s$$

$$\epsilon_n = \frac{k_n}{H_n} \qquad n = 1 \dots N_s$$

$$E_n = \sum_{i=n+1}^{N_s+1} H_i \qquad n = 0 \dots N_s$$

(6) Numerical Implementation:

In the numerical implementation of the parallel model, the above E_n formula is represented within the Gibbs free energy formulation as;

$$E_0 = \sum_{n=1}^{N_s+1} H_n$$

2.4 Masing Rule

The Masing rule is a concept used to describe the hysteresis behavior of materials under cyclic loading. It provides a way to generate the cyclic stress-strain curve from the monotonic (static) stress-strain curve. According to the Masing rule (Masing, 1926), if the monotonic stress-strain curve of a material which is the backbone curve is described by a function $\sigma = f(\epsilon)$; then upon load reversals, the relationship returns to the maximum tangent modulus also known as

the initial elastic modulus (Rule 1). Furthermore, the cyclic stress-strain curve can be obtained by scaling the stress and strain by a factor of two when unloading and reloading (Rule 2). Mathematically, for a half-cycle starting from the reversal point (σ_r, ϵ_r), the stress-strain relationship can be written as:

$$\sigma - \sigma_r = 2f\left(\frac{\epsilon - \epsilon_r}{2}\right)$$

The above mathematical equation simply means that the cyclic stress-strain curve can be obtained by taking the backbone curve and doubling the strain for a given stress during the unloading and reloading phases. The rule describes how this static behavior can be modified to represent cyclic loading.

2.5 Rate-Dependent and Rate-Independent Models

The hyperplasticity approach allows constitutive models to be developed based on hypotheses for the storage and dissipation of energy, while the entire material response is derived from knowledge of two potential functions which allows models to be very simply defined, classified, and if necessary, developed. The theory in the hyperplasticity framework is extended to include the treatment of rate-dependent materials and introduces a powerful concept, in which a single plastic strain is replaced by a plastic strain function, allowing smooth transitions between elastic and plastic behavior (Houlsby & Puzrin, 2006). Understanding how materials respond to different loading rates is essential for predicting their behavior under various conditions. This understanding is achieved through the development of rate-dependent and rate-independent models. These models are integral to describing a material's response to applied stresses and strains.

2.5.1 Rate-Independent Models

Rate-independent models assume that the material's response is not affected by the rate of loading. These models are suitable for elastoplastic materials that exhibit the same behavior regardless of the loading rate, capturing elastic behavior up to a yield point followed by plastic deformation without any time-dependent effects. The models can capture hysteresis behavior observed in cyclic loading, where the material's response depends on its loading history. The general form of the constitutive equation for a rate-independent model can be expressed as:

$$\sigma = g(\epsilon)$$

Where σ is the stress tensor and ϵ is the strain tensor. For instance, in the von Mises plasticity model, the yield function f is defined as:

$$f(\sigma, \epsilon^P) = 0$$

Where ϵ^P is the plastic strain. At $f < 0$, the material is in an elastic state, and no plastic deformation occurs, but at $f = 0$, the material is at the yield point, and plastic deformation begins. However, in constitutive modelling $f > 0$ is not a valid or meaningful condition, and does not have a physical meaning, as the yield function is no longer a boundary. Instead, at this point, the hardening rules govern the evolution of the yield surface, ensuring the material's behavior is accurately modelled. The hardening rule can be kinematic hardening i.e. translation of yield surface or isotropic hardening i.e. expansion of the yield surface. Though, for offshore foundation modelling and a realistic representation of most engineering material response under cyclic loading, the KH rule is considered more accurate and valid because it captures the material's response to cyclic loading, it accounts for the Bauschinger effect which describes the material's reduced yield stress after reverse loading, and more importantly it incorporates material memory, allowing the material to remember its previous loading history.

The dissipation potential d (assuming associative flow rule) in rate-independent models is a function of the plastic strain rate $\dot{\epsilon}^P$, ensuring that the second law of thermodynamics is satisfied, which means entropy production is always non-negative:

$$d(\dot{\epsilon}^P) \geq 0$$

The gradient of d with respect to the plastic strain rate gives the dissipative forces used in the flow rule.

$$\sigma = \frac{\partial d}{\partial \dot{\epsilon}^P}$$

2.5.2 Rate-Dependent Models

Rate-dependent models, also known as viscoplastic models, account for the time-dependent behavior of materials. These models are essential for materials that exhibit different responses at varying strain rates. The material's response depends on the rate at which the load is applied; faster loading rates can lead to different stress-strain responses compared to slower rates. Viscoplastic models combine both viscous and plastic behavior, allowing for the description of materials that exhibit both time-dependent and permanent deformation. The constitutive equations for rate-dependent models incorporate time as an explicit variable:

$$\sigma = f(\epsilon, \dot{\epsilon}, t)$$

Where $\dot{\epsilon}$ is the strain rate tensor and t is the time. In the Perzyna (Perzyna, 1966) viscoplastic model, the yield function f is modified to include a rate-dependent term:

$$f(\sigma, \epsilon^P, \dot{\epsilon}^P) = 0$$

The d in rate-dependent models is a function of both the plastic strain rate $\dot{\epsilon}^P$ and time t:

$$d(\dot{\epsilon}^P, t) \geq 0$$

Similarly, the gradient of d with respect to the plastic strain rate provides the dissipative forces used in the flow rule:

$$\sigma = \frac{\partial d}{\partial \dot{\epsilon}^P}$$

In rate-dependent models, the material's energy dissipation is viscous. Thus, the rate-independent model could be interpreted as a rate-dependent model with artificially infinitesimal viscosity. This statement could be useful when transforming from a rate-dependent to a rate-independent assumption.

2.5.3 Material Testing Application

Material testing is crucial for both rate-independent and rate-dependent models to capture the accurate response of materials under different loading conditions. For rate-independent models, testing focuses on the material's response to different stress or strain states, regardless of the loading rate. Common tests include uniaxial tensile tests and cyclic loading tests to observe the hysteresis behavior and permanent deformations. However, in rate-dependent models, testing involves varying the strain rate to observe the material's time-dependent behavior. Common tests include creep tests where slow, time-dependent deformation under constant stress is observed, and stress relaxation tests where a decrease in stress under constant strain is observed.

The hyperplasticity framework provides a systematic and thermodynamically consistent approach to developing both rate-independent and rate-dependent models. By incorporating the concept of dissipation potential, these models ensure the second law of thermodynamics is satisfied and are capable of accurately describing the material's response under various loading conditions. Understanding the distinctions and applications of these models is crucial for precise material testing and for predicting material behavior in constitutive modelling.

2.6 Modes of Load Application in Macro-element Modelling

Two different modes of load application to describe constitutive relationships are the force-controlled and displacement-controlled modes. In force-controlled constitutive behavior, the approach assumes that the stress is the independent variable, and the resulting strain is the dependent variable. In other words, the material's deformation is a response to the applied force. In displacement-controlled constitutive behavior, the approach assumes that the strain is the independent variable, and the resulting stress is the dependent variable. In other words, the material's stress state is a response to the applied deformation.

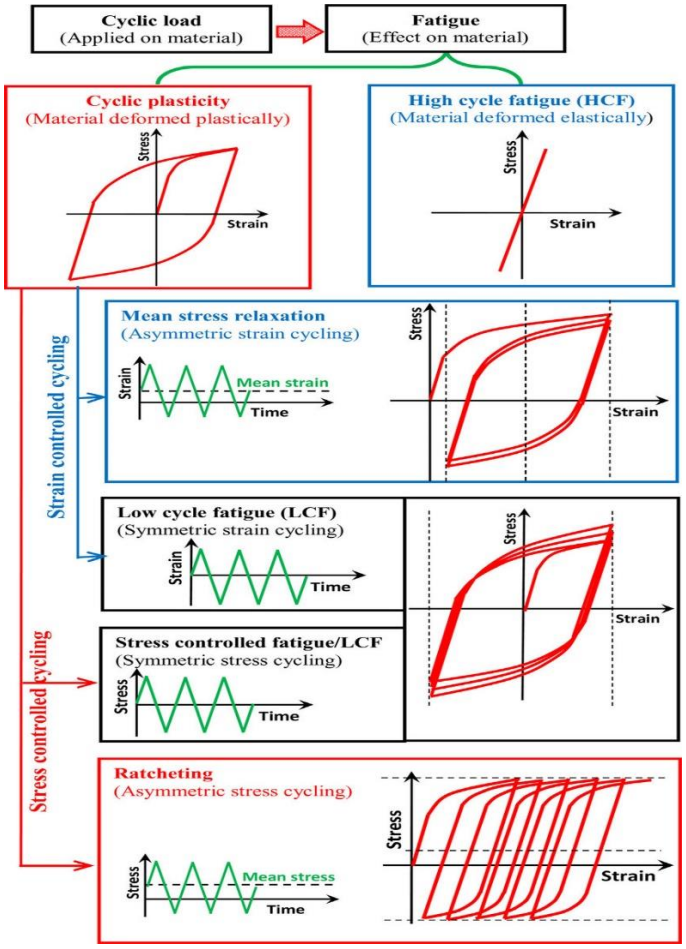

Figure 2. 5. Displacement-Controlled and Force-Controlled Representation of Cyclic Response (Paul, 2019).

In the context of KH and then HARM implementation, KH in series and parallel are suitable for stress/load-controlled and strain/displacement conditions respectively.

In macro-element modelling, constitutive relationships in stress-strain, force-displacement, and moment-rotation are all equivalent and valid. For fair comparison and scaling from different research works and experiments, these relationships are typically normalized. Normalization of the force can be done with respect to the ultimate limit state (ULS) value, while that of displacement can be done with respect to 10 % of the pile diameter.

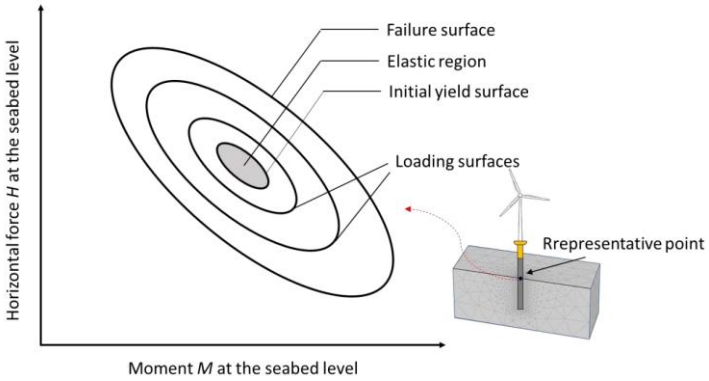

Figure 2. 6. MSKH States under Macro-Element Model (Liu et al., 2023).

3. HARM AND REDWIN CONSTITUTIVE MODELS

3.1 The HARM Model

3.1.1 Overview of the HARM Model

The Houlsby-Abadie Ratcheting Model (HARM), is a constitutive model used to describe the behavior of materials, particularly in offshore soil foundations, under cyclic loading conditions. HARM is designed to capture the nonlinear response of materials during loading, hysteretic behavior during unloading and reloading, and the ratcheting phenomenon over a large number of cycles.

In engineering materials applications, there are conditions where a material exhibits nonlinear behavior under cyclic loading, including hysteresis during unloading and reloading cycles. With an increasing number of large cycles over time, there is a gradual accumulation of irreversible strain or deformation, known as ratcheting, which results in permanent deformation. This is especially relevant for OWTs supported on monopile foundations, which experience varying cyclic loads due to waves, currents, and wind direction bias, making ratcheting a potential concern (Houlsby et al., 2017).

HARM is rigorously formulated to account for the effects of plastic strains due to ratcheting, capturing the response of soil foundations to numerous cycles of loading. Ratcheting, a fraction of the plastic strain accumulated with cycles, is dissipative, leading to energy loss physically interpreted by the formation of hysteresis loops. The energy dissipation and damping based on hysteresis loops, with increments due to the sum of ratcheting strain/displacement, are analogous to the energy dissipation in Kolmogorov's cascade, where the size of the vortices decreases with energy dissipation, converting to heat and increased viscosity, resulting in damping. Similarly, the size of the hysteresis loops decreases with an increasing cycle number.

Researchers have developed theoretical models within the hyperplastic framework to describe the response of one-dimensional mechanical systems under cyclic loading. These models address the nonlinear response during loading, hysteretic behavior during unloading and reloading, and the ratcheting phenomenon over many cycles. The model can be expressed using general incremental relationships and applied directly to any loading history, making its implementation within numerical codes straightforward using time-stepping methods (Houlsby et al., 2017).

The calibration of the HARM model involves fitting one test response and a few continuous cyclic tests to a closed-form expression for the accumulation of ratcheting strain with cyclic history (Abadie et al., 2019). This process ensures that the model accurately reflects the material’s behavior under cyclic loading conditions.

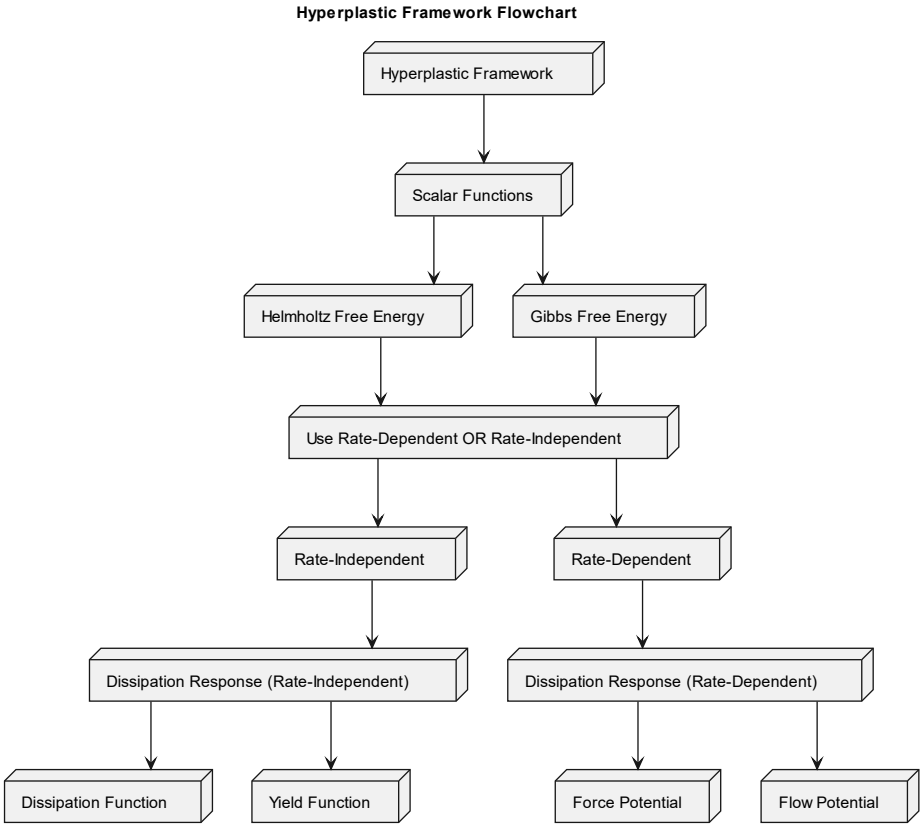

Figure 3. 1. Flow Chart on Implementation of Hyperplasticity Framework using Two Potentials.

3.1.2 Literature Review on HARM

Origination of the Constitutive Model

Houlsby & Puzrin (1999) presented a thermomechanical framework for rate-independent dissipative materials with thermodynamic potentials. The constitutive behavior is determined by two scalar potentials in 16 ways of formulation. The elastoplastic theory for rate-independent materials using thermodynamic potentials is described; the dissipative behavior is introduced via kinematic internal parameters and the use of dissipation function or yield function to describe irreversible behavior. The paper is an extension of the work by Collins & Houlsby (1997) by including and accounting for thermal effects.

Houlsby & Puzrin (2002) studied the rate-dependent plasticity models derived from potential functions in metallic glass. The temperature-dependent dynamics in the metallic glass plasticity are analyzed based on potential functions (thermodynamic laws compliant potentials). The paper extended the rate-independent plasticity theory to rate-dependent behavior, offering insights into rate-dependent materials based on rate-independent cases, and focused on deriving constitutive responses from force and flow potentials, and exploration of the relationships between the choices of potential functions. The constitutive models are derived using two scalar potential functions thus, material behavior is specified through energy and dissipation response functions.

Houlsby & Puzrin (2006) explored mass conservation and dissipation functions in mathematical equations. The paper established thermodynamic laws (zeroth, first, second, and third laws) about plasticity theory; defined closed systems, state variables, properties, and equations of state; defined materials in geomechanics within a rigorously defined thermodynamic approach; introduced assumption to derive evolution equations for internal variables; determined constitutive behavior through generalized stresses and dissipation functions i.e. based on two scalar potential functions only; and addressed plastic potential and stress-strain behavior. Houlsby & Puzrin extended the hyperplasticity principles

to large strains, fluid flow, and heat flow. The model accurately captures transition in clay behavior under different strain rates. Six material parameters have been used to predict diverse behavior with high accuracy.

Frederick & Armstrong (2007) proposed a new material model for accurate plasticity representation in inelastic stress analysis and evaluation of constants from tensile stress-strain curve for the behavior model and Prager yield criterion. The multiaxial Bauschinger effect is represented mathematically based on various models' capabilities. The proposed model in the paper predicts the convergence of cyclic stress-strain curves, and the extension of the behavior model to include time-dependent effects is discussed. The paper aimed at addressing the inadequacies in existing models for Bauschinger effect representation, and the need for improved mathematical models for time-independent plasticity. The model limitation is that the A-F rule (Armstrong & Frederick) predicts excessive ratcheting under non-symmetric loading conditions, and the difficulty in handling strain direction changes within a fixed length.

Development of HARM

Abadie (2015) researched cyclic loading of monopile foundations in cohesionless soils; and also, the experimental and theoretical study to improve understanding of the pile behavior and identify key mechanisms driving pile response. The author's work encompasses a study of the experimental and theoretical aspects to understand pile behavior under cyclic loading, and the development of a constitutive model called HARM for accurate prediction of pile response. The calibration methodology is based on selected test results for model parameters. Findings for the paper showed that pile response conforms to extended Masing rules with permanent deformation, as multi-amplitude loading scenarios interaction is used to describe the pile response; ratcheting behaviour is characterized by decreasing rate and tightening hysteresis loop; the HARM model captures ratcheting and conforms to observed Masing behaviour under monotonic and cyclic loading. Research limitations indicate that pile dimensions differ from oil and gas platform piles, and thus standard design techniques may lack confidence due to these differences.

Houlsby et al. (2017) presented the HARM model for hyperplasticity in materials, ensuring mathematical conciseness and adherence to the thermodynamic laws. The paper presents a model for cyclic loading in mechanical systems, addressing nonlinear response, ratcheting, hysteretic behavior under loading, and multidirectional loading behavior. A framework extending the model from 1D to 2D problems with wider applicability is presented. The paper addresses the limitation of existing models in over-predicting ratcheting strain, and initial cyclic load response not conforming to Masing rules. Findings indicated that 1D models can simulate ratcheting phenomena with extensions, and the models accommodate reduced ratcheting rate, increased secant stiffness, and hysteresis changes (reduced hysteresis).

Applications and Extensions of HARM

Abadie et al. (2017) studied rigid monopile response to cyclic lateral loading in sand; conducted experimental tests based on 1 g model tests in sand with up to 100, 000 cycles focusing on key response mechanisms; extension of the HARM constitutive model to capture pile response more accurately and discussion of calibration methodology based on experimental results for complex load scenarios. The results from moment-rotation curves indicated ratcheting dominance, while at the same time conforming to Masing rules. Key mechanisms observed are grouped into Masing behavior conformity and accumulated ratcheting deformation. The paper aimed to address the lack of fundamental behavior description of soil-pile response based on the existing semi-empirical models; and the difficulty in adapting load packets at different amplitudes with some assumptions.

Richards (2019) investigated monopile foundations under complex cyclic lateral loading explored through physical modeling. A novel laboratory apparatus for complex cyclic loading applications was developed, hence, leading to informed and effective monopile design under realistic loading conditions. A numerical model based on a MSKH macro-element model is deployed to capture hysteretic response (no ratcheting at this stage), and then the HARM framework models predict ratcheting, hysteresis, and arbitrary loading response. The paper explored the impact of load amplitude, asymmetry, and multidirectional components, with results indicating the dominance of large load events in response to realistic loading; and qualitatively similar behavior in very loose and dense sand are observed.

Further Validation and Optimization of HARM

Beuckelaers (2017) investigated the behavior of monopile foundations for OWTs using numerical modeling; and also, the development of advanced plasticity models based on the hyperplasticity framework integrated within a generalized Winkler model (1D model) to improve the foundation design accuracy. Advanced numerical modeling techniques were deployed to investigate monopile behavior to reduce design conservatism for wind turbines. Field testing provided data on rate effects and cyclic behavior hence, the data is used to validate the numerical models for foundation response prediction accuracy under monotonic and cyclic loading. Furthermore, soil reaction models for plastic unloading, rate effects, and ratcheting were developed. The paper aimed to address the lack of cyclic loading effects and loading rate considerations in OWT design.

Abadie et al. (2020) modeled monopile response to lateral cyclic loading for OWTs; combining the PISA design model with the HARM framework for performance assessment/prediction with a focus on ultimate capacity and deformation limitations over 25 years including determining the in-service performance of offshore monopile subjected to the storm. The paper attempted to address the lack of detailed 1D layered model adaptation for HARM formulation, and the insufficient exploration of more rigorous approaches for SLS and FLS (Fatigue Limit State) design. Abadie et al. contributed to improved design guidelines for ULS conditions using PISA and HARM methods, as well as a numerical modeling approach for predicting pile ULS, SLS, and FLS performance. Results indicated that the model captured a monopile response to 3×10^8 cycles in 30 minutes, with calibration of ratcheting behaviour achieved through choice of ratcheting rate.

Abadie et al. (2023) modeled cyclic loading for wind turbine foundations using HARM (0D and 1D) to predict accurately pile response to operational and extreme loads efficiently over the lifetime. The paper emphasized global moment-rotation response prediction of the monopiles, and demonstration of model application to pile field testing for wind turbines with a focus on computational efficiency while maintaining high calculation accuracy. The paper aimed to close the gap in the lack of understanding calibration process of local soil reaction, and the importance of stress level and scale exploration. The HARM model is validated against PISA cyclic tests and applied to extreme scenarios, and the residual pile deflection was found to be below the design limit for extreme cyclic loading ($< 0.5°$ over the lifetime) and for various loading scenarios with promising capabilities and potential for computational optimization of monopile foundation design to large cycle numbers.

HARM provides valuable insights into the behavior of materials subjected to cyclic loading, especially when ratcheting effects are significant. This comprehensive understanding is crucial for optimizing the design and ensuring the long-term structural integrity of OWT foundations under complex loading conditions. In the area of OWT foundation application, the model is particularly very useful for predicting the behavior of the foundation to accumulated deformations due to ratcheting where cyclic loading is very dominant. Other aspects where this model is applicable are in OWT structural fatigue analysis, structural health monitoring (SHM), and structural damage detection and prognosis. Aside from offshore soil foundation application, this model can be extended to materials such as metals, polymers, and composites.

3.1.3 S-HARM Formulation: Using Helmholtz Free Energy Function & Dissipation Function Approach (Rate Independent Method)

Derivation of HARM in series (S-HARM) based hyperplasticity framework according to the work of Houlsby et al. (2017) is presented here. The back-stress or internal KH variable is directly related to the plastic strain since the back-stress evolves with the accumulation of plastic strain. Under the HARM implementation, the plastic strain part of the total strain (ϵ) will be denoted as α_n where n is the index of the yield surface. This shouldn't be confused with the general back-stress notation (α).

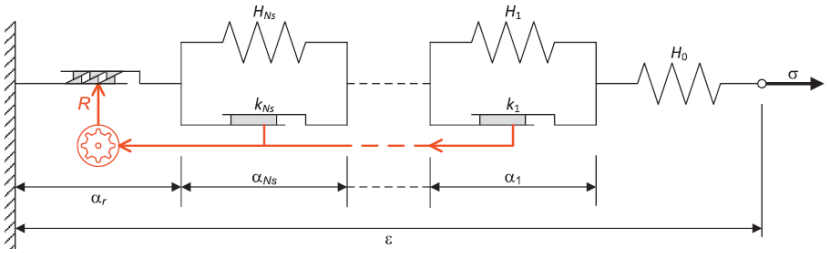

Figure 3. 2. HARM Model in Series (Houlsby et al., 2017).

Step-by-step derivation and explanation:

(1) Helmholtz Free Energy Function: The S-HARM formulation is completely defined with two scalar functions,

$$f = \frac{H_0}{2}\left(\epsilon - \sum_{n=1}^{N_s} \alpha_n - \alpha_r\right)^2 + \sum_{n=1}^{N_s} \frac{H_n}{2}\alpha_n^2$$

In the Helmholtz potential energy function, the first term penalizes the deviation of the total strain ϵ from the sum of the plastic strain α_n and the ratcheting strain α_r, while the second term penalizes the magnitude of the individual plastic strains. The number of yield surfaces is N_s and n is the index of the yield surface.

(2) Dissipation Function:

$$d = \left(\sum_{n=1}^{N_s} k_n \left|\dot{\alpha}_n\right|\right) + \sigma\dot{\alpha}_r$$

The dissipation function d now includes a term for the ratcheting strain rate $\dot{\alpha}_r$, accounting for energy dissipation due to ratcheting. In the dissipation function which includes plastic strain rate and ratcheting strain rate, the first term accounts for the dissipation due to plastic strain $\dot{\alpha}_n$ with strength coefficient k_n, while the second term accounts for the dissipation due to the ratcheting strain rate $\dot{\alpha}_r$ with stress/load coefficient σ.

(3) Ratcheting Constraint: In addition to the constraint defining the ratcheting strain,

$$c = \dot{\alpha}_r - S(\sigma)\sum_{n=1}^{N_s} R_n \left|\dot{\alpha}_n\right| = 0$$

Where $S(\sigma)$ is a sign function of stress, R_n is ratcheting parameters. The above constraint equation defines the ratcheting rate in terms of plastic strain rate and stress.

(4) Augmented Dissipation Function:

$$d^* = d + \Lambda c$$

$$\Lambda \Rightarrow \text{Lambda Capital Form}$$

Here Λ is the Lagrange multiplier.

The above equation introduces the Lagrange multiplier to incorporate the constraint function into the dissipation function.

(5) Governing Equations: The derivatives below are required for complete description of the model.

Stress-strain relationship:

$$\sigma = \frac{\partial f}{\partial \varepsilon} = H_0\left(\epsilon - \sum_{n=1}^{N_s} \alpha_n - \alpha_r\right)$$

Back-stresses for plastic strain and ratcheting strain:

These back-stresses here are known as the “generalized stresses/forces”.

$$\bar{\chi}_n = -\frac{\partial f}{\partial \alpha_n} = H_0\left(\epsilon - \sum_{n=1}^{N_s}\alpha_n - \alpha_r\right) - H_n\alpha_n = \sigma - H_n\alpha_n \qquad n = 1 \dots N_s$$

$$\bar{\chi}_r = -\frac{\partial f}{\partial \alpha_r} = H_0\left(\epsilon - \sum_{n=1}^{N_s}\alpha_n - \alpha_r\right) = \sigma$$

Dissipation function derivatives:

$$\chi_n = \frac{\partial d^*}{\partial \dot{\alpha}_n} = k_n\, S(\dot{\alpha}_n) - \Lambda S(\sigma) R_n S(\dot{\alpha}_n) \qquad n = 1 \dots N_s$$

$$\chi_r = \frac{\partial d^*}{\partial \dot{\alpha}_r} = \sigma + \Lambda$$

(6) Solving for Λ:
Thus, $\Lambda = 0$ can be derived.

$$\chi_r = \sigma \Rightarrow \Lambda = 0$$

(7) Final Incremental Relations:
Then;
Stress-strain relationship:

$$\sigma = H_0\left(\epsilon - \sum_{n=1}^{N_s}\alpha_n - \alpha_r\right)$$

Plastic strain rate relationship:

$$\sigma = k_n\, S(\dot{\alpha}_n) + H_n\alpha_n \qquad n = 1 \dots N_s$$

Yield condition and consistency condition:

$$|\sigma - H_n\alpha_n| < k_n \Rightarrow \delta\alpha_n = 0$$

The above indicates that yielding does not occur. The condition below indicates yielding can occur.

$$|\sigma - H_n\alpha_n| = k_n \Rightarrow \delta\alpha_n \neq 0$$

$$\delta\sigma = H_n\delta\alpha_n$$

Ratcheting strain increment:
Together with;

$$\delta\alpha_r = S(\sigma)\sum_{n=1}^{N_s} R_n|\delta\alpha_n|$$

This relationship fully defines incrementally the elastoplastic behavior.
(8) Numerical Implementation: For numerical implementation in incremental constitutive behavior (stress-strain relationship),

$$\delta\sigma = H_0\left(\delta\epsilon - \sum_{n=1}^{N_s}\delta\alpha_n - \delta\alpha_r\right)$$

Note that to achieve a ratcheting rate $\dot{\alpha_r}$ increase nonlinearly with an increase in the magnitude of stress; and reduction with an increase in the hardening parameter β i.e. for a normal regular cyclic loading with increasing cycle number – the ratcheting rate decreases, hysteresis loop indicating damping decreases, and secant stiffness increases (asymptotically towards the initial stiffness or elastic modulus); then the formulation for the ratcheting parameter R_n satisfying these criteria is given below.

$$R_n = R_0\left(\frac{k_n}{k_U}\right)\left(\frac{\beta}{\beta_0}\right)^{-m_r}\left(\frac{|\sigma|}{k_U}\right)^{m_s}$$

Where k_U is the upper value of k_n; β_0 and R_0 are the initial values of the hardening parameter and ratcheting parameter respectively. The constants m_r and m_s are ratcheting and stress exponents respectively. Implementation of S-HARM using Gibbs free energy & yield function approach is presented under Appendix B.

3.1.4 P-HARM Formulation: Using Helmholtz Free Energy Function & Dissipation Function Approach (Rate Independent Method)

Derivation of HARM in parallel (P-HARM) based hyperplasticity framework according to the work of Houlsby et al. (2017) is presented here.

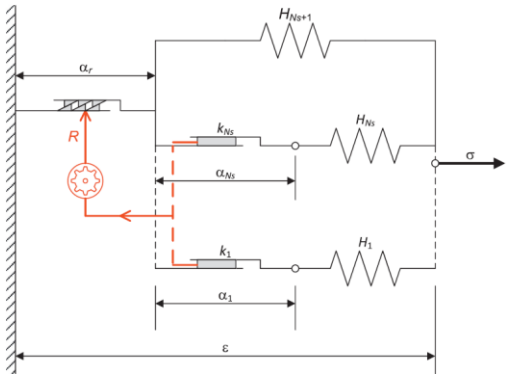

Figure 3. 3. HARM Model in Parallel (Houlsby et al., 2017).

Step-by-step derivation and explanation:

(1) Helmholtz Free Energy Function: The P-HARM formulation requires arrangement of the spring-slider units in parallel instead of series arrangement like in the case of S-HARM. This model is formulated through the functions below,

$$f = \sum_{n=1}^{N_s} \frac{H_n}{2}(\epsilon - \alpha_n - \alpha_r)^2 + \frac{H_{N_s+1}}{2}(\epsilon - \alpha_r)^2$$

The first term accounts for the energy due to plastic strains and ratcheting strain, while the second term is the energy due to ratcheting strain alone.

(2) Dissipation Function:

$$d = \left(\sum_{n=1}^{N_s} k_n \,|\dot{\alpha}_n|\right) + \sigma\dot{\alpha}_r$$

The dissipation function includes terms for plastic strain rates and the ratcheting strain rate.

(3) Ratcheting Constraint:

$$c = \dot{\alpha}_r - S(\sigma)\sum_{n=1}^{N_s} R_n \,|\dot{\alpha}_n| = 0$$

This constraint defines the ratcheting rate in terms of plastic strain rates and stress.

(4) Augmented Dissipation Function:

$$d^* = d + \Lambda c$$

Λ: Lagrange multiplier

Introducing the Lagrange multiplier incorporates the ratcheting constraint into the dissipation function.

(5) Governing Equations: Stress-strain relationship,

$$\sigma = \frac{\partial f}{\partial \epsilon} = \sum_{n=1}^{N_s} H_n\,(\epsilon - \alpha_n - \alpha_r) + H_{N_s+1}(\epsilon - \alpha_r)$$

Back-stresses for plastic strain and ratcheting strain:

Starting with the Helmholtz free energy function f, solving it requires taking the partial derivatives with respect to α_n and α_r, and setting them to zero to obtain mathematically the critical points.

$$\bar{\chi}_n = -\frac{\partial f}{\partial \alpha_n} = H_n(\epsilon - \alpha_n - \alpha_r) \qquad n = 1 \ldots N_s$$

$$\bar{\chi}_n = -\frac{\partial f}{\partial \alpha_n} = H_n(\epsilon - \alpha_n - \alpha_r) = 0$$

$$\bar{\chi}_r = -\frac{\partial f}{\partial \alpha_r} = \sum_{n=1}^{N_s} H_n\,(\epsilon - \alpha_n - \alpha_r) + H_{N_s+1}(\epsilon - \alpha_r)$$

$$\bar{\chi}_r = -\frac{\partial f}{\partial \alpha_r} = \sum_{n=1}^{N_s} H_n\,(\epsilon - \alpha_n - \alpha_r) + H_{N_s+1}(\epsilon - \alpha_r) = 0$$

The above equations yield the critical points for α_n and α_r, which can be solved simultaneously to get their respective values.

Dissipation function derivatives:

Similarly, the dissipation function can be solved by computing the derivative of d with respect to $\dot{\alpha}_n$ and $\dot{\alpha}_r$ respectively.

$$\chi_n = \frac{\partial d^*}{\partial \dot{\alpha}_n} = k_n\,S(\dot{\alpha}_n) - \Lambda S(\sigma) R_n S(\dot{\alpha}_n) \qquad n = 1 \ldots N_s$$

$$\chi_r = \frac{\partial d^*}{\partial \dot{\alpha}_r} = \sigma + \Lambda$$

(6) Solving for Λ:

Thus, $\Lambda = 0$ can be derived.

$$\chi_r = \sigma \Rightarrow \Lambda = 0$$

(7) Final Incremental Relations: Stress-strain relationship,

$$\sigma = \sum_{n=1}^{N_s} H_n\,(\epsilon - \alpha_n - \alpha_r) + H_{N_s+1}(\epsilon - \alpha_r)$$

Plastic strain rate relationship:

$$H_n(\epsilon - \alpha_n - \alpha_r) = k_n S(\dot{\alpha}_n) \qquad n = 1 \ldots N_s$$

Yield condition and consistency condition:

$$|\sigma - H_n(\epsilon - \alpha_n - \alpha_r)| < k_n \Rightarrow \delta\alpha_n = 0$$
$$|\sigma - H_n(\epsilon - \alpha_n - \alpha_r)| = k_n \Rightarrow \delta\alpha_n \neq 0$$
$$\delta\sigma = H_n \delta\alpha_n$$

Ratcheting strain increment:

To satisfy the constraint equation, the value of $\dot{\alpha}_r$ has to be in the form shown below.

$$\delta\alpha_r = S(\sigma) \sum_{n=1}^{N_s} R_n\,|\delta\alpha_n|$$

(8) Yield Function: The yield function (y_n) represents the condition under which yielding or plastic deformation occurs. In the P-HARM formulation, the yield function can be defined for each of the spring-slider units (n) as follows,

$$y_n = |\sigma - H_n(\epsilon - \alpha_n - \alpha_r)| - k_n$$

Stress is represented as σ; the hardening modulus/stiffness associated with the nth spring-slider unit as H_n; the total strain as ϵ; plastic strain associated with the nth spring-slider unit as α_n; the ratcheting strain as α_r; and the threshold value of the yield stress for the nth spring-slider unit as k_n.

If the yield function (y_n) is less than zero yielding does not occur for the nth spring-slider unit, and may occur if equal to zero (though theoretical ≤ 0 yield does not occur). Otherwise, yield occurs indicating that plastic deformation has taken place. Furthermore, it is worth knowing that y_n represents the condition where the stress σ exceeds the effective stress due to plastic strain $H_n(\epsilon - \alpha_n - \alpha_r)$ by an amount greater than k_n. Once this condition is satisfied, yielding occurs.

(9) Numerical Implementation: The formulation for the ratcheting parameter R_n is given below.

$$R_n = R_0 \left(\frac{k_n}{k_U}\right)\left(\frac{\beta}{\beta_0}\right)^{-m_r}\left(\frac{|\sigma|}{k_U}\right)^{m_s}$$

The variables and parameters in P-HARM is different from that of S-HARM in term of physical interpretation. Implementation of P-HARM using Gibbs free energy & yield function approach is presented under Appendix C.

3.1.5 Numerical Simulation based on S-HARM

Numerical example on S-HARM calibrated to PISA CM9 test (Cowden clay) and DM4 test (Dunkirk sand). For an efficient implementation, power law is fitted to the backbone curves of these tests according to the equations below:

$$\text{CM9: } y = 1.8089x^{0.3137}$$
$$\text{DM4: } y = 4.7331x^{0.6893}$$

The above power law equations are obtained based on the data normalization – H/H_R and v_G/D with H and v_G as the lateral force and ground displacement respectively; and H_R and D (0.762 m) as the reference lateral force value and monopile diameter respectively. For CM9 and DM4, reference values of 110.0 kN and 250.0 kN respectively have been used. The displacement at the respective reference values are 0.1163 m (CM9) and 0.0807 m (DM4).

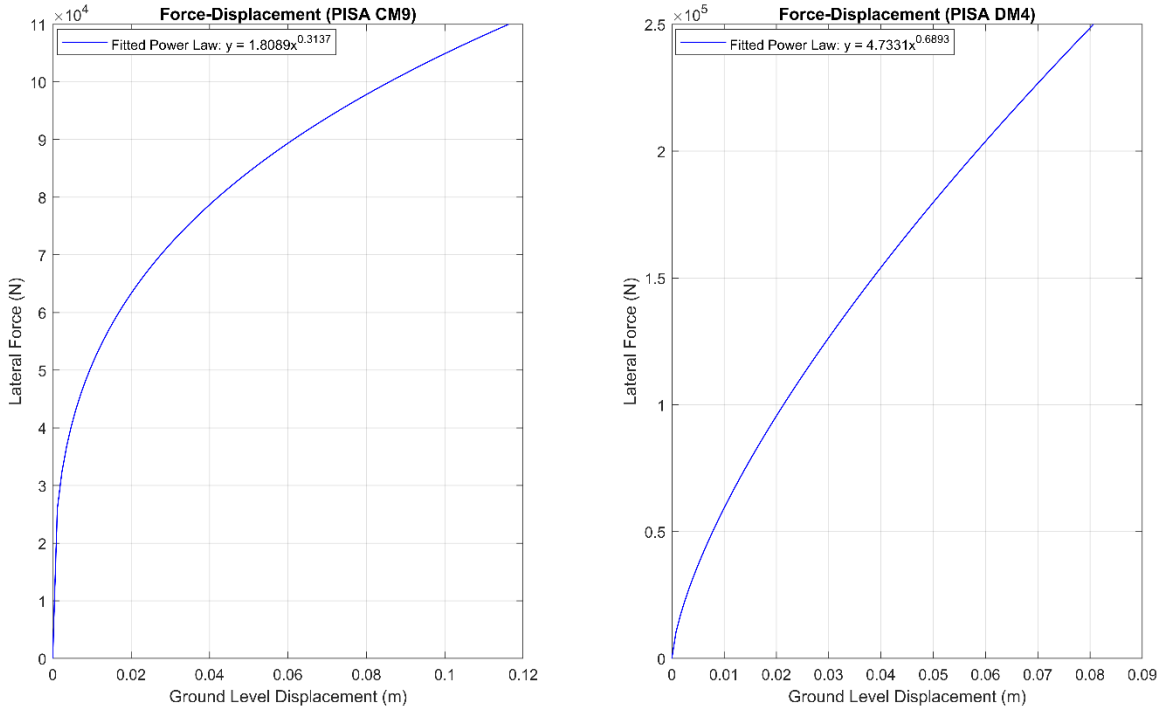

Figure 3. 4. Monotonic Response of PISA CM9 (L/D = 5.20) and DM4 (L/D = 5.25) 3D FE Model.

Table 3. 1. Ratcheting Parameters Adopted for the Study.

Ratcheting Parameter	Value
R_0	1
β_0^r	1×10^{-5}
m_r	0.3
m_s	1

Table 3. 2. Acceleration Scheme for 1-Way Cyclic Loading.

100 Cycles of Cyclic Load			
Cycle-by-Cycle Scheme		**Acceleration Scheme**	
Number of Cycles	R_{fac}	Number of Cycles	R_{fac}
2	1	2	1
7	1	1	7
2	1	2	1
88	1	1	88
1	1	1	1
100 Cycles Computed		7 Cycles Computed	

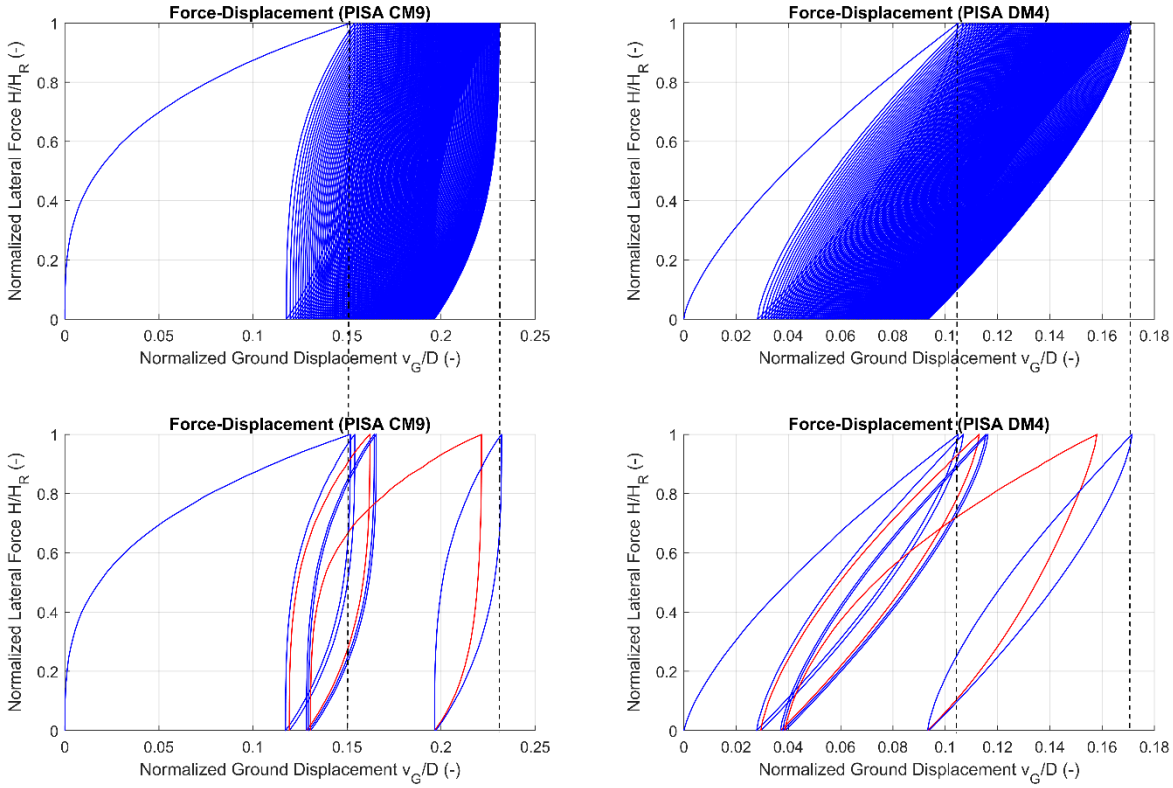

Figure 3. 5. Cyclic Response of HARM Applied to CM9 and DM4.

The response curves in blue and red in Figure 3.5 indicate curves with cycle-by-cycle increments and accelerated increments respectively.

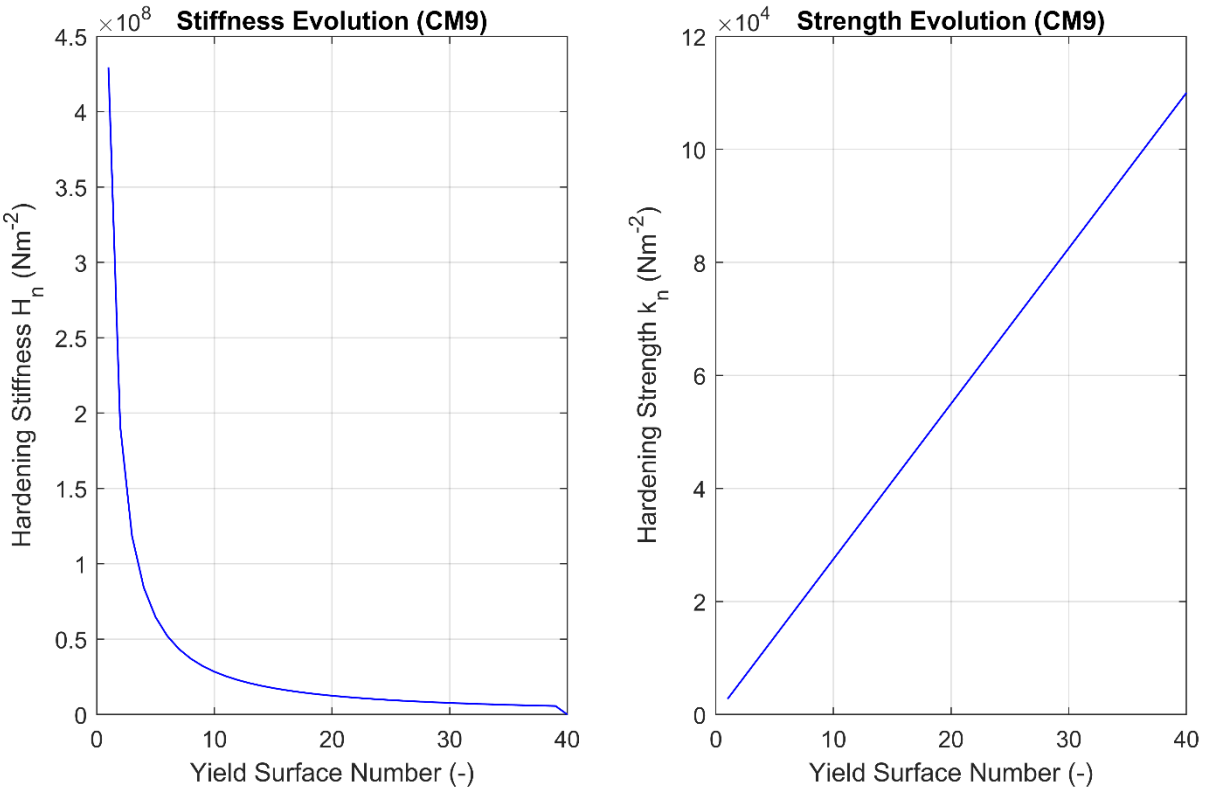

Figure 3. 6. Kinematic Hardening Stiffness (Modulus) and Strength Evolution of CM9 using S-HARM.

3.2 The REDWIN Model

3.2.1 Overview of the REDWIN Macro-Element Model

The REDWIN macro-element model, developed by Page et al. (2019a), is an advanced computational tool designed for simulating the behavior of monopile foundations supporting OWTs. This model is particularly notable for its ability to capture the complex SSI under various loading conditions, including multidirectional cyclic loads, which are common in offshore environments. The aim is to reduce costs in the design of OWTs by developing soil-foundation models that account for key geotechnical issues such as stiffness, damping, drainage, degradation, and long-term behavior, and integrate them into the OWT structural model for more optimal analysis and design.

The REDWIN model has 3 versions namely REDWIN models 1, 2, and 3. Model 1 is the simplest version of the REDWIN model, which is a 1D Winkler-type model with springs arranged in parallel, and mostly suitable for unidirectional loading, say, horizontal loading in one direction. Models 2 and 3 are for multidirectional loading with model 2 accounting for coupled loading in the x-y plane, while model 3 extends this further with additional coupling in the vertical direction. In this study, the focus is on model 2, hence, all references to the REDWIN model are for model 2.

Though the REDWIN in its natural form is displacement-controlled, the KH arrangement is in series. A limitation of the REDWIN code is that it is coupled in the x-y directions, but uncoupled in the *z* direction. It assumes the *z* direction, doesn't contribute significantly to the lateral response of the monopile foundation. This will be a hindrance to applying the model to a foundation with significant contributions in all directions (vertical and horizontal planes), say, anchor piles for instance, or even response to earthquake loading with significant contributions from vertical and horizontal components of the load. Rectifying this will require that the model be reformulated such that it is coupled in all x, y, and

z directions. But for this study, the focus will be on the x-y coupling and then validation with foundation types that resist mostly horizontal load compared to the vertical load.

Foundation Stiffness and Damping

The primary function of the REDWIN model is to accurately represent the foundation stiffness and damping characteristics in integrated time-domain simulations. These simulations are critical for the design and analysis of OWTs, as the foundation behavior significantly impacts the overall dynamic response of the turbine structure, including its natural frequencies and damping properties. Traditional models often simplify the loading conditions by assuming in-plane loads, but the REDWIN model addresses the more realistic scenario of multidirectional loading, thereby providing a more accurate representation of the SSI.

Constitutive Soil Model

A key feature of the REDWIN constitutive model is its capability in simulating 3D stress conditions in cohesive soils under undrained conditions, as well as non-cohesive soils. This model adopts a MSKH approach, which is advantageous for its ability to produce closed loops in cyclic loading scenarios, reflecting the expected behavior under operational load conditions having relatively low cyclic load levels with respect to the pile capacity coupled with the number of cycles expected within a short simulation timeframe of 10–60 minutes in an integrated analysis (Page et al., 2019a). The multi-surface plasticity model utilized in REDWIN is characterized by KH, where the yield surfaces translate in stress space without changing size, a method that effectively captures the cyclic stress-strain behavior of the foundation.

Multidirectional Loading

The REDWIN model also stands out for its capability to simulate the impact of multidirectional cyclic loads on monopiles supported on OWT. Offshore environments subject monopiles to complex loading conditions, with waves and wind often acting in different directions. The model incorporates these multidirectional effects, thereby providing a more comprehensive understanding of the monopile response. This feature is crucial for ensuring the structural integrity and longevity of OWTs, as it affects the foundation stiffness and hysteretic damping, which in turn influence the fatigue damage and the designed structural fatigue lifetime of the structure (Page et al., 2019a).

Implementation and Verification

The implementation of the model as user-defined in commercial FE software, such as PLAXIS 3D, has been verified against detailed FEA as well as comparison against true triaxial tests. The results have shown that the model can simulate the monopile response with high accuracy while significantly reducing computational effort compared to traditional FEA approaches. This efficiency makes the REDWIN model a valuable tool for integrated analysis and design processes, enabling engineers to perform extensive simulations within practical time frames.

Applications

In practical terms, the model is used in the design phase of OWT projects to predict the performance of monopile foundations under realistic loading scenarios. By incorporating the effects of multidirectional cyclic loads, engineers can better anticipate potential issues related to foundation stiffness and damping, leading to more robust and reliable turbine designs. The ability of the model to reduce computational effort without compromising accuracy also allows for more extensive parametric studies, facilitating optimized foundation designs that meet both performance and economic criteria.

3.2.2 Sign Convention and Coordinate Orientation

In OWTs, the in-plane loading is that which acts in the direction tangential to the plane of rotation along the y-axis, and the out-of-plane loading is that which acts in the direction normal to the plane of rotation along the x-axis. The positive sense of all forces acting on the monopile foundation is depicted in Figure 3.7.

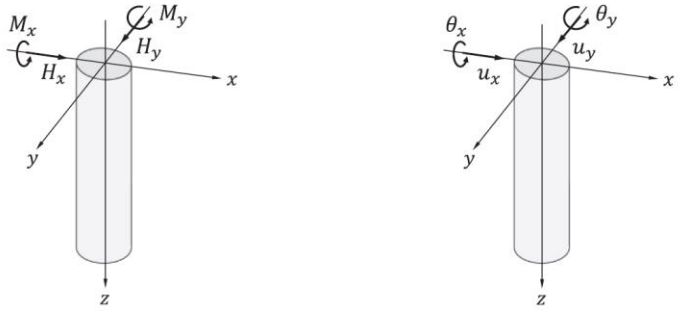

(a) Force components. (b) Displacements components.

Figure 3. 7. Positive Sense of Lateral Force and Displacement (Butterfield et al., 1997).

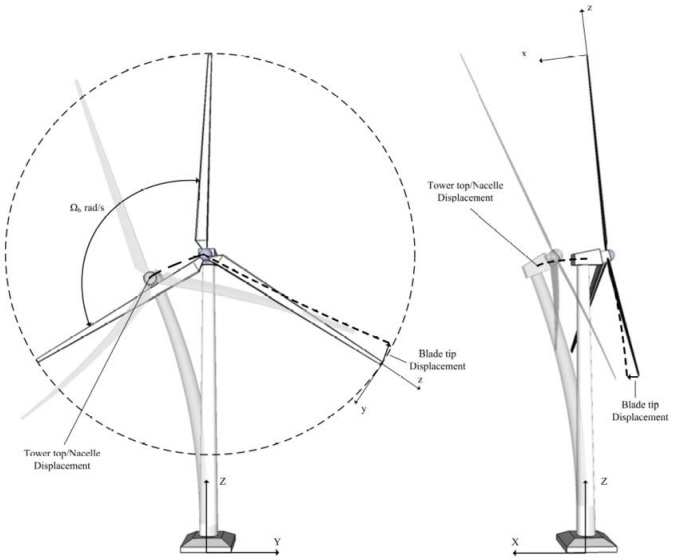

Figure 3. 8. In-Plane & Out-of-Plane Loading Orientation (Fitzgerald & Basu, 2020).

3.2.3 Literature Review on REDWIN

REDWIN Model and Its Development

Page et al. (2017) presented a foundation model for integrated analysis of OWTs with improved load predictions. The model which is based on FEA is simple and computationally efficient with the aim to improve reliability and accuracy. The model performance is demonstrated on real OWT time histories and replicates nonlinear load-displacement response and hysteretic behavior. Model calibration is informed by FEA, with simplification of the load-displacement relation and improved foundation modeling accuracy. The model calibration is very flexible and can be calibrated to varying soil conditions. The model enhanced load predictions and reduced the design uncertainties due to fatigue over the lifetime. Foundation stiffness during unloading and reloading can be reproduced as well as the damping as a function of the loading history.

Page et al. (2018) presented a macro-element model for piles using a multi-surface plasticity framework. The model design follows classical elastoplastic theory with active yield surfaces, thus leading to a new foundation model for monopile-based OWTs with accurate nonlinear load-displacement response in integrated load simulations. The analyses were based on unidirectional loading. The calibration of the model is informed by 3D FEA pushover analysis. Comparisons were made against field test measurements and FEA results.

Existing models fail to reproduce natural frequencies accurately, for instance, the traditional API p-y curves underestimate soil response and lack foundation damping. The paper contributed to a new macro-element model for cyclic undrained loading of piles and predicts load-displacement response and hysteretic damping in integrated analyses.

Here the pile response and the surrounding soil have been condensed into a force-displacement relation at the seabed. The practical implication is in the aspect of reduction in computational effort while maintaining accuracy in foundation response simulations, and the model applies to offshore structures and bridges for lateral loading predictions. The foundation model can integrate vertical, torsional, and lateral loading responses effectively. Demonstration is made on the application of the model to simulate the dynamic response of the wind turbine under various environmental conditions – wind and wave loads, and the SSI influence. There is a lack of vertical load effect on lateral response in the model; frequency dependency is not considered in the model formulation, while assumptions limit model applicability to specific soil conditions as further validation is needed to confirm the applicability of the model to a wide range of soil conditions.

Advancements in Model Calibration and Multidirectional Loading

Page et al. (2019a) investigated and extended the foundation model to multidirectional loading of a monopile in clay supporting OWTs. The numerical simulations are based on yield criteria for time-domain integrated structural design. The von Mises yield criterion used in the unidirectional analysis has been extended to a criterion based on the 4D elliptical yield function in the multidirectional analysis. The proposed macro-element model results in reduced computational effort and the constitutive soil model is validated for integrated analyses of OWTs. Results indicated that multidirectional loading alters foundation stiffness and damping thus, affecting OWT eigenfrequencies and damping characteristics. This is a very important finding as it has significant consequences on the designed structural fatigue over the lifetime. The calibration of the model is informed by FEA, and the macro-element model is verified against FEA for accuracy. The calibration is simple, flexible, and computationally efficient. The paper's contribution to the field of studies is the presentation of a model that can accurately represent both foundation stiffness and foundation damping efficiently, as the existing models focused on the provision of either an accurate foundation stiffness or foundation damping.

Skau et al. (2018a) studied the monopile fatigue damage influenced by different foundation models under the REDWIN project. The REDWIN project integrates geotechnical discipline in OWT design. The main aim is to develop foundation models for dynamic time-domain integrated analyses with improved accuracy and provide application-oriented models with flexibility for different foundation types. The foundation behavior was shown to have a significant impact on fatigue damage in monopile design. A library was developed for the representation of the most common types of foundations, and are grouped into 3 model categories named – REDWIN model 1, 2, and 3. As described earlier, in terms of load regime, model 1 is 1D with distributed load applied to any degrees of freedom (DOFs), model 2 is based on lateral force & moment loads, and model 3 is based on the vertical force, lateral force & moment loads.

Applications and Validation of the REDWIN Model

Page et al. (2019b) presented a library based on the REWIN plasticity model verified against large-scale field experiment data for validation. The model is still within the macro-element model framework for arbitrary coupled loads at the seabed for monopiles with nonlinear lateral response and elastic loading. The paper presented a macro-element model for dynamic response simulations based on coupled aero-servo-hydro-elastic analysis, with good balance in computational accuracy and efficiency, and decreased uncertainty in load predictions and fatigue life estimates. Findings from the paper indicated that the model reproduced nonlinear load-displacement response observed in large-scale field tests; accurate reproduction of the natural frequencies which is a limitation in existing models; and foundation damping as a function of displacement amplitude is produced. The models account for multidirectional loading effects on load-displacement response. In addition, the calibration is simple, flexible, and computationally efficient with physical interpretation.

Bergua et al. (2021a) presented a comprehensive study and summary of the activities of the OC6 Phase II project in terms of improvement in offshore wind design with an advanced SSI model. The introduction of the macro-element approach improved the accuracy of foundation characteristics, reduced uncertainty, and enhanced the cost-effectiveness of the offshore wind design. The SSI model is retrieved from the REDWIN project and uses elastoplastic with KH based on the macro-element model. This model captured the stiffness and damping characteristics more accurately compared to the traditional and simplified SSI models like models based on distributed springs, coupled springs, and apparent fixity. The contribution of the paper is on the integration of the REDWIN SSI model into offshore wind system design, and the

verification of new capability in OC6 Phase II project based on the SSI model. Traditional SSI models are compared to the REDWIN model for load assessment. The linear SSI approaches showed smaller tower-top displacements in simulations. The macro-element model reduces system loading, thus, improving design efficiency – attributed to the effects of both shifts in natural frequencies of the system and increased energy dissipation. This suggests a more cost-effective design that is less conservative.

Bergua et al. (2021b) provided a detailed overview of the work done within the OC6 Phase II project and presented the REDWIN macro-element model for fixed-bottom OWT foundations with a detailed discussion focused on SSI, damping, and different load cases based on monopiles examined under the WAS-XL (wave loads and soil support for extra-large monopiles) project leading to reduction in the uncertainties in large-diameter monopile design for offshore wind systems. Part of the findings showed that the REDWIN macro-element model dissipates energy, while the elastic stiffness matrix approach does not dissipate energy when a free-decay test was performed to quantify the SSI damping. Also, the load-deflection curves showed system response and energy dissipation.

Case Studies and Future Research Directions

Skau et al. (2018b) presented a macro-element model for bucket foundations in OWTs and discussed load reference points and foundation characteristics in seabed analysis. The model is developed in a multi-surface plasticity framework for cyclic loading behavior and is intended for an application-oriented engineering design model with physically understandable input data. The model can reproduce FE soil and foundation responses accurately, and capture shallow foundation in clay behavior under irregular cyclic loading. The positive aspect of the model is that it's numerically stable, ratcheting is avoided, and it matches large-scale field test results. The plastic work evolved non-proportionally along load axes, changing flow direction. The limitation of the model is the exclusion of displacement accumulation (ratcheting) and stiffness degradation due to load cycles. Though the formulation prevented numerical ratcheting, numerical stability is ensured as earlier noted. There's good agreement in the overall response, but a slight underestimation of damping, and the model neglects high-frequency loading effects like inertia and radiation damping.

Van Hoogstraten et al. (2020) explored the prevalent and impact of extreme loads from typhoons on the support structure design of OWTs in Asia-Pacific; assessed the improvement of the nonlinear macro-element model based on nonlinear hysteretic response (hysteretic foundation damping) on the support structure response in dynamic analysis simulations due to extreme load levels, which indicates that nonlinear macro-element model reduced response magnitude on the support structures compared to foundation models that are based on nonlinear elasticity with calibration informed by API p-y functions. The model agreed well with 3D FEA but was slightly softer; provided good damping estimation and captured SSI accurately under extreme loads. Macro-element model calibration is informed by 3D FEA.

Practical implications are that the macro-element model enhanced OWT support structure response accuracy; the use of logarithmic decrement method (LDM) with caution for system damping estimation as it may not be valid for OWTs with nonlinearities in extreme loads. Additional steady-state forced vibrations are recommended for storm conditions analysis. There is a need to evaluate damping using energy balance for global damping ratio estimation. Limitations of the model are that the LDM approach is not accurate for nonlinear stiffness and damping; also, gapping is not considered in the macro-element model, hence, this affects the unloading-reloading.

Klinkvort et al. (2020) presented a fast monopile design for OWTs using the NGI approach with a time-efficient 3D FEA program for cyclic loading and spring calibration, with a focus on cyclic loads, soil response, and monopile optimization. The contribution of the paper is the proposal of a simpler design approach based on NGI cyclic accumulation. Practical implications of the study are in the Python script automation of geotechnical monopile design for an entire wind farm and spring calibration; utilization of fast 3D FEA tool for accurate calculations of permanent rotation at the end-of-life of the monopile i.e. SLS, determination of the pile capacity under maximum (extreme) loads i.e. ULS and the pile response under operational condition i.e. FLS. Findings indicate that the model has a simplified design method for monopiles compared to advanced methods; the Python script is implemented in three stages for 3 different limit states – SLS, ULS, and FLS; and the optimal monopile geometry is determined through cyclic accumulation and stress redistribution.

3.2.4 REDWIN Formulation for Multidirectional Loading

REDWIN formulation under multidirectional loads based on MSKH framework according to the work of Page et al. (2019a) is presented here. The unidirectional formulation of the REDWIN model as per Page et al. (2018) which is a precursor to the multidirectional formulation presented here is very vital for model calibration based on the input load-displacement curves and the foundation's stiffness matrix. This has been presented under Appendix D. Given a stress state characterized by the stress tensor σ and the corresponding strain tensor ϵ, thus the incremental constitutive response can be established for small increments $d\sigma$ and $d\epsilon$.

(1) Yield Surface: A typical representation of von Mises yield criterion in 3D space is given below.

$$f_i(\sigma, \alpha_i) = \sqrt{3.J_2(\sigma, \alpha_i)} - r_i = 0$$

Where J_2 deviatoric stress tensor's second invariant which is a function of the deviatoric stress tensor σ and the back-stress α_i which defines the center of the yield surface, whereas the von Mises yield criterion can be visualized as a circle in the π-plane with r_i representing the radius of each of the circles starting with the inner-most circle with the radius r_1 which distinguishes the elastic region from the elastoplastic region. It is to be noted that in the π-plane which is a 2D representation of the deviatoric plane, the von Mises yield surface appears as a circle, but appears as an ellipse/ellipsoid in the full deviatoric plane (3D).

For the multidirectional formulation in 4 DOFs i.e. in the horizontal x-y plane only (vertical plane excluded), yield criterion based on hypersphere or 4D spherical function is utilized.

$$f_i(\sigma, \alpha_i) = \sqrt{\sum_{k=1}^{4} \left(\sigma_k - \alpha_{i,k}\right)^2} - r_i = 0$$

Where σ_k is the principal stress in the transformed 4D space (hyperspherical space), $\alpha_{i,k}$ is the component of the back-stress vector α_i in the 4D space and r_i is the radius of the i-th yield surface in the hyperspherical space.

(2) Generalized Load and Displacement Vectors
Here, implementation in 4-DOFs is presented. The generalized force vector σ and work-conjugate generalized displacement vector ϵ is given as;

$$\sigma = \begin{bmatrix} H_y \\ H_x \\ M_y/D \\ M_x/D \end{bmatrix}; \qquad \epsilon = \begin{bmatrix} u_y \\ u_x \\ D.\theta_y \\ D.\theta_x \end{bmatrix}$$

Where D is the pile diameter. For simplicity, the generalized vector notations are not bolded.
(3) Plastic Work-done: The plastic work-done W^p is calculated as;

$$W^p = \int_0^{u_y^p} H_y.du_y^p + \int_0^{u_x^p} H_x.du_x^p + \int_0^{\theta_y^p} M_y.d\theta_y^p + \int_0^{\theta_x^p} M_x.d\theta_x^p$$

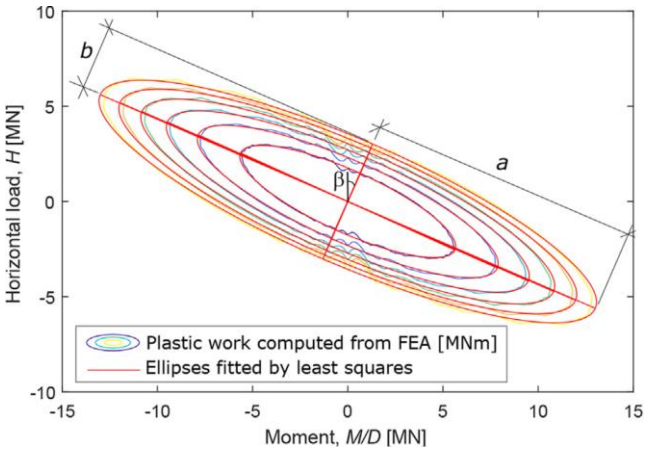

Figure 3. 9. Constant Plastic Work Contours (Page et al., 2018).

(4) Incremental Contributions: The macro-element formulation constitutive model is based on MSKH. Given the generalized displacement increment as $d\epsilon$ decomposed into elastic and plastic components, then the incremental contributions from elastic and plastic displacements are;

$$d\epsilon = d\epsilon^e + d\epsilon^p$$

Where ϵ^e and ϵ^p are the generalized elastic and plastic displacement respectively.
(5) Elastic Response: Likewise, the incremental elastic response in 4-DOFs is given as;

$$d\sigma = \boldsymbol{K}.d\epsilon^e; \qquad \boldsymbol{K} = \begin{bmatrix} K_{11} & K_{12} & K_{13} & K_{14} \\ K_{21} & K_{22} & K_{23} & K_{24} \\ K_{31} & K_{32} & K_{33} & K_{34} \\ K_{41} & K_{42} & K_{43} & K_{44} \end{bmatrix}$$

Where $\boldsymbol{K}$ is the elastic stiffness matrix. Note that $\boldsymbol{K}$ is dependent on the dimension of the pile, properties of the pile, layering of soil, properties of soil, and drainage conditions.
(6) Yield Criterion: The yield criterion f is given as;

$$f(\sigma, \alpha) = f(H_y, H_x, M_y/D, M_x/D, \alpha_{H_y}, \alpha_{H_x}, \alpha_{M_y}, \alpha_{M_x})$$

Given an arbitrary number of yield surface i;

$$f_i(\sigma, \alpha_i) = \alpha_{1,i}.\left(H_x - \alpha_{H_x,i}\right)^2 + \alpha_{1,i}.\left(H_y - \alpha_{H_y,i}\right)^2 + \alpha_{2,i}.\left(M_y/D - \alpha_{M_y,i}\right)^2 + \alpha_{2,i}.\left(M_x/D - \alpha_{H_x,i}\right)^2$$
$$+ 2.\alpha_{3,i}.\left(H_x - \alpha_{H_x,i}\right).\left(\frac{M_y}{D} - \alpha_{M_y,i}\right) - \alpha_{3,i}.\left(H_y - \alpha_{H_y,i}\right).\left(M_x/D - \alpha_{H_x,i}\right) - 1 = 0$$

Where α_i is the position or coordinate of the back-stress vector at a given yield surface i. This is also referred to as generalized state variables. Also, $\alpha_{1,i}$, $\alpha_{2,i}$ and $\alpha_{3,i}$ indicates the shape/size and orientation of the yield surface i. The shape s indicated as ratio of the elliptical axes of the plastic work-done contours are approximately constant, thus, s and orientation β for all the yield surfaces are assumed constant, hence, homothetic yield surfaces. This function defines an elliptical yield surface in a 4D space of generalized stresses.

(7) Flow Rule: Flow rule definition,

$$d\epsilon^p = d\lambda.\frac{\partial \mathrm{g}}{\partial \sigma}$$

Here g in the flow rule formulation is the plastic potential surface. The flow rule equation becomes associative when g is equal to the yield surface f.
For each yield surface i;

$$d\epsilon_i^p = d\lambda_i.\frac{\partial f_i}{\partial \sigma}$$

Where $d\lambda_i$ represents the plastic multiplier and $d\epsilon^p$ represents the total plastic strain. Assuming Koiter's rule (Koiter, 1953) applied to the sum of plastic contributions from active yield surfaces gives;

$$d\epsilon^p = \sum_{i=1}^{j} d\epsilon_i^p = \sum_{i=1}^{j} d\lambda_i . \frac{\partial f_i}{\partial \sigma}$$

Where j indicates the number of active yield surfaces.

(8) Hardening Rule: Ziegler's KH rule,

$$d\alpha_i = d\mu_i . (\sigma - \alpha_i)$$

Where μ_i is a function of λ_i.

The hardening rule is reformulated as follows;

$$d\alpha_i = \boldsymbol{K}_i^p . d\epsilon^p = d\lambda_i . \boldsymbol{K}_i^p . \frac{\partial f_i}{\partial \sigma}$$

Note that the plastic stiffness matrix $\boldsymbol{K}_i^p$ is interpreted as;

$$\boldsymbol{K}_i^p = \frac{\sigma - \alpha_i}{d\epsilon^p}$$

This value is constant for each yield surface i, hence resulting in linear piece-wise KH curves.

The plastic stiffness matrix $\boldsymbol{K}_i^p$ in 6-DOFs is given as;

$$\boldsymbol{K}_i^p = \begin{bmatrix} \frac{4}{3}G_i^p & -\frac{2}{3}G_i^p & -\frac{2}{3}G_i^p & 0 & 0 & 0 \\ -\frac{2}{3}G_i^p & \frac{4}{3}G_i^p & -\frac{2}{3}G_i^p & 0 & 0 & 0 \\ -\frac{2}{3}G_i^p & -\frac{2}{3}G_i^p & \frac{4}{3}G_i^p & 0 & 0 & 0 \\ 0 & 0 & 0 & G_i^p & 0 & 0 \\ 0 & 0 & 0 & 0 & G_i^p & 0 \\ 0 & 0 & 0 & 0 & 0 & G_i^p \end{bmatrix}$$

Where G_i^p is the plastic shear modulus corresponding to each of the yield surfaces. In 1D Iwan (Iwan, 1967) KH model, it represents the stiffness for each of the spring-slider units. This plastic stiffness matrix is a representation of $\sigma - \alpha_i$ to $d\epsilon^p$ ratio, and remains constant for all the yield surfaces i. Thus, the hardening curves are piecewise linear. In 4-DOFs, elimination of the 3rd and 6th rows and columns is required. This removes the vertical component.

(9) Consistency Condition: The consistency condition assuming a single yield surface is given as;

$$df = \left(\frac{\partial f}{\partial \sigma}\right)^T . d\sigma + \frac{\partial f}{\partial \alpha} . \frac{\partial \alpha}{\partial \lambda} d\lambda = 0$$

$$df = \left(\frac{\partial f}{\partial \sigma}\right)^T . d\sigma + (-A d\lambda) = 0$$

Where A represents the plastic resistance. The above equation can be re-written as follows;

$$A . d\lambda = \left(\frac{\partial f}{\partial \sigma}\right)^T . d\sigma \approx f; \qquad f \approx A . d\lambda$$

For an arbitrary number of active yield surface(s) j, the consistency condition can be represented as;

$$f = \begin{bmatrix} f_1 \\ f_2 \\ \vdots \\ f_j \end{bmatrix} \approx \begin{bmatrix} a_{11} + A_1 & a_{12} & \cdots & a_{1j} \\ a_{21} & a_{22} + A_2 & \cdots & a_{2j} \\ \vdots & \vdots & \ddots & \vdots \\ a_{j1} & a_{j2} & \cdots & a_{jj} + A_j \end{bmatrix} = \Xi . d\lambda$$

Where;

$$a_{ik} = \left(\frac{\partial f_i}{\partial \sigma}\right)^T . \boldsymbol{K} . \left(\frac{\partial f_k}{\partial \sigma}\right)$$

And;

$$A_k = \left(\frac{\partial f_k}{\partial \sigma}\right)^T . \boldsymbol{K}_k^p . \left(\frac{\partial f_k}{\partial \sigma}\right)$$

This is required to obtain $d\lambda_i$ for each yield surface, given j active yield surface(s). The above symbol Ξ which is a matrix with several components, can be simplified as:

$$\Xi_{ik} = a_{ik} + A_k$$

$$\Xi_{ik} = \left(\frac{\partial f_i}{\partial \sigma}\right)^T . \boldsymbol{K} . \left(\frac{\partial f_k}{\partial \sigma}\right) + \left(\frac{\partial f_k}{\partial \sigma}\right)^T . \boldsymbol{K}_k^p . \left(\frac{\partial f_k}{\partial \sigma}\right)$$

Given incremental steps from n to $n+1$, this ensures that the yield criterion $f_{i,n+1} = 0$ is satisfied at the end of each step. This is a critical aspect of elastoplasticity models to ensure that the material's behavior adheres to the defined yield surface. Consistency conditions ensure convergence by checking the yield criteria and updating plastic multipliers iteratively.

(10) Step-by-Step Numerical Implementation Procedure: Presented here is the numerical implementation of the macro-element model in incremental response. For every iteration or incremental step completed, i.e. from step n to $n+1$ then $\Delta\epsilon$ which is the incremental generalized displacement is applied to the foundation model. In return, the generalized force i.e. σ_{n+1} is computed and likewise, the state variable is updated which in this case is the back-stress i.e. $\alpha_{i,n+1}$ for each yield surface i.

The first step is to compute the trial stress σ_{n+1}^{trial};

$$\sigma_{n+1}^{trial} = \sigma_n + \boldsymbol{K} . \Delta\epsilon$$

Then the trial back-stress $\alpha_{i,n+1}^{trial}$;

$$\alpha_{i,n+1}^{trial} = \alpha_{i,n}$$

Check to determine if the yield surface i is active for the trial stress and trial back-stress;

$$f_{i,n+1} \geq 0$$

If active then the yield criterion $f_{i,n+1} = 0$ has to be satisfied at the end of the step. With the inclusion of the associative flow rule, and separation of the strain into elastic and plastic components, then the updated stress state σ_{n+1} following Koiter's rule can be computed as follows;

$$\sigma_{n+1} = \sigma_{n+1}^{trial} - \boldsymbol{K} . \sum_{j=1}^{i} \Delta\lambda_j . \left\{\frac{\partial f_j}{\partial \sigma}\right\}_{n+1}$$

Where i here is the number of active yield surface(s). The assumption here is that once a yield surface j is active, then all surface(s) enclosed by it would be active i.e. starting from the inner-most surface with $j = 1$ up to j which is the active outer-most yield surface. Otherwise, yield surfaces beyond j i.e. say, $j+1$ onwards are considered inactive. From the KH rule, $\alpha_{i,n+1}$ (back-stress update) is computed as follows;

$$\alpha_{i,n+1} = \alpha_{i,n+1}^{trial} + \Delta\lambda_i . \boldsymbol{K}_i^p . \left\{\frac{\partial f_i}{\partial \sigma}\right\}_{n+1}$$

Or;

$$\alpha_{i,n+1} = \alpha_{i,n} + \Delta\lambda_i . \boldsymbol{K}_i^p . \left\{\frac{\partial f_i}{\partial \sigma}\right\}_{n+1}$$

The plastic multiplier is computed iteratively until the required condition is satisfied as follows;

$$\sum_{j=1}^{i} |f_{j,n+1}| < tol . s_u$$

Where i again is the number of active yield surface(s); specified tolerance is tol, say, 10^{-5} and then s_u represents the undrained shear strength of the soil (applicable to cohesive soil like clay). For each iteration, the vector $\Delta\lambda$ with elements $\Delta\lambda_i$ is updated with the addition $\delta\Delta\lambda$ computed as follows;

$$\delta\Delta\lambda = \Xi_{n+1}^{-1} . f_{n+1}$$

Where f_{n+1} is a vector with elements $f_{j,n+1}$. Once convergence is not achieved after a specified number of iterations, then sub-stepping is enforced. Once sub-stepping is activated, the earlier incremental strain $\Delta\epsilon$ input is divided by 10, thus, the computation process is repeated.

Geometric Transformation

Similar to the 2-DOFs model where the ellipse (2D) is transformed into circles (2D), here in the case of the 4-DOFs model, the yield surfaces in 4D ellipsoidal shapes are transformed into 4D spherical shapes. This is done to enable efficiency and robustness in the implementation of the macro-element model. Hence, the yield criterion is formulated in the spherical coordinate system, with the adoption of a stress invariant.

$$\sigma' = R.\sigma = \begin{bmatrix} sin\beta & 0 & 0 & cos\beta \\ 0 & -sin\beta & cos\beta & 0 \\ 0 & -s.cos\beta & -s.sin\beta & 0 \\ -s.cos\beta & 0 & 0 & s.sin\beta \end{bmatrix}.\sigma$$

In the above formulation, the transformed generalized force is σ' and R is the linear transformation matrix. Also, s describes the deformation of the ellipsoidal surface into a spherical surface, and β indicates the rotation or its orientation. Again, just like in the case of the 2-DOFs model, the above transformation and computations are only valid provided that the yield surfaces are homothetic or geometrically similar to each other.

$$\beta = \frac{\pi}{2} + \frac{1}{2}.\arctan\left(\frac{2.\frac{a_1}{a_3}}{\frac{a_1}{a_3}.\frac{a_2}{a_3} - 1}\right)$$

$$s = \sqrt{\frac{\frac{a_1}{a_3}.\frac{a_2}{a_3} + 1 - \sqrt{\left(\frac{a_1}{a_3}.\frac{a_2}{a_3} - 1\right).\left(\frac{a_1}{a_3}.\frac{a_2}{a_3} - 1 + 4.\left(\frac{a_1}{a_3}.\frac{a_2}{a_3}\right)\right)}}{\frac{a_1}{a_3}.\frac{a_2}{a_3} + 1 + \sqrt{\left(\frac{a_1}{a_3}.\frac{a_2}{a_3} - 1\right).\left(\frac{a_1}{a_3}.\frac{a_2}{a_3} - 1 + 4.\left(\frac{a_1}{a_3}.\frac{a_2}{a_3}\right)\right)}}}$$

Where a_1/a_3 and a_2/a_3 are ellipsoid parameters. The incremental generalized displacement $\Delta\epsilon$ is transformed via the inverse of the transpose of the transformation matrix. Thus, the transformed incremental generalized displacement $\Delta\epsilon'$ is given as;

$$\Delta\epsilon' = (R^T)^{-1}.\Delta\epsilon$$

As soon as both $\Delta\epsilon$ and σ_n are in the transformed coordinate system via the use of R and $(R^T)^{-1}$, then the incremental constitutive response is solved in the transformed coordinate system (spherical system), and thus the updated generalized forces are transformed to the ellipsoidal coordinate system. Note that the plastic work done remains constant (does not change) irrespective of changes in coordinate systems.

Model Calibration

The calibration approach in the 2-DOFs model is the same as in the 4-DOFs model. This process only required two things to be specified – the elastic stiffness matrix coefficients and the nonlinear load-displacement curves (backbone curves). This load-displacement curve for the relevant representative soil model can be obtained from experimental or field tests like the PISA project and also numerically from a static pushover analysis in the FEA program.

In summary, following the specification of the required calibration data (coefficients of elastic stiffness matrix and backbone curves), the plastic displacement components are obtained, then s and β hardening parameters are determined from the force-plastic displacement relations.

The force-plastic displacement relations are transformed into a spherical coordinate system, and the calibration parameters – stiffness K_i^T and strength or radius S_i are obtained. With the assumption of spring-slider units coupling in series, then K_i^p based on pure Iwan (1967) kinematic hardening formulation is obtained as follows;

$$K_i^p = \left(\frac{1}{K_i^T} - \sum_{j=1}^{i-1}\frac{1}{K_j^p}\right)^{-1}$$

$$\boldsymbol{K}_i^p = K_i^p . \boldsymbol{I}$$

The REDWIN formulation presents a comprehensive model to predict the elastoplastic behavior of the monopile foundation under multidirectional loading using a 4D hypersphere-based yield criterion. The iterative solution procedure ensures that the consistency condition is maintained, which allows for accurate constitutive relation predictions across complex loading paths.

Radiation damping is ignored (OWT foundations are of very low frequency), but hysteresis (damping) is accounted for. Ratcheting is ignored as load intensity is assumed relatively low.

3.3 Other Notable Plasticity Models

Notably, two of the most common plasticity frameworks in the literature for offshore foundation constitutive modelling are frameworks based on the hyperplasticity model and the hypoplastic model. While the Hyperplasticity approach to plasticity theory is based on thermodynamic principles where the entire material response is derived from knowledge of two potential functions of which HARM is an example of a model that falls under this framework; the hypoplastic models are an alternative approach for modeling mechanical behaviors of soils as they describe anelastic phenomena without the need for additional concepts such as yield surfaces, plastic potentials, and strain decomposition.

Both multi-surface plasticity model and bounding surface plasticity model can be formulated under the hyperplasticity framework. The HARM model and REDWIN models are implemented using the multi-surface plasticity model. An example of a constitutive model implemented under the bounding surface plasticity is the SANISAND model. This model is particularly suitable for reproducing the drained mechanical response of sands in high-cyclic loading conditions, and it is part of a family of simple anisotropic sand constitutive models developed within the framework of critical state soil mechanics and bounding surface plasticity. The critical state concept determines the behavior of soil under various loading conditions i.e. void ratios and effective stresses.

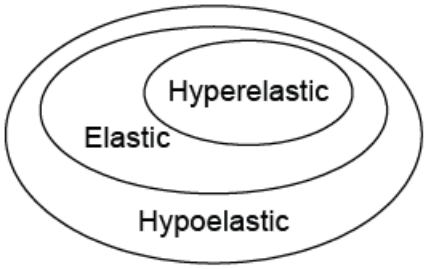

Figure 3. 10. Classical Theory on Plasticity (Houlsby & Puzrin, 2006).

3.3.1 State-of-the-Art Review on the Plasticity Models

Several constitutive models have been developed to simulate the SSI in offshore environments. These models include sophisticated nonlinear and plasticity-based models that capture the intricate behaviors of monopile foundations under varying loading conditions. Recent advancements in the field have focused on addressing the limitations of traditional models, such as their inability to accurately predict accumulated deformation due to ratcheting under cyclic loading and their limited applicability under complex, multidirectional loading conditions.

The literature review in this section examines the state-of-the-art constitutive models used for simulating the behavior of monopile foundations in the offshore domain. The review highlights the key advancements of OWT supported on monopile foundation under cyclic loading and their implementation and identifies the limitations and gaps that still exist in this domain.

Experimental Modelling of Cyclic Loading

Abadie et al. (2018) performed experimental work on monopile behavior in cohesionless soil under cyclic lateral loading, identifying key mechanisms, ratcheting behavior, and response to complex loads – with results indicating conformity to Masing rules (and extended Masing rules), with permanent accumulated deformation (ratcheting) during cyclic loads due to non-symmetric nature of the loads. Methods deployed are the use of 1 g laboratory model tests scaled for OWT monopiles; investigation of loading rate effects, hysteretic behavior, long-term cyclic loading; and multi-amplitude cyclic loads to analyze complex load scenarios. The paper provided some insights for developing new constitutive models for accurate monopile response predictions. The ratcheting behavior is characterized by a decreasing rate with cycle number, influenced by cyclic load magnitude; the hysteresis loop tightens with increased secant stiffness and decreased area of the loop.

Richards et al. (2020) explored experimentally monopile rotation under various cyclic lateral loading scenarios (constant and variable amplitude, unidirectional and multidirectional) in dry sand for wind turbine design. The authors aimed to investigate monopile response to multidirectional and multi-amplitude cyclic loading; and understand monopile rotation evolution under many cycles. The tests showed rotation response to unidirectional and multidirectional cyclic loading. Rotation accumulation under cyclic loading is a key concern. Methods used in the study are laboratory tests in dry sand with constant and variable amplitude loading; unidirectional and multidirectional cyclic loading tests conducted for model development; and multi-amplitude storm tests to highlight realistic loading responses. Practical implications of the study are informed monopile design with rotation response to cyclic loading; provision of insight into multidirectional cyclic loading response; and validation of models with realistic loading features. Results indicate qualitatively similar behavior in very loose and dense sand; unidirectional tests are consistent with previous studies, providing a basis for interpretation of more complex tests; multidirectional tests offer new insights into monopile response to multidirectional cyclic loading; and multi-amplitude storm tests highlight salient features of monopile response to realistic loading. The observed limitation is scaling uncertainties limit direct full-scale design application i.e. caution is needed in scaling laboratory responses for full-scale design. Furthermore, reference values for rotation and displacement vary among researchers.

Richards et al. (2021) explored through modeling techniques the stress level impact on monopile response to cyclic lateral loading in sand. The outcome of the paper indicates that stress level impacts pile displacement and secant stiffness under cyclic loading. Furthermore, full-scale stress levels are essential for a thorough understanding of foundation behavior. Methods used are stress control via centrifuge testing (physical modeling) at varying g levels; and investigation through small-scale physical modeling at 1 g and centrifuge. Results indicated reduced pile displacement i.e. rate of accumulation of pile displacement and secant stiffness i.e. rate of change of secant stiffness with increasing stress levels under the cyclic loading; qualitative similarity in responses across stress levels with some quantitative differences. Qualitative insights from 1 g modeling provide valuable foundation behavior data and can inform new design methods. The study could be extended to assess the effect of stress levels on cyclic response to minimize backbone linearity; and full-scale stress level simulation for a thorough understanding of foundation behavior.

Numerical Modelling of Cyclic Loading: Constitutive Model Development & Application

Luo et al. (2016) investigated offshore monopile response to lateral cyclic loads using the user subroutine of degradation stiffness model (DSM) model for displacement analysis; then the power model and logarithmic model for displacement prediction. Evaluation of the two models for predicting accumulated displacement under various load levels indicated that the logarithmic model underestimates displacements for larger load levels, while the power model showed validity under different load levels with linear parameter increments. Results showed that larger cyclic loads increased monopile displacement with load cycle number in the dense sand ground; the power model is valid under various load levels for displacement prediction – the model parameter α increases linearly with load level increase. The maximum load in each cycle is expected to be less than 0.58 times the static load capacity. Limitations encountered are that the API p-y method is not suitable for cumulative displacement prediction, and the DSM model has limitations for monopiles exceeding 2 m in diameter.

Yang et al. (2017) investigated monopile lateral response/deformation under lateral cyclic load using the DSM in the FE program; evaluated the power and logarithmic models for predicting accumulated pile displacement, and proposed/developed a design model that is validated against field tests on scaled monopiles. The incorporation of a subroutine of DSM in the FE program enabled the quantification of load character effect, pile embedded length, and load eccentricity on the displacement development of the monopile. The proposed model accounts for the influence of loading cycle number, load amplitude, and pile embedded length on the accumulated pile displacement. Practical implications are the evaluation of monopile displacement models for OWT design validation; and the recommendation of lateral displacement criteria for determining monopile ultimate capacity under lateral monotonic loading. The ultimate load capacity is determined based on displacement and rotation criteria at the mudline. The power and logarithmic models predicted accumulated monopile displacement effectively, while load eccentricity and amplitude influenced the power model parameter.

Zha et al. (2022) proposed a simplified model that predicts the accumulated displacement of large-diameter semi-rigid piles under cyclic loadings accurately in soft clay based on two cyclic loading factors. The proposed two factors approach considered – pile diameter, loading profile, and undrained shear strength. The model is validated with centrifuge data and the HARM model. Calibration is informed by centrifuge test data for ratcheting model. The authors aimed to investigate accumulated displacements under stochastic loadings using fitting parameters. Monopile displacements under storm and fatigue loading histories were also investigated. Methods used are – a simplified model with two cyclic loading factors for displacement prediction; incremental method and accelerated method for displacement prediction validation; and a unified soil reaction model based on soil flow mechanism. The limitation encountered is that the simplified model may not consider all factors affecting displacement accurately.

Liu & Kaynia (2022) studied monopile response under undrained cyclic loading in sand based on numerical models enhancing understanding of monopile-soil interaction and optimized engineering design procedures in offshore wind farms. Effects of geometry and static vertical load on lateral response were analyzed. The numerical analyses utilized the 3D FE method with the SANISAND-MSu model. Methods used are 3D FE with SANISAND-MSu; implicit 3D FE analysis method; and OpenSEEs for 3D FE mesh used in simulation cases. A practical implication is that the SANISAND-MSu model enhanced monopile design with pore water pressure considerations; and reliable simulation results for pore pressure evolution and pile displacement accumulation when a simple anisotropic sand model with a memory surface is adopted. The findings of the study revealed that the SANISAND-MSu model accurately simulates sand undrained cyclic behavior; soil fabric effects reflected in hardening coefficient and memory surface; static vertical load had minor effects on pile cyclic lateral response, thus, monopile lateral response is influenced by geometry, not static vertical load; and soil drainage condition crucial for optimized monopile design. For a given pile diameter, accumulated pile head displacement decreased linearly with increasing pile embedded length but increased with increasing eccentricity. The model limitation is that the implicit 3D FE method has a long computational time, and accuracy depends highly on constitutive models used in simulations.

Sun et al. (2023) investigated the cumulative deformation of large-diameter monopiles in saturated sand; and developed numerical and analytical models to predict lateral monopile response. The model is validated by triaxial and centrifuge tests. The analyses of cyclic responses of monopiles under different loading conditions indicate that pile diameter significantly affects cumulative deformation in lateral loading. Comparison is made between cyclic responses in saturated and no-pore pressure cases. Methods used are numerical modeling with FLAC3D validated by triaxial and centrifuge tests and an analytical model developed based on a parametric study for cyclic loading. The authors considered soil dilatancy and densification around monopiles in saturated sand. Results showed that larger subsidence (and less capacity of soil around the pile) in saturated sand due to transient excess pore pressure accumulation and dissipation caused larger cumulative deformation; influence parameters are independent of pile diameter and cyclic load level; sand permeability and frequency have little effect on cumulative displacement. Limitations encountered are differences in boundary displacement affected calculated versus measured test results. Mesh size sensitivity is conducted for accurate results and computational efficiency. It was recommended to further investigate applicability of analytical model with full-scale piles.

Haiderali et al. (2023) investigated cyclic lateral loading on monopiles in structured London Clay, with the simulation of the cyclic behavior done based on the sub-loading t_{ij} constitutive model. The authors aimed to analyze the response of large-diameter monopiles to one-way and two-way cyclic loads and define time-varying cyclic lateral load parameters for the monopiles. Methods used are implicit 3D FE analyses on cyclic lateral loading; simulation of cyclic behavior in clay using sub-loading t_{ij} model; symmetric and asymmetric two-way and one-way low-frequency cyclic loads. A practical implication is that clay structure affects cyclic pile behavior; neglecting it is conservative in monopile design, hence, experimental research on monopiles in London Clay is recommended. Ratcheting occurs with cyclic loading, with stiffness (secant) degradation over cycles, though the rate of degradation is reduced with increasing cycles as well as decreased ratcheting rate. This behavior from London Clay is in contrast with several soil types/conditions say sand whereby the secant stiffness increases instead. The results showed that one-way loads induced greater pile lateral deformation and rotation at the mudline than two-way loads, with findings suggesting strain softening, reconsolidation, and densification during cyclic loading. Lateral displacement accumulation was higher for asymmetric one-way loads. Limitations in the study are that anisotropy of London Clay is not modeled in the study; over-consolidation ratio (OCR) and OCR variation are not considered in the analysis.

Gao et al. (2023) presented a bounding surface stiffness degradation method (B-SDM) that models long-term ratcheting response in sand for OWT foundations – the aim is to address drawbacks in cyclic SDM approach. Advanced constitutive models for cyclic sand behavior are proposed. The B-SDM method is a hybrid strain accumulation approach for cyclic loading in OWT design and is supported under a base elastoplastic model with a cyclic strain accumulation scheme validated. The base elastoplastic constitutive model captures the stress-strain relationship in the first load-unload cycle and B-SDM is used for modeling subsequent cycles based on a strain accumulation scheme in which the plastic modulus and dilatancy relationship are scaled according to a strain accumulation law. The base constitutive model is established based on the bounding surface concept and considers strain-hardening and plastic volume change before failure.

The numerical approach adopted is B-SDM for cyclic loading analysis with an explicit skip-cycle strain accumulation type model for cyclic response simulation. The 3D FEA-based design checks for long-term cyclic ratcheting are crucial. The practical implication is that the B-SDM method predicts sand response in the first regular cycle accurately; and it is ideal for monopile design calculations, superior to the industry standard approach; though, it requires further verification and updates in strain accumulation formulations for shear and dilatancy equations in stiffness degradation phase modeling. Findings revealed validation of the B-SDM method with single-element test data on sand. The method is practically stable and allows decoupled modelling of cyclic volumetric and shear strains; the cyclic strain accumulation model is used in 3D FEA monopile response. The model needs validation in field tests for cyclic loading. The limitation encountered is the lack of extensive cyclic test data for hypothesis confirmation.

Houlsby & Richards (2023) developed bounding surface models in a compact form within the hyperplasticity theory defined completely with two potentials similar to the case of multi-surface plasticity implementation. The developed models have bounding surface characteristics and real data calibration. The requirement for the model is a single yield surface; the curve is a smooth response, and comparisons are made with complex tests. Model calibration is informed by a monotonic test. The models combined features of both multi-surface and bounding surface (or two-surface) models, and obey thermodynamics laws. There's a lack of exploration on inner yield surface evolution during plastic straining, thus, the approach adopted can reproduce inner yield surface features and gradual plastic strain development. Limitation of the model are non-inclusion of complex soil behavior features, and the inner yield surface size and shape evolution is not explored. The developed models are illustrated with one-way, two-way cycling, and 2D stress paths.

Numerical Modelling of Cyclic Loading: Practical Implications & Field Applications

Albiker et al. (2017) discussed large-diameter pile behavior in the sand under arbitrary cyclic loading conditions for offshore wind energy converters and investigated the predicted behavior of displacement accumulation rates under different loading types – one-way and two-way cyclic loading. Methods used are the prediction of displacement accumulation for load spectra (consisting of packages of arbitrary loads) using empirical approaches and conducting 1 g model tests to validate the hypothesis on loading type effects. Asymmetric two-way loading affects displacement accumulation differently for flexible piles – here the asymmetric two-way loading was not more unfavorable than the

one-way loading. The study found for almost rigid large-diameter piles, the effect of the loading type on the rate of displacement accumulation could be accounted for by a function almost independent of the system parameters – pile stiffness or relative density of the sand, but dependent on load eccentricity. Results indicated that the maximum accumulation rate occurs for asymmetric two-way loading. Limitations of the model are limited clarity on behavior under cyclic two-way loading; and the difficulty in comparing parameters due to load dependency. There is a need for more research on flexible pile-soil systems under cyclic loading.

Liu et al. (2022) investigated monopile tilt under cyclic lateral loading in sand using 3D FE modeling; assessed Miner's rule validity for monopile tilting under multi-amplitude cyclic loading; and highlighted loading history effects on monopile tilt under irregular loading and soil behavior in global pile response. The paper aimed at exploring implications of idealizing external loading history on monopile tilt prediction accuracy, and enhancing existing engineering methods for monopile serviceability and fatigue analysis. Methods used are – step-by-step implicit 3D FE modeling with SANISAND-MS for cyclic lateral loading; numerical investigation of Miner's rule for monopile tilting under cyclic loading; and idealization of irregular loading histories into regular versions for analysis – with loading packages sorted in ascending amplitude order. The use of SANISAND-MS model is to achieve a reliable simulation of sand's cyclic ratcheting. Gap in knowledge is on the aspect of Miner's rule application limitations in monopile tilting under cyclic loading, coupled with insufficient exploration of irregular loading history effects on monopile behavior. Practical implications of the study are partial validation of Miner's rule under specific cyclic loading conditions; loading history idealization can represent irregular loading sequences effectively; and monopile tilt behaviour under cyclic loading is closely linked to soil response.

Results indicated that Miner's rule is not always applicable to monopile tilting under cyclic loading i.e. Miner's rule is partially validated for monopile tilt under cyclic loading – this validation is assessed based on the results of 3D FE parametric analyses; dense sand is more sensitive to load sequence than loose sand; loading parcel order has minor effects on pile head displacement. Regular loading parcels represent irregular loading history under drained conditions. Limitations encountered are that Miner's rule is not universally applicable to all cases considered herein, and irregular loading histories translation may not always be accurate.

Lopez-Querol et al. (2023) presented numerical methods for OWT foundation cyclic SSI analysis using advanced numerical techniques; and discussed unique loads and design considerations for wind turbine foundations. The authors aimed to investigate the long-term performance of OWT foundations and analyze cyclic and dynamic loads on the foundation (including dynamic loading effects and resonance analysis). Summary of numerical analysis methods used in monopile design are presented – these are grouped into 3 namely simplified method (closed form solutions), standardized method (code-based computations) based on p-y analysis i.e. nonlinear beam supported on Winkler foundation, and advanced analysis method. The focus was on the latter based on the Discrete Element Method (DEM) coupled with the integration time step method for numerical analysis. Monopile-soil interactions using open-sourced DEM code and stiffness variations are investigated. Results indicated that progressive pile-head displacement is observed with increasing number of cycles under dynamic loading conditions; and residual errors accumulate with more time steps in simulations. Limitations of the model are – simplified SSI estimation, neglect of cyclic soil property changes; inability to study progressive foundation tilt under cyclic loads; oversimplified pile bending and lateral deflection considerations; inadequate accounting for interface opening, impacts during dynamic loading; and the need for advanced constitutive models to simulate cyclic behavior.

Nigitha et al. (2023) studied the monopile behavior under one-way and two-way loading based on FE analysis (PLAXIS 3D) of monopiles under lateral cyclic loading scenarios. Numerical studies were conducted on a 6 m diameter monopile by varying amplitudes and embedded length ratios. The monopile was subjected to both one-way and two-way symmetric lateral cyclic loading with an amplitude of 30 %, 40 %, and 50 % of the ultimate capacity of the pile. The rate of accumulated displacement increased by a factor of 0.3 – 0.7 when the load amplitude increased from 30 % to 50%. Methods adopted are the p-y method for monopile foundation design using a simplified approach; power law and logarithmic law for predicting accumulated displacement under cyclic loading. The practical implications are validation of monopile behavior under lateral cyclic loading using centrifuge tests; studies on the effect of load amplitude and embedded length on lateral displacement; and identification of cyclic stiffness changes and displacement accumulation

rates under different conditions. Results showed that monotonic tests established the monopile's ultimate capacity using lateral displacement, while a parametric study on monopile under cyclic loading analyzed displacement and stiffness. Limitations are the model lacked strain and pore-pressure accumulation under cyclic loading; the hardening soil model has drawbacks in predicting hysteresis behavior; the Masing rule application may not be suitable for increasing cycles; and the HS small model (hardening soil model with small strain stiffness) predicts smaller displacements in two-way cyclic loading i.e. model limitations in predicting displacements accurately under two-way loading. Takeaways from the study are – lateral displacement increased with cycles in one-way loading; peak lateral displacement reduced with cycles in two-way loading; attenuation parameter increased with load amplitude in one-way loading; and rate of displacement accumulation was higher at lower L/D ratios; cyclic secant stiffness increased with cycles, independent of loading nature.

Zha et al. (2023) presented a foundation model for fatigue life prediction under the hyperplasticity framework incorporated in the NREL FAST aero-hydro-servo-elastic simulation model that accounts for damping, stiffness variation, and ratcheting (accumulated displacement), and enhanced accurate fatigue damage estimation under cyclic loadings – considering that the rigid foundation modeling assumption has been widely used in most of the coupled integrated simulation software programs making for an inaccurate fatigue damage estimation as it does not consider soil stiffness and damping. The proposed model is validated using centrifuge test data. Findings showed wind loads and midline bending moments vary nonlinearly with wind speeds; midline bending moments differ in operational and non-operational cases; the validity of the model is demonstrated through hysteresis loops and simulations based on nonlinear displacement curves due to soil resistance; non-operational cases showed higher fatigue damage due to intense hydrodynamic loads; and hardening model can be used for simplicity in fatigue damage estimation. The model is limited to isotropic clay (not sand nor layered soils) for monopiles under cyclic loadings; the installation method effect on pile response is not considered; and simplification of foundation effect on support structure as an external force.

Chaloulos et al. (2024) presented the results of 3D coupled cyclic time history numerical analyses of monopiles supporting a 12 MW OWT to assess conservatism in monopile analysis approaches and evaluate the impact of drainage conditions on monopile response accurately. The monopile is installed in dense cohesionless soils and subjected to a 600-s load history corresponding to the high phase of a 35-h design storm. The authors validated a Ta-Ger model for the monopile foundation in dense cohesionless soils, with the numerical model capturing complex soil response under drainage simulation and deformation mechanisms accurately. The calibration is informed by site-specific tests. The practical implications of the study are that drainage affects monopile response, leading to conservative or unconservative outcomes; the advanced numerical analyses complement the standard methods to assess uncertainties accurately. Drainage affects soil response, leading to liquefaction typically in low-permeability soils (for example – cohesionless soils with low-plasticity fines) – this may induce high rotations above allowable limits. On the contrary, foundation systems that can drain effectively within each cycle, develop moderate excess pore pressures which do not jeopardize performance. Results indicated that the soil response analyzed under different drainage conditions showed varying ratios of excess pore pressures during loading. Drainage impacts monopile response, influencing stability and deformation, and time history analyses provide site-specific clarity on drainage effects.

Multidirectional Loading

Nanda et al. (2017) investigated monopile performance under unidirectional and multidirectional cyclic loading, with observation of sand flow and vertical movement during cyclic loading. The tests were conducted on a 530 mm long model monopile in a sand bed – a mobile loading platform was manufactured to apply loading on the pile in various directions. The authors tested two-way and one-way cyclic loading on model monopiles; and analyzed the effects of pile end conditions and cyclic load patterns. The practical implication of the study is that multidirectional cyclic loading affects monopile stiffness and displacement significantly, and closed-ended piles show higher stiffness than open-ended piles under loading. Results showed model tests presented in dimensionless form, focusing on soil-pile system response. Parameters like stiffness and deformation are evaluated under horizontal cyclic load. Soil-pile stiffness increases with the number of load cycles; and multidirectional loading results in significantly higher stiffness in monopiles with more load cycles than the unidirectional case – most likely attributed to shear deformation of a larger volume of soil mass adjacent to the pile. Open-ended piles had more horizontal displacement than closed-ended piles; vertical deformation is

observed under multidirectional cyclic loading; and stiffness did not significantly increase under multidirectional two-way cyclic loading.

Hong et al. (2023) proposed and introduced a multidirectional bounding-surface-based cyclic model in both sand and clay that analyzes pile responses and lateral soil-pile interaction under multidirectional lateral cycling effectively. The model is validated with centrifuge and 1 g experimental test results on piles under unidirectional and multidirectional cycling (with various paths) experiments. The authors developed a multi-spring cyclic soil-pile model for OWTs within the plasticity framework, and analyzed the effect of changing cyclic loading direction on soil-pile stiffness; the model captures multidirectional cyclic hysteresis and shakedown with six parameters. The practical implication is enhanced OWT design under typhoon loadings. The proposed model i.e. multi-axial bounding surface p-y model, showed lateral pile displacement accumulation under multi-directional cycling, while the multi-spring model reveals degradation of global soil-pile stiffness under cyclic loading. The lateral cycling reduces global soil-pile stiffness, increasing lateral displacement accumulation.

Xu et al. (2024) presented an improved multi-springs model for predicting the responses of suction caissons under cyclic lateral loading. The authors carried out an enhanced model under the bounding surface plasticity theory for caisson responses under multidirectional cyclic lateral loading, incorporating a multi-spring system for dynamic analysis of caisson-based OWTs. The verification is informed by unidirectional and multidirectional laboratory tests for monopod caisson. Methods used in the study are enhanced multi-springs model with p-y and t-z springs; structural mechanics module (SMM) in COMSOL and SSI module (SIM); cyclic p-y, t-z, and Q-z models for foundation displacement. The model supports the loading and unloading behaviors at the caisson-soil interface. The practical implication of the study is that soil densification strengthens the passive side, thus, affecting foundation stability and impacting caisson displacement. The enhanced model replicated caisson deformation accurately and can effectively capture the complex SSI under cyclic loading, while neglecting the combined spring effect leads to an overestimation of caisson deformation. There is a negligible impact of the spring group number on computational outcomes. Limited cycle numbers may hinder reaching a state of cyclic shakedown, and there are challenges in stable foundation deformation under higher load coefficients.

Macro-element Models

Zhang et al. (2023) presented a macro-element model for mono-bucket foundations supporting OWTs in clay that captured cyclic softening under real-time displacement representation with high computational efficiency and accuracy. Cyclic softening is a typical characteristic of clay under cyclic loading. The calibration of the parameters for the model is informed by FEA. Methods adopted in the study are multi-surface plasticity with kinematic and isotropic hardening rule; incorporation of cyclic contour diagram approach to simulate and capture cyclic softening behavior of the soil; and calibration of model parameters using uniaxial quasi-static load-displacement curves from FE analyses. The load point and yield surface differences are evaluated for convergence, while plastic displacement is calculated by plastic multipliers and flow vectors. The limitation of the model is that it ignored the consolidation effect on soil strength during wind turbine operations (long-term operation of wind turbines), and errors in load point calculations may require smaller time increments. There is good agreement of the model with FE analysis for uniaxial cyclic loading, and slight to moderate discrepancies for combined cyclic loadings.

Gorini & Callisto (2023) presented a hyperplastic macro-element model that simulates multidirectional lateral soil-pile interaction in nonlinear analysis of structures, with model predictions validated under monotonic and dynamic loads – experimental data and advanced numerical modeling. The foundation failure conditions are described by hyper-ovoidal ultimate limit state surface in the force space – calibrated through standardized procedures, and implementation is done in OpenSees for earthquake engineering applications – focusing on foundation design under various load combinations and seismic performance. Methods used in the study are thermodynamic inertial macro-elements (TIMs) for geotechnical system response simulation and calibration of macro-elements for piled foundations based on ULS surface. The calibration is based on traditional methods for ease of use. The inertial effects developing under dynamic loading can be reproduced by coupling the macro-element with the participating masses of the soil-foundation system. Plastic behavior is modeled with yield surfaces for cyclic response. The plastic behavior controlled by a series of yield surfaces with

kinematic hardening produced the desired directional coupling and allowed the modelling of the cyclic response and irreversible deformation of the foundation. The contribution of the paper is the macro-element model directional coupling due to plasticity, seismic performance, and dynamic response.

Meng et al. (2024) addressed the challenge of numerical analysis of the monopile foundation for an OWT subjected to complex environmental loads. The authors proposed a macro-element model for accurate simulation of OWT supported on the large-diameter monopile foundation in sand under lateral cyclic loading due to wind and wave loads that combines limit analysis and hypoplastic theory for the accurate numerical tool. The calibration of the model is informed by centrifuge test data and 3D FEA. Methods deployed in the model are the numerical limit analysis method for 3D failure envelope surface; the hypoplastic macro-element model based on basic principles of hypoplastic theory; and the utilization of the FELA software program for determining the bearing capacity of monopile. The model provided accurate foundation stiffness and damping simultaneously. Practical implications are the simplification of complex pile-soil interaction problems using a macro-element model with high accuracy, and reduction in computational costs while maintaining performance accuracy. An analytical formula for failure envelope surface is developed for large-diameter monopiles. The result indicated that the wind load significantly impacts OWT rotation, while the wave load has minimal influence. The 3D failure envelope surface analysis reveals an inclined elliptical surface in the H-M plane.

Gaps in Research

Despite these advancements, significant gaps remain in the available literature. One major gap is the lack of constitutive models that simultaneously account for both damping and stiffness in SSI. Most existing models focus on one aspect but fail to integrate both, which is critical for accurate fatigue life prediction and structural analysis in an integrated design under cyclic loading. Furthermore, there is a scarcity of models capable of handling coupled multidirectional loading while also accounting for displacement accumulation under complex cyclic loading, such as ratcheting. This gap highlights the need for a comprehensive model that can address these challenges simultaneously.

These gaps underscore the necessity for a novel constitutive model that integrates both damping and stiffness, coupled multidirectional loading, and displacement accumulation under complex cyclic loading conditions. The proposed CLAP model aims to fill this gap by providing a more accurate and comprehensive tool for predicting the behavior of OWT foundations under various environmental loads.

4. CLAP MODEL

4.1 Background

The CLAP model is implemented as a multi-surface kinematic hardening (MSKH) model with a hardening rule based on Ziegler's assumption. The macro-element model is rate-independent, offering foundation stiffness and damping that are unaffected by the loading frequency and excluding soil inertia effects. A key advantage of MSKH models is their ability to accurately capture the nonlinear behavior of geo-mechanical materials across a wide range of strain amplitudes. This makes them particularly valuable for applications involving modeling OWT supported on monopile foundations. The model is used to assess the response of offshore monopiles at the mudline/seabed level.

A central concept in this model is the "back Stress", which is a state-dependent variable that relies on the current state of the system. The back-stress functions as a memory mechanism, enabling the accurate tracking of the yield surface's position during incremental analysis. While modern complex constitutive models may use up to 30 state variables, the back-stress is often the most critical for capturing kinematic hardening (KH) behavior.

The yield function is elliptical but is transformed into a circular function for computational efficiency. Additionally, the optimal number of yield surfaces depends on the specific constitutive model; for the CLAP model, 15 yield surfaces is proposed as optimal. However, increasing the number of yield surfaces can lead to higher computational costs and possibly potential numerical instability depending on the number of data points in the load-displacement input files used for model calibration.

The CLAP model supports both displacement-controlled and load-controlled formats. These formats can accommodate applied displacements and forces up to the maximum limits defined by the load-displacement curves, based on the input file used during backbone curve calibration. For response in load-controlled, the model employs a robust Newton-Raphson algorithm in a 4-DOF compatible format, where the full stiffness matrix is used to compute displacement increments and update the global displacement vector, ensuring accurate results. Although using diagonal coefficients of the stiffness matrix with the corresponding DOF index in a loop could improve computational efficiency with minimal loss of accuracy, the adopted approach relies on the full matrix to maintain precision. The load-controlled implementation can be easily adapted to include vertical DOF components. However, the implementation focuses on lateral multidirectional loads in the x-y plane. Extension can be done on the model to account for vertical DOF components in both load-controlled and displacement-controlled settings. This is particularly relevant for load scenarios with significant vertical contributions, such as seismic loading or anchor piles with substantial vertical resistance (e.g., suction caissons with semi-taut mooring lines).

The merger to achieve the current model can be likened to the substrate-matrix relationship in composite materials, such as a concrete-epoxy system, where the matrix (e.g., epoxy) adheres to the substrate (e.g., concrete). In this novel constitutive model, REDWIN acts as the substrate/host, as it is already an integrated model for OWT, accounting for multidirectional loading. The HARM implementation, which accounts for ratcheting, is then incorporated into REDWIN.

The programming task involved carefully debugging, translating, and modifying the original REDWIN model, which was written in FORTRAN, into Python/MATLAB. These modifications included adding functions to handle singularity issues, such as floating-point division errors caused by the divisor matrix being singular, nearly singular, or ill-conditioned. Additionally, the numerical implementation addressed the challenge of accurately representing the complex FORTRAN control flow, which relied heavily on numerous GOTO statements. The implemented code successfully captured this control flow efficiently.

4.2 CLAP Model

The CLAP model builds upon the foundation established by the REDWIN model under Section 3.2.4, incorporating an advanced approach to account for ratcheting effects. This addition makes the CLAP model more versatile and accurate

in simulating the complex behaviors observed in offshore foundations subjected to cyclic loading. Ratcheting, which is the progressive accumulation of plastic strain under cyclic loading, is a significant phenomenon in many engineering applications, particularly in monopile foundations subjected to lateral loading. The following sections detail the various components and implementation steps of the model.

4.2.1 Model Overview

The CLAP model is an advanced mathematical framework used to simulate the behavior of piles under various loading conditions by utilizing a MSKH model with circular yield surfaces. The model accounts for both elastic and plastic deformations, including ratcheting effects. The model reads input soil foundation properties from files that contain the elastic stiffness matrix, the nonlinear load-displacement curves used for model calibration; calibrates the model, initializes parameters, computes forces based on the given displacement increment (assuming displacement-controlled mode), considering plastic deformation and ratcheting contributions. The elastic stiffness matrix describes the elastic response of the pile at the seabed. The yield surfaces define the plastic behavior based on calibration parameters S and K_P denoting the size of the yield surface, and the plastic stiffness respectively.

The generalized force vector σ and work-conjugate generalized displacement vector ϵ is given as;

$$\sigma = \begin{bmatrix} H_y \\ H_x \\ M_y \\ M_x \end{bmatrix}; \qquad \epsilon = \begin{bmatrix} u_y \\ u_x \\ \theta_y \\ \theta_x \end{bmatrix}$$

In the model, the hardening rule is maintained and does not directly incorporate ratcheting, thus, modifying the evolution of the back-stress is avoided. The hardening rule is presented as earlier shown:

$$d\alpha_j = \boldsymbol{K}_j^p . d\epsilon^p$$

Where $\boldsymbol{K}_j^p$ is the plastic stiffness matrix at the j-th yield surface. The direct exclusion of ratcheting in the hardening rule means that the yield surface remains unaltered. The consistency condition in the model ensures that the stress state remains on the yield surface during plastic deformation. This condition is essential for maintaining the accuracy of the model, as it prevents the stress state from violating the yield criterion.

4.2.2 Numerical Implementation

The incremental response in the CLAP model is decomposed into elastic and plastic components including ratcheting which is a dissipative component.

$$d\epsilon = d\epsilon^e + d\epsilon^p + d\epsilon^R$$

Where ϵ, ϵ^e, ϵ^p and ϵ^R are the generalized total displacement, elastic displacement, plastic displacement, and displacement due to ratcheting respectively. The model iteratively calculates these increments to track the foundation's behavior under applied loads.

The model implementation follows the computation of the incremental displacement at the seabed and transforms it according to the spherical yield surface coordinate system. The trial force is determined based on the elastic response and checked against yield surfaces.

Given the trial stress σ_{n+1}^{trial} and trial back-stress $\alpha_{j,n+1}^{trial}$:

$$\sigma_{n+1}^{trial} = \sigma_n + \boldsymbol{K}.\Delta\epsilon$$
$$\alpha_{j,n+1}^{trial} = \alpha_{j,n}$$

Note that for the initial step, incremental total strain $\Delta\epsilon$ is assumed. Plastic correction/adjustment will eventually be taken into account if it turns out that the yield surface is active.

If yielding occurs, plastic displacements are calculated, the yield surfaces' positions are updated, and incorporation of ratcheting effects. This involves checking whether the yield surface j is active for the trial stress and back-stress values. The yield criterion is evaluated for each yield surface:

$$f_{j,n+1} \geq 0$$

The yield function checks whether the trial force lies within the yield surface, indicating plastic deformation, while the model updates force by accounting for both plastic strain corrections and ratcheting, ensuring a realistic response under cyclic loading. If the criterion is satisfied, it indicates that the yield surface is active, and plastic deformation may occur. If the criterion is not met, the foundation remains in the elastic region, and no plastic adjustment is needed. For active yield surfaces, the stress state and back-stress must be updated using the associative flow rule and Koiter's (Koiter, 1953) rule to ensure that the yield criterion is satisfied at the end of the step.

The updated stress is computed as:

$$\sigma_{n+1} = \sigma_{n+1}^{trial} - \boldsymbol{K}.\sum_{j=1}^{i} \Delta\lambda_j . \left\{\frac{\partial f_j}{\partial \sigma}\right\}_{n+1} - \boldsymbol{K}.\sum_{j=1}^{i} sign(\sigma).\left\{R_0\left(\frac{k_j}{k_U}\right)\left(\frac{\beta_r}{\beta_0^r}\right)^{-m_r}\left(\frac{|\sigma|}{k_U}\right)^{m_s}\right\}_{n+1} . |\Delta\epsilon_j^p|$$

Where σ is generalized stress/force, ϵ is generalized strain/displacement, i is active yield surface number.

The above updated stress computation accounts for the plastic correction and ratcheting contribution assuming that the yield surface j is active ($f_{j,n+1} \geq 0$). Hooke's law is satisfied for the elastic portion of the strain, and also this aligns with the principles of elastoplasticity by iteratively correcting the stress to maintain the validity of the yield surface. This plastic correction ensures that the updated stress state lies on the yield surface, aligning with the conditions set by the yield criterion, flow rule, and hardening rule.

The updated back-stress is computed as:

$$\alpha_{j,n+1} = \alpha_{j,n+1}^{trial} + \Delta\lambda_j . \boldsymbol{K}_j^p . \left\{\frac{\partial f_j}{\partial \sigma}\right\}_{n+1}$$

This remained unchanged from the earlier established REDWIN model.

The plastic multipliers $\Delta\lambda_j$ are computed iteratively until convergence is achieved. The consistency condition requires that the sum of the yield functions $f_{j,n+1}$ for all active yield surfaces satisfies the following condition:

$$\sum_{j=1}^{i} |f_{j,n+1}| < tol.S_1$$

Here S_1 corresponds to the strength (S_j) of the inner-most yield surface in a MSKH model. This substitutes the undrained shear strength s_u which applies to cohesive soil. Thus, this approach applies to both cohesionless and cohesive soil. Recommended value for tolerance tol is 1×10^{-6}. To ensure convergence, iterative methods are used with sub-stepping to handle nonlinearities. If convergence is not achieved, sub-stepping is activated whereby the model divides the incremental strain into smaller steps by a factor of 10 and repeats the computation process, thereby ensuring the numerical stability and accuracy of the solution. After convergence is achieved, the final stress state σ_{n+1}, back-stress $\alpha_{j,n+1}$, and plastic multipliers $\Delta\lambda_j$ are updated for the next increment. To preserve the memory i.e. load history of the model, the updated values based on the displacement, force in the transformed coordinate, back-stress in the transformed coordinate, and the outermost active yield surface are stored as the state variables, saved and retrieved at the next increment.

To handle the 4D yield surface efficiently, a geometric transformation is applied, converting the ellipsoidal yield surfaces into spherical shapes in the transformed coordinate system. This transformation simplifies the computations and enhances the numerical robustness of the model. Once the constitutive response is solved in the transformed system, the updated stress state is transformed back to the original coordinate system.

The goal of the macro-element model in incremental response is to achieve this relation at the end of the step;

$$\sigma = \sigma_0 + \Delta\sigma = \sigma_0 + \boldsymbol{K}.\Delta\epsilon^e = \sigma_0 + \boldsymbol{K}.(\Delta\epsilon - \Delta\epsilon^p - \Delta\epsilon^R)$$

Where the generalized force at the beginning of the step is σ_0.

4.2.3 Step-by-Step Numerical Implementation Summary

1. Calibration: Calibrate the model using elastic stiffness and backbone curves.

- The calibration process involves specifying the coefficients of the elastic stiffness matrix and the nonlinear backbone curves.
- These curves can be obtained from experimental tests or numerical simulations.
- The calibration parameters K_P (stiffness) and S (strength or radius) are determined from the force-plastic displacement relations, transformed into the spherical coordinate system.

2. Initialization: Set initial conditions.

- Define the initial stress σ_0, initial back-stress $\alpha_{j,0}$, and initial displacement ϵ_0.

3. Incremental Step: Compute trial stresses and back-stresses.

For each incremental step n to $n+1$:

- Compute the trial stress σ_{n+1}^{trial}
- Compute the trial back-stress $\alpha_{j,n+1}^{trial}$

4. Yield Surface Check: Determine active yield surfaces.

Check if the yield surface is active for the trial stress and back-stress:

- If $f_{j,n+1} < 0$, the constitutive behavior is in the elastic region, and no plastic correction is needed. Go to Step 9.
- If $f_{j,n+1} \geq 0$, the yield surface is active, yielding has occurred and plastic correction is required.
- Enforce the yield criterion $f_{j,n+1} = 0$ at the end of the step.

5. State Update: Update stresses and back-stresses using flow and hardening rules.

- Apply the plastic correction to adjust the trial stress and back-stress so that the yield criterion is satisfied.
- Use Koiter's rule (Koiter, 1953) and the flow rule to update the stress state σ_{n+1}.
- Update the back-stress $\alpha_{j,n+1}$ using the hardening rule.

6. Iteration: Iterate to satisfy yield criteria.

- Ensure that the updated stress and back-stress satisfy the yield criterion $f_{j,n+1} = 0$ at the end of each step.
- Iterate $\Delta\lambda$ i.e. to find the correct plastic multiplier, until convergence:

$$\sum_{j=1}^{i} |f_{j,n+1}| < tol.S_1$$

7. Transformation: Transform to and from spherical coordinates for efficiency.

- Transform the ellipsoidal yield surface into a spherical shape for efficient computation.
- Use the transformation matrix R to transform the generalized forces and displacements into the spherical coordinate system.
- Solve the constitutive relations in the spherical system and transform back to the ellipsoidal system after computation.

8. Sub-Stepping: Apply sub-stepping if necessary.

9. Update Generalized Forces: The forces are updated back to the ellipsoidal coordinate system. Prepare for the next displacement increment.

Steps 3–6 perform the consistency condition checks iteratively, to ensure that the yield criterion is satisfied ($f_{j,n+1} = 0$) after accounting for any plastic deformation, thus, ensuring that the constitutive response follows the defined elastoplastic behavior, maintaining the validity of the yield surface at each incremental step.

Detailed descriptions of the programming functions and key mathematical equations are presented in Appendix E, and also challenges encountered in implementing and improving the model are presented under Appendix F, including MATLAB code snippets on Newton-Raphson's algorithm for transformation to force-controlled mode.

4.3 STRUCTURE OF THE MODEL

4.3.1 Key Changes to the REDWIN Model

Implementation of the novel CLAP constitutive model followed an effective coupling of the REDWIN and HARM models. The key to this new integrated constitutive model for OWT foundations is the integration of the ratcheting contributions from HARM to the REDWIN model at the point of calculation of the incremental plastic displacement response. Here the plastic displacements are calculated and updated to the new position of the current active yield surface and the hardening variable i.e. the back-stress. A detailed mathematical representation of these key changes to obtain the CLAP model is presented below.

1. Initialization of the sum of the plastic displacements and ratcheting strains:

$$\sum \Delta\epsilon_k^P = 0 \quad \text{for } k = 1,2,3,4$$
$$\sum \Delta\epsilon_k^R = 0 \quad \text{for } k = 1,2,3,4$$

Subsequent steps follow a loop for each yield surface j up to the active outermost yield surface i (not the maximum specified number of surfaces). Thus given $j = 1$ to i:

2. The yield function gradient for the yield surface j is given as $\left(\frac{\partial g}{\partial \sigma_k}\right)_j$.

3. Calculation of the plastic displacements:

$$\Delta\epsilon_{kj}^P = \Delta\lambda_j \left(\frac{\partial g}{\partial \sigma_k}\right)_j$$
$$\sum \Delta\epsilon_k^P = \sum_{j=1}^{i} \Delta\epsilon_{kj}^P$$

4. Calculation of the ratcheting strains:

$$R_{kj} = R_0 \left(\frac{k_j}{k_U}\right)\left(\frac{\beta_r}{\beta_0^r}\right)^{-m_r}\left(\frac{|\sigma_k|}{k_U}\right)^{m_s}$$
$$\Delta\epsilon_{kj}^R = sign(\sigma_k) R_{kj} |\Delta\epsilon_{kj}^P|$$
$$\sum \epsilon_k^R = \sum_{j=1}^{i} \Delta\epsilon_{kj}^R$$

5. Updating the hardening strain:

$$\Delta\beta_r = |\sum \Delta\epsilon^R|$$
$$\beta_r = \beta_r + \Delta\beta_r$$

6. Computation of the plastic stiffness matrix for yield surface K_{Pl}^{j}.

7. Calculation of back-stress α increment due to plastic strain:

$$\Delta\alpha_{kj} = \Delta\lambda_j \left(K_{Pl}^{j} . \left(\frac{\partial \mathrm{g}}{\partial \sigma_k} \right)_j \right)$$

8. Updating the α:

$$\alpha_{kj} = \alpha_{0kj} + \Delta\alpha_{kj}$$

Again, notice that there was no need to add the ratcheting strain $\Delta\epsilon_{kj}^{R}$ multiplied by a ratcheting modulus, this is consistent with maintaining the shape of the yield surfaces. There was no need to alter this.

9. Finally, the trial force is updated including the plastic correction and the ratcheting contribution:

$$\sigma_k = \sigma_{0k} + K_e^T \left(\Delta\epsilon_k - \sum \Delta\epsilon_k^P - \sum \Delta\epsilon_k^R \right)$$

$$\sigma_k = \sigma_{0k} + K_e^T \epsilon_e$$

Note that in macro-element modelling displacement and strain can be interchanged, same also with force and stress.

The variables are in the transformed coordinate system. Where ϵ^P is plastic displacement ϵ^R is ratcheting displacement, ϵ_e is elastic displacement, ϵ is total displacement, R_{kj} is ratcheting parameter, R_0 is the initial ratcheting parameter, β_r hardening strain, β_0^r is initial hardening strain, α is back-stress at the end of the step, α_0 is back-stress at the beginning of the step, σ is the force at the end of the step, σ_0 is the force at the beginning of the step, K_{Pl} is plastic stiffness matrix, K_P is spring stiffness, S is spring-slider strength for a given yield surface (radius of the yield surface), λ_j is the plastic multiplier for a given yield surface, $\frac{\partial \mathrm{g}}{\partial \sigma}$ is the gradient of the yield function with respect to force, K_e^T is elastic stiffness matrix.

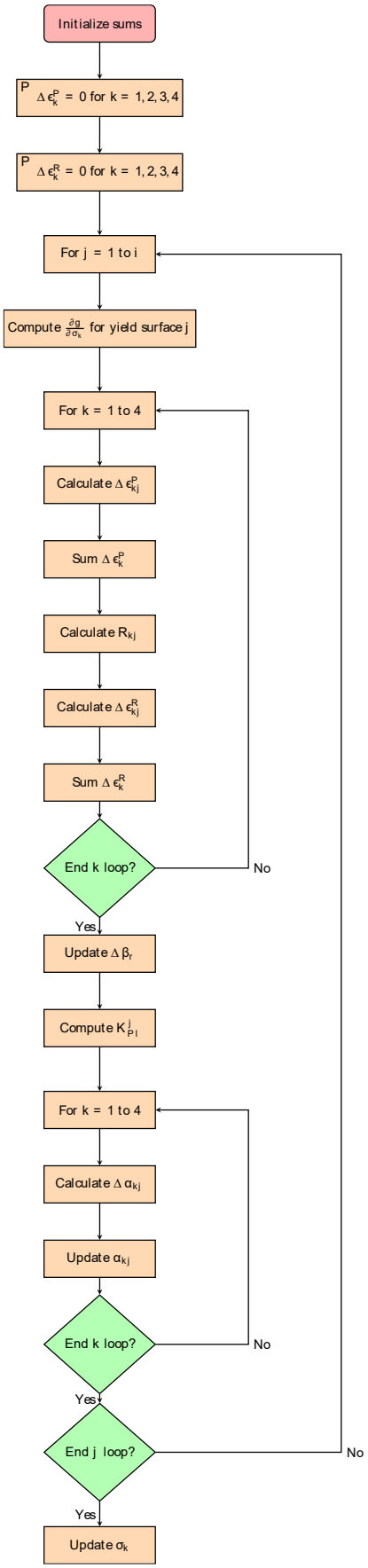

Figure 4. 1. Flow Chart Representation Key Changes to REDWIN Model (P = Summation).

4.3.2 Model Flow Charts

Figure 4.2 to Figure 4.4 presented below narrows down the key location of CLAP implementation from the entire model code (Figure 4.2), down to the subroutine responsible for calculating the response either force output if in displacement-controlled or displacement output if force-controlled (Figure 4.3), then to the section of the code for iterative incremental response (Figure 4.4).

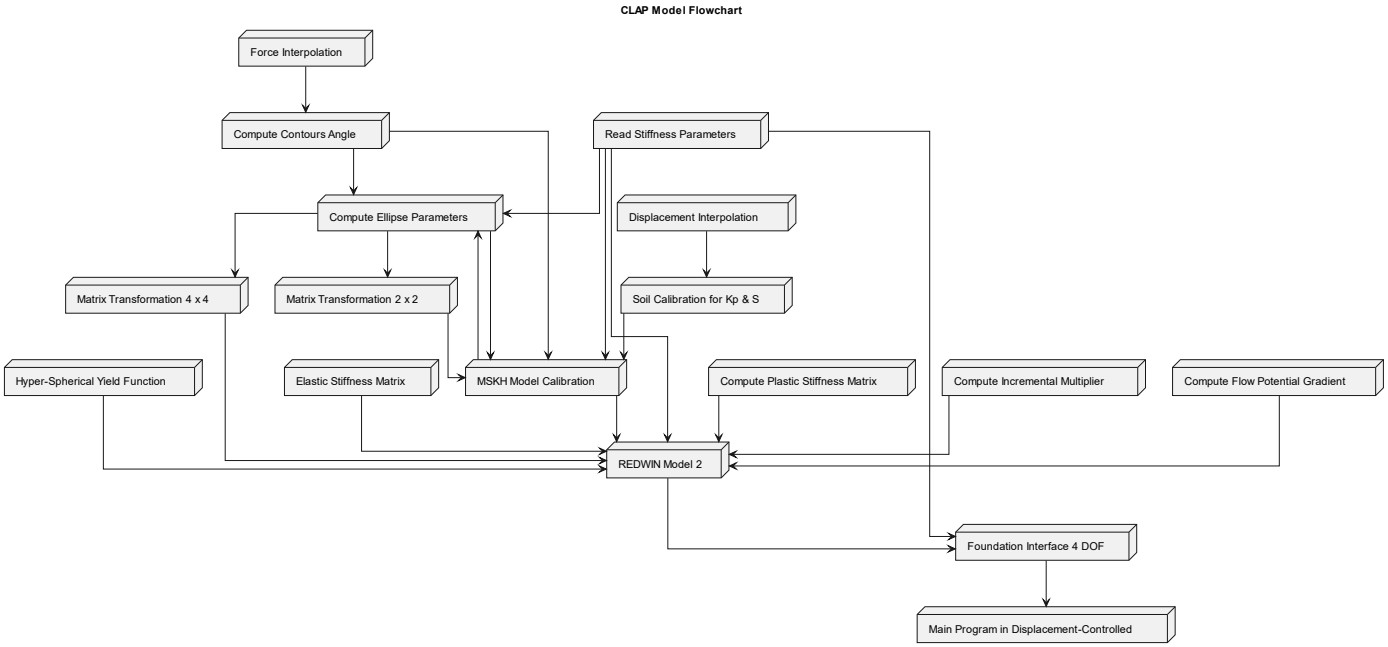

Figure 4. 2. Flow Chart of Representation of the Displacement-Controlled Model.

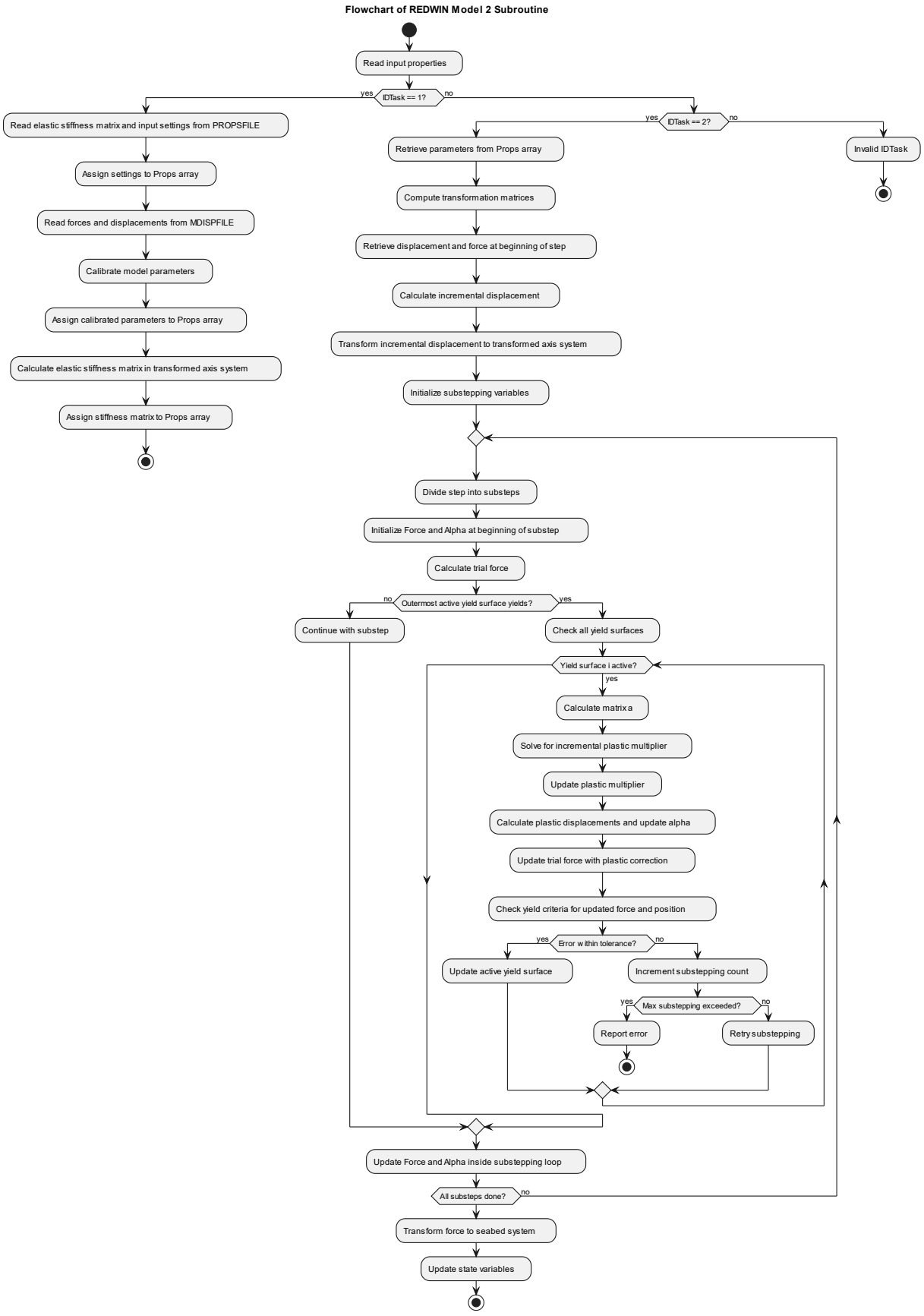

Figure 4. 3. Flow Chart of Force Calculation due to Applied Displacement in the Model.

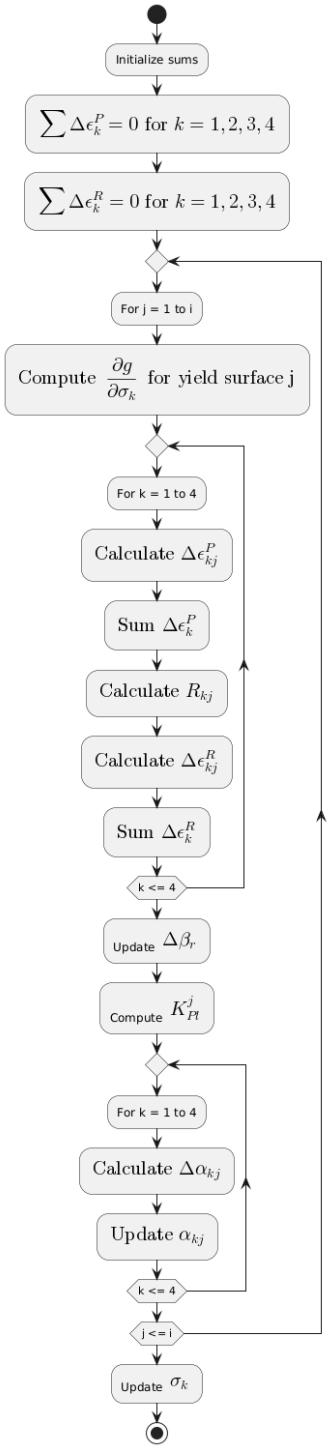

Figure 4. 4. Flow Chart of Incremental Response of the Model.

The above flow chart initializes the sums of plastic displacements and ratcheting strains. It iterates over each yield surface j up to the active outermost yield surface i. Within each yield surface, it computes the gradient of the yield function, plastic displacements, and ratcheting strains, updates the hardening strain, computes the plastic stiffness matrix, and calculates and updates the back-stress increment. Finally, the trial force is updated including the plastic correction and ratcheting contribution.

5. VALIDATION OF MULTIDIRECTIONAL CYCLIC LOADING

The operational loads of OWT supported on monopile foundations are typically relatively low compared to the ultimate capacity of the monopile foundation at ULS. These operational loads can be classified within the SLS and FLS. Under this load condition, the ratcheting effect is likely not noticeable in a few cycles say 10–100. This can be noticeable at 1×10^5 to 1×10^8 cycles i.e. considering long-term cyclic load over the lifetime of the OWT assuming there's no extreme event.

For understanding ratcheting effects in multidirectional cyclic loading in tens or hundreds of cycles, the loading conditions considered for most of the simulations under Chapter 5 and Chapter 6 are high to extreme load types i.e. $> 0.5 \times$ ULS capacity of the monopile foundation. Table 5.1 below shows the ratcheting parameter settings adopted throughout Chapters 5 and 6. It is the same parameter as that used under Section 3.1.5 except that β_0^r is changed from 1×10^{-5} to 1×10^{-4}.

Table 5. 1. Ratcheting Parameters Adopted for the Study.

Ratcheting Parameter	Value
R_0	1
β_0^r	1×10^{-4}
m_r	0.3
m_s	1

The elastic foundation stiffness matrix for the macro-element model is given below:

$$\boldsymbol{K} = \begin{bmatrix} 9.75E9 & 0 & 0 & 0 & -7.24E10 & 0 \\ 0 & 9.75E9 & 0 & 7.24E10 & 0 & 0 \\ 0 & 0 & 1E13 & 0 & 0 & 0 \\ 0 & 7.24E10 & 0 & 1.32E12 & 0 & 0 \\ -7.24E10 & 0 & 0 & 0 & 1.32E12 & 0 \\ 0 & 0 & 0 & 0 & 0 & 1E13 \end{bmatrix}$$

The inverse to the above stiffness matrix is the flexibility matrix, which is crucial as it indicates the deflection or rotation for an applied unit of force or moment. Notably, the area contained within the load-deflection hysteresis loops at the seabed corresponds to the energy dissipated by the SSI.

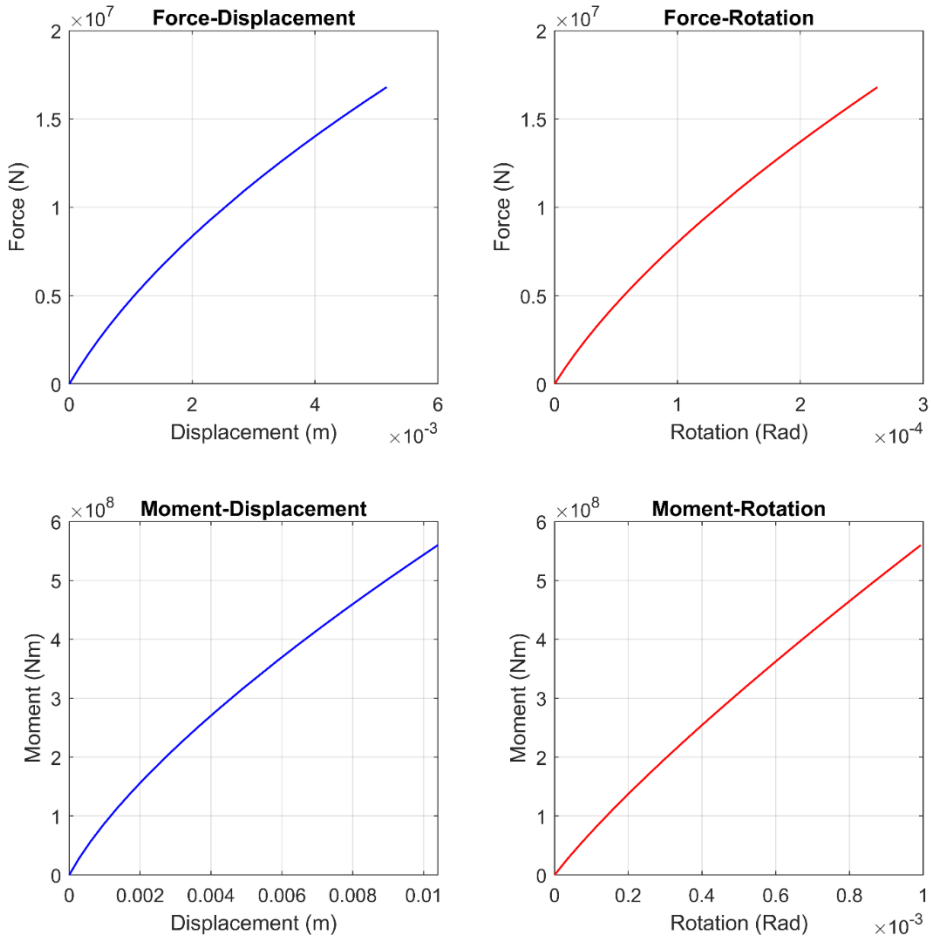

Figure 5. 1. Dense Sand Backbone Curves for Model Calibration.

The above backbone curves used for the calibration of the model in addition to the stiffness matrix are obtained from pushover analyses due to separate application of pure moment (M) and pure lateral force (H) until failure. Peak values of force, moment, displacement (u) and rotation (θ) from these curves will be taken as the values at the ultimate limit state (ULS), these values will be referred to as the referenced values – H_R, M_R, u_R and θ_R for force, moment, displacement, and rotation respectively. The above stiffness matrix and backbone curves properties and characteristics are representations for dense sand with large diameter monopile foundations (9 – 10 m ∅). All analysis done using the novel macro-element model will be based on these calibration input data except stated otherwise.

5.1 Verification of the Macro-Element Model for Cyclic Loading

Model Verification

Model verification is performed for the following load conditions:

- Pure REDWIN monotonic loading in displacement-controlled mode.
- Two cycles of 1-way cyclic loading with & without ratcheting in displacement-controlled mode.
- Two cycles of 2-way cyclic loading with & without ratcheting in displacement-controlled.
- Two cycles of 1-way cyclic loading with & without ratcheting in force-controlled mode.
- Two cycles of 2-way cyclic loading with & without ratcheting in force-controlled mode.

The ratcheting effect can be disabled by setting the initial ratcheting parameter $R_0 = 0$. Disabling the R_0 automatically changes the behavior of the CLAP model to the pure REDWIN model. Figure 5.2 is a pure REDWIN monotonic response comparing the performance of the 0D model to 3D FEA pushover analyses.

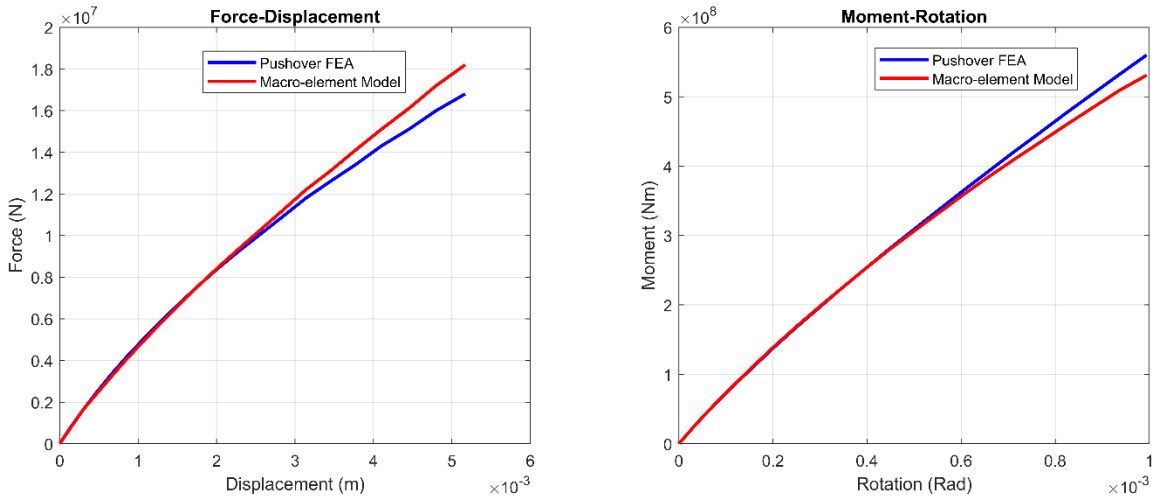

Figure 5. 2. Monotonic Response of the Macro-Element Model Compared to 3D FEA (Displacement-Controlled).

Displacement-Controlled Cyclic Response

The observed response in the performance of the macro-element model indicates satisfactory performance overall. At the first 50 % of the reference values, the model matches closely with the 3D FEA results, except for much higher load levels where there is acceptable performance divergence with the model overestimating the response for the $H - u$ curves and underestimating the response for the $M - \theta$ curves. Physical interpretation of the divergence at a very high load level can be due to the approximation of the 3D foundation behavior to 0D at the location at mudline/seabed, as well as the approximation of the elliptical yield surface geometry to circular yield surface in the model implementation.

Peak lateral force in 3D FEA and macro-element models are 16.80 MN and 18.23 MN respectively, while peak moments are 560.1 MNm and 532.8 MNm respectively.

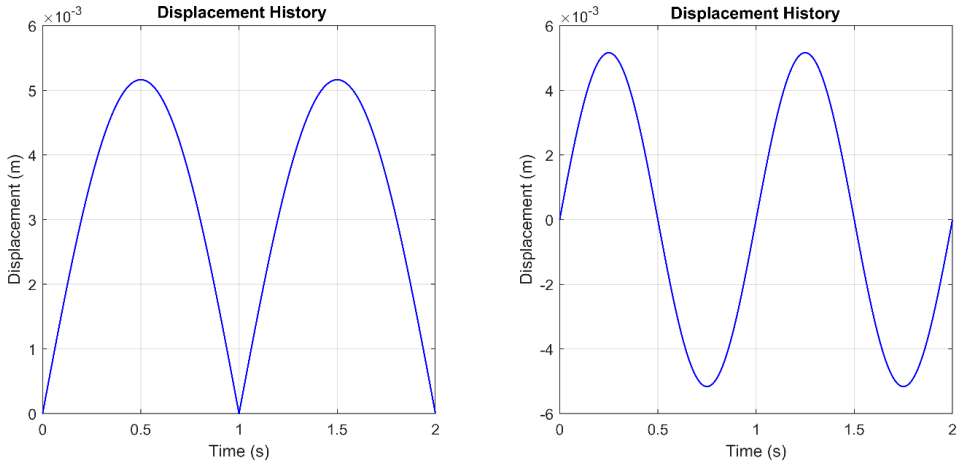

Figure 5. 3. One-way (Left) and Two-way (Right) Sinusoidal Displacement Signals.

In displacement-controlled mode, both displacement and rotation due to pure lateral force from the 3D FEA pushover analyses data are applied up to the peak/reference values u_R and θ_R. The same could be done for pure moment load, but the focus here is on the applied loads (u and θ) due to pure lateral force.

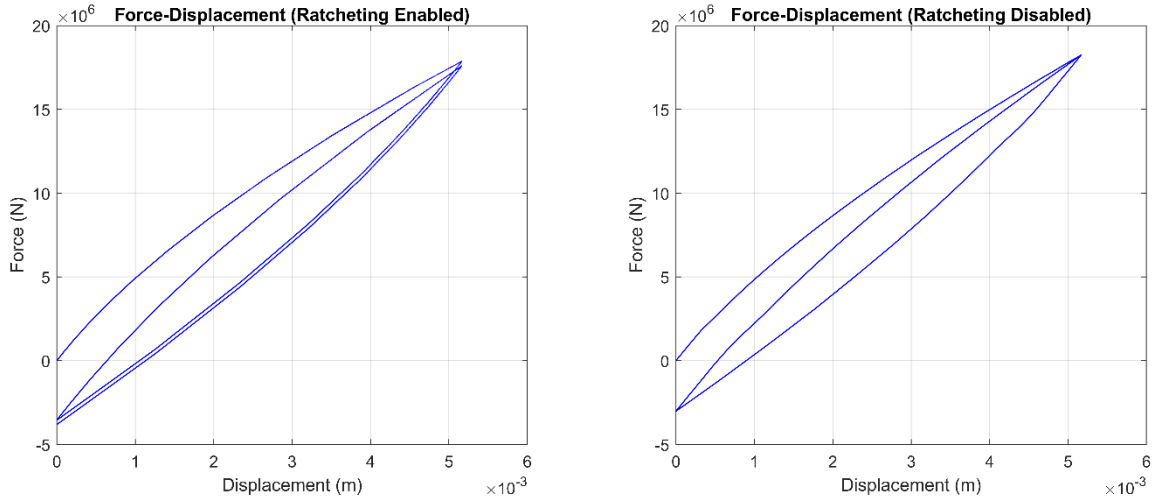

Figure 5. 4. Two Cycles of 1-Way Cyclic Loading With & Without Ratcheting (Displacement-Controlled).

The hysteresis loop is fully closed and not fully closed when ratcheting is disabled and enabled respectively.

Response to two sinusoidal cycles of 1-way loading (cyclic tension) with ratcheting enabled and disabled in Figure 5.4 indicates that while the peak displacement response remained unchanged in the displacement-controlled mode, there is a decrease in secant stiffness for the case with enabled ratcheting compared to the case with ratcheting disabled. This is observed by the decrease in peak force i.e. 17.87 MN ($R_0 \neq 0$) and 18.23 MN ($R_0 = 0$). Ratcheting increases numerical complexity and instability, thus, distortions in the original backbone curve are common. Such an undesirable effect will be rectified in the subsequent sections.

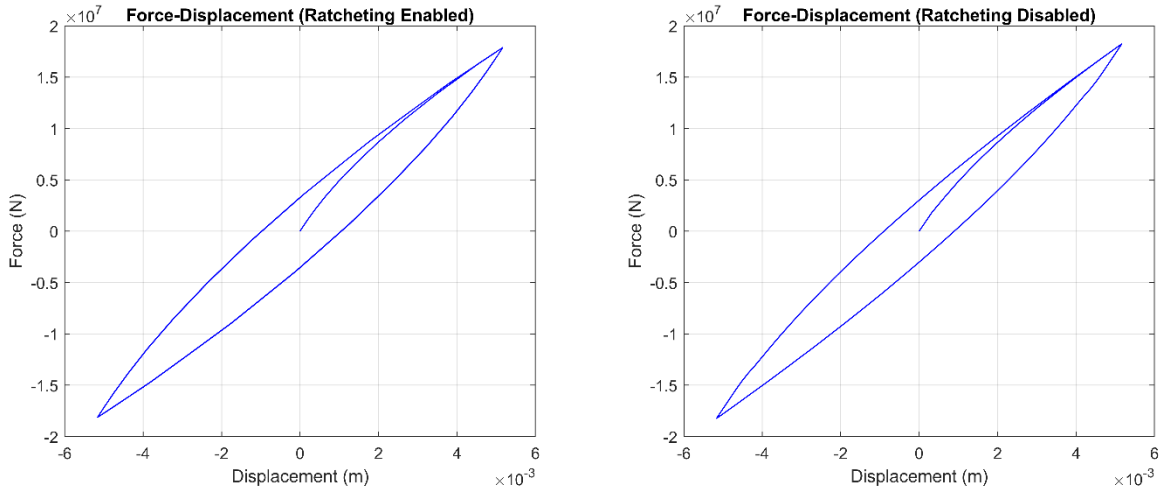

Figure 5. 5. Two Cycles of 2-Way Cyclic Loading With & Without Ratcheting (Displacement-Controlled).

Similar to the 1-way behavior, the 2-way response in Figure 5.5 results in decreased secant stiffness with ratcheting enabled ($H = 17.88$ MN) compared to the case with ratcheting disabled ($H = 18.23$ MN). The response shows that the model adheres to Masing rules as the load path tends to rejoin the backbone curve on reloading. Displacement accumulation due to ratcheting is not observed (fully closed hysteresis loop) in the case with $R_0 \neq 0$, because of load symmetry. Displacement accumulation is due to load asymmetric condition hence, common in 1-way cyclic loading.

Force-Controlled Cyclic Response

The model is then subjected to similar loading conditions as Figure 5.3 – 5.5 but in force-controlled mode. The lateral force from the 3D FEA pushover analyses data is applied as a unidirectional load up to the peak/reference values (H_R = 16.8 MN).

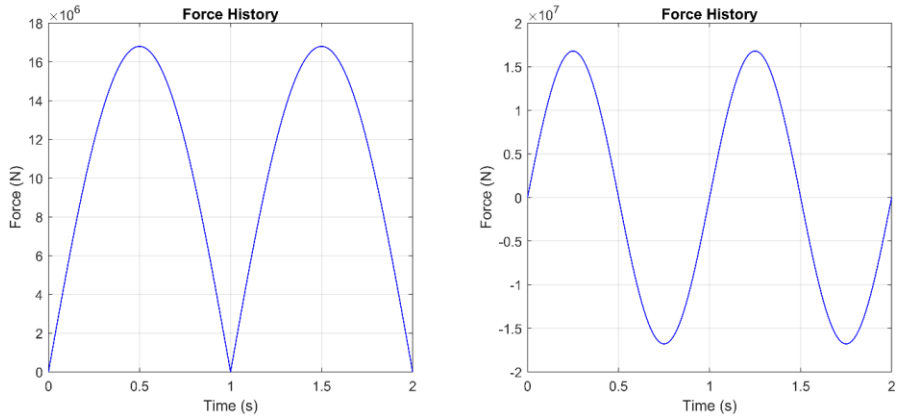

Figure 5. 6. One-way (Left) and Two-way (Right) Sinusoidal Force Signals.

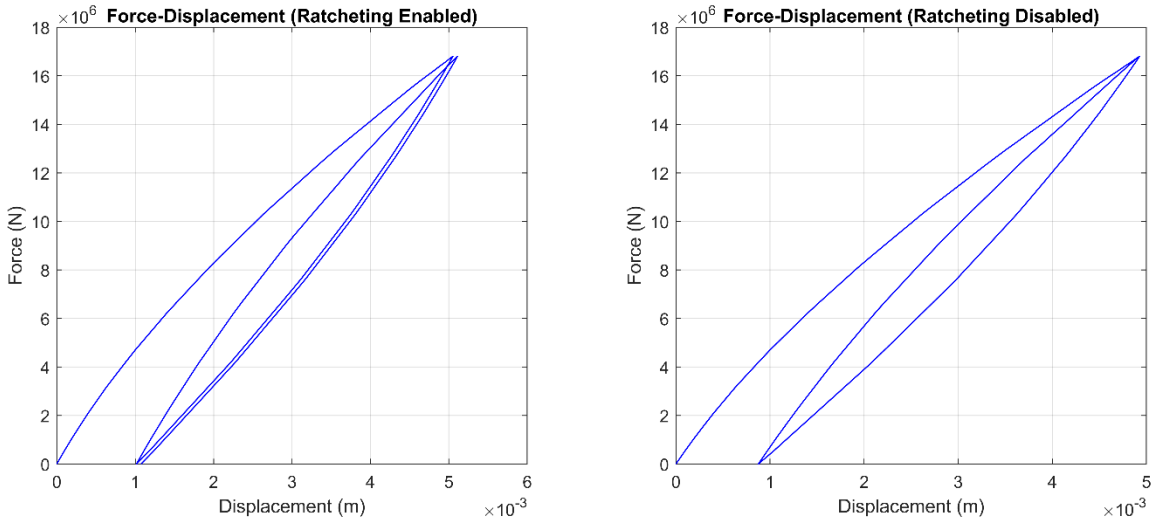

Figure 5. 7. Two Cycles of 1-Way Cyclic Loading With & Without Ratcheting (Force-Controlled).

Unlike the displacement-controlled mode where the peak displacement response is unchanged irrespective of the ratcheting condition while the force varies, in the force-controlled mode, the peak force response remains unchanged irrespective of the ratcheting condition while the displacement varies. However, the principle concerning the secant stiffness behavior in either mode remains unchanged. In Figure 5.7 for 1-way cyclic loading at $R_0 \neq 0$, peak displacement response is higher than the case with $R_0 = 0$. This also signify that ratcheting effect distorts the backbone curve and result in decreased secant stiffness of the backbone curve.

Peak displacement obtained from the 1-way cyclic loading is 0.0051 m ($R_0 \neq 0$) and 0.0049 m ($R_0 = 0$).

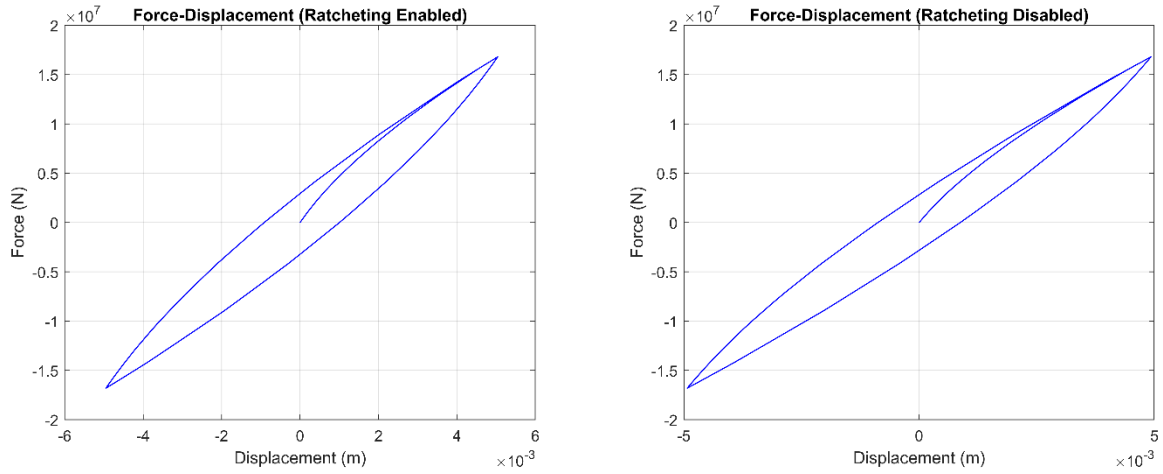

Figure 5. 8. Two Cycles of 2-Way Cyclic Loading With & Without Ratcheting (Force-Controlled).

Likewise, in Figure 5.8 the peak displacement obtained from the 2-way cyclic loading (cyclic tension-compression) is 0.0050 m ($R_0 \neq 0$) and 0.0049 m ($R_0 = 0$).

Typically, in force-controlled/stress-controlled mode, there exists permanent deformation (plastic strain) and internal damping after unloading. But in displacement-controlled/strain-controlled mode, this is represented by the compressive stress (indicating permanent deformation) after unloading since the material does not return to the original state which is zero force and zero displacement.

5.2 Validation based on REDWIN Modelling of Multidirectional Cyclic Loading

REDWIN Validation

Validation of the HARM-REDWIN macro-element model is done considering 3 different load paths according to Page et al. (2019a) namely –

- Radial load path
- Rectangular load path
- Bow tie load path

The elastic stiffness matrix and backbone curves used as input for this specific model calibration are based on clay soil. The elastic foundation stiffness matrix for the macro-element model is given below:

$$\boldsymbol{K} = \begin{bmatrix} 7.40E6 & 0 & 0 & 0 & -5.55E7 & 0 \\ 0 & 7.40E6 & 0 & 5.55E7 & 0 & 0 \\ 0 & 0 & 1E6 & 0 & 0 & 0 \\ 0 & 5.57E7 & 0 & 9.10E8 & 0 & 0 \\ -5.57E7 & 0 & 0 & 0 & 9.10E8 & 0 \\ 0 & 0 & 0 & 0 & 0 & 1E6 \end{bmatrix}$$

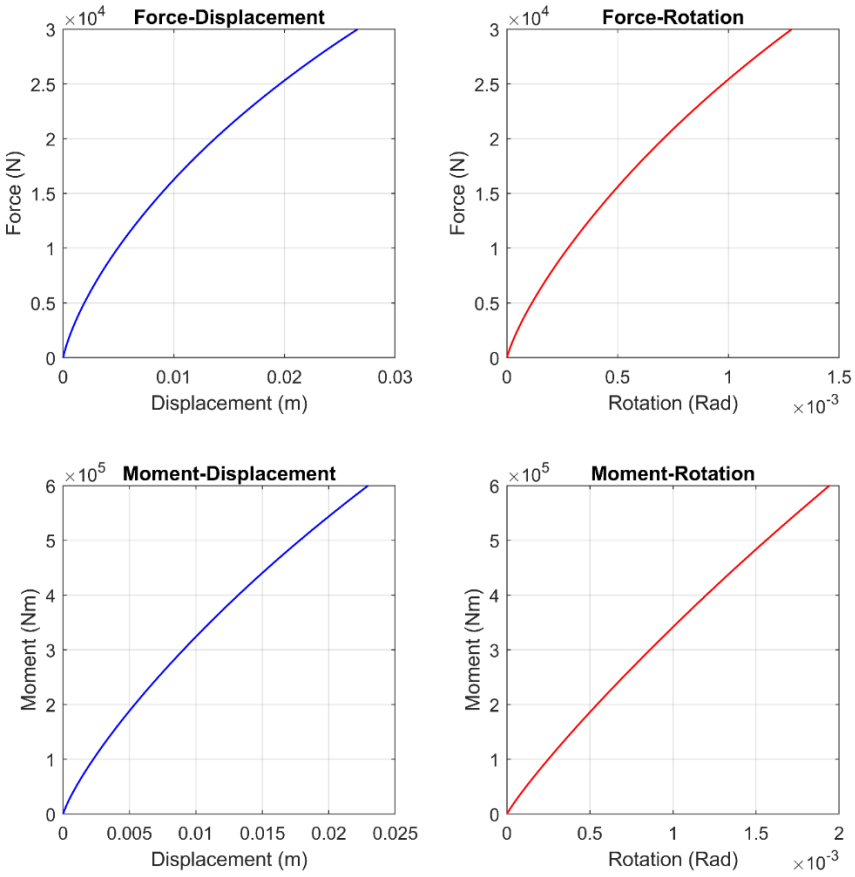

Figure 5. 9. Clay Backbone Curves for Model Calibration.

These backbone curves are obtained from pushover analyses in distinct phases. The first phase is the application of pure moment load (M) i.e. zero lateral force (H) until failure. The output of this phase is translational displacement and rotation due to the applied moment. Similarly, the second phase is the application of pure lateral force load (H) i.e. zero moment (M) until failure. The output of this phase is translational displacement and rotation due to applied lateral force. The above stiffness matrix and backbone curves properties and characteristics are representation for a clay with large monopile diameter monopile foundation of 9.0 m, and embedder length to diameter ratio L/D is 4. The global stiffness and capacity of the monopile foundation is quite very much lower compared to the case with dense sand presented earlier.

Radial Load Path

Monotonic radial loads are applied to the foundation with a peak lateral force of 10 kN in H_y component and peak moment of 300 kNm in M_y component. Here, 5 different monotonic load paths with different orientations with respect to the horizontal i.e. 0°, 30°, 60°, 75°, and 90° are considered as shown in Figure 5.10. Equal length is selected for each monotonic path for fair comparison.

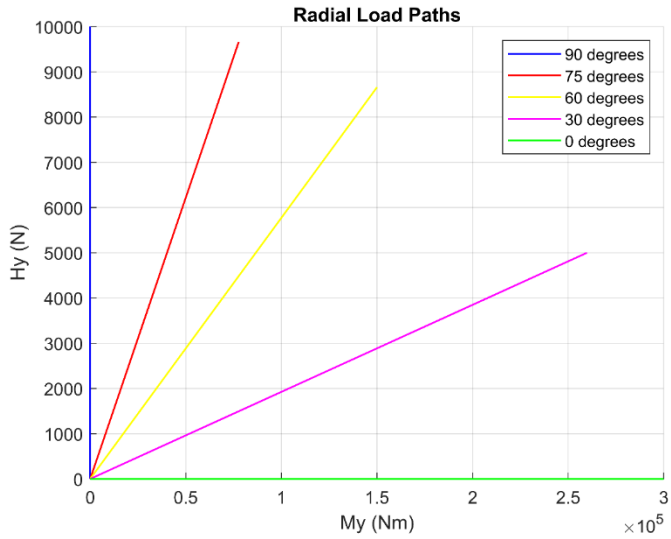

Figure 5. 10. Radial Load Path.

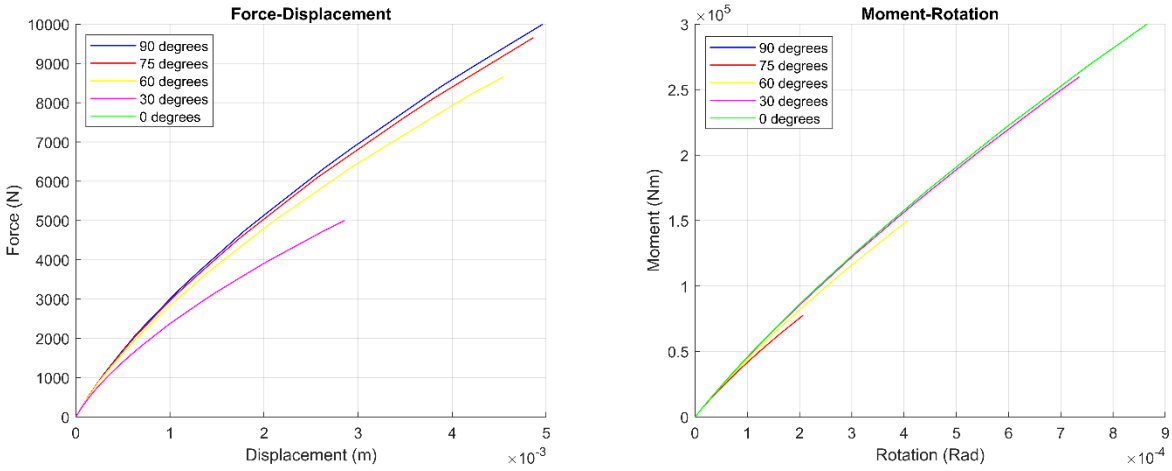

Figure 5. 11. Radial Load Response.

In the force-displacement ($H_y - u_y$) response, peak displacement for each monotonic path decreases with decreasing orientation i.e. from 90° to 0°. The response at 0° vanished since the trigonometric sine of 0° is zero. Likewise, the secant stiffness followed the same pattern in decreasing order. Meanwhile, the opposite behavior is observed for the moment-rotation ($M_y - \theta_y$) response where peak rotation for each monotonic path is in descending order from 0° to 90°, the same also is the secant stiffness. The response at 90° vanished since the trigonometric cosine of 90° is zero.

Rectangular Load Path

A square load path is applied in the clockwise direction, with peak lateral forces of 10 kN each in H_y and H_x components.

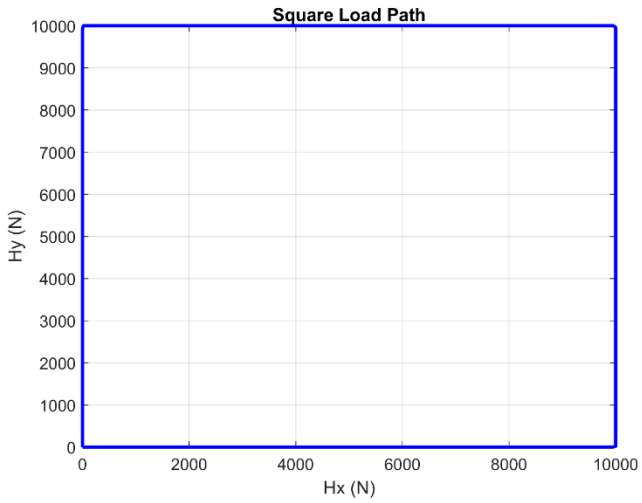

Figure 5. 12. Rectangular Load Path.

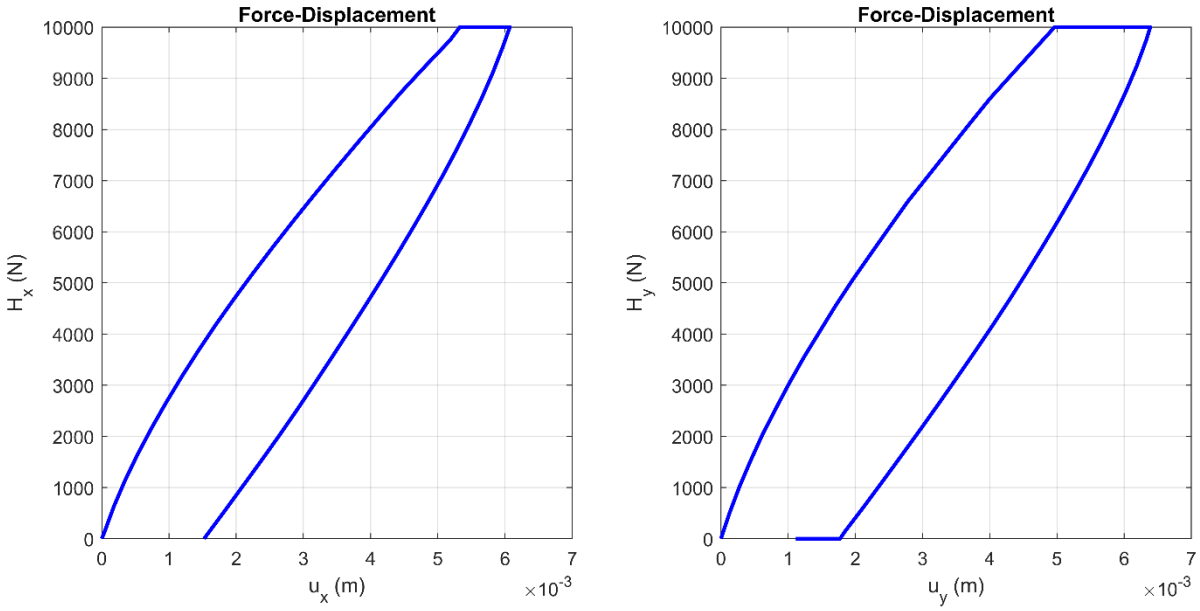

Figure 5. 13. Rectangular Load Response.

Figure 5.13 indicates that the model can reproduce a response to a multidirectional load path. With every change in load path direction, the initial displacement response is observed to be parallel to the load path. This behavior at the transition in the load path shows that the foundation exhibits stable, elastic behavior momentarily i.e. the foundations behave elastically and uncoupled at these transitions. The residual deformation is 0.001522 m and 0.001114 m at u_x and u_y respectively.

Bow-Tie Load Path

The bow-tie load path shows a distinctive pattern that corresponds to alternating load directions. The bow-tie load path is applied in the clockwise direction, with a peak lateral force of 10 kN in H_y component and peak moment of 100 kNm in M_y component.

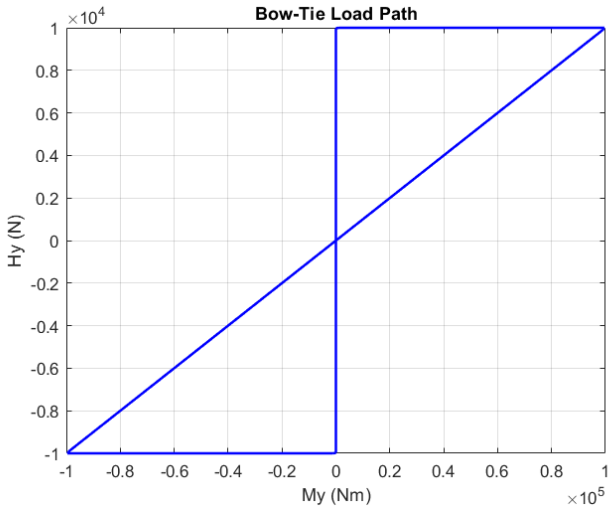

Figure 5. 14. Bow Tie Load Path.

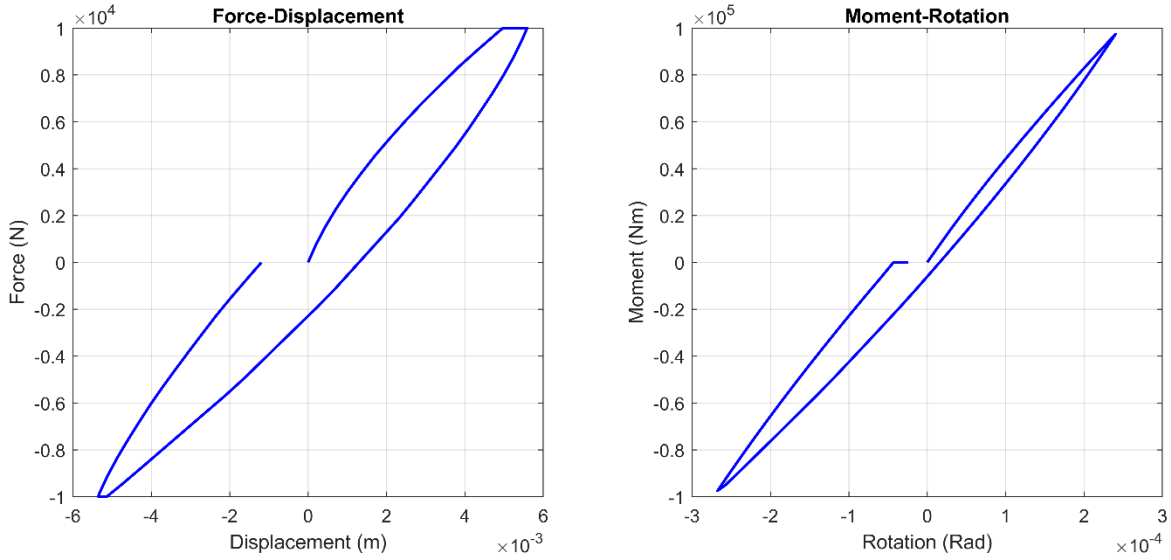

Figure 5. 15. Bow Tie Load Response.

The response in force-displacement ($H_y - u_y$) and moment-rotation ($M_y - \theta_y$) are identical to the results by Page et al. (2019). The hysteresis loops observed in the bow-tie load response imply energy dissipation characteristic of inelastic behavior or damping within the foundation or soil-monopile interaction. The foundation experiences loading and unloading, with some residual deformation (– 0.001191 m) and rotation (– 0.00002411 rad or – 0.0014°).

Unlike the square load path, the bow-tie load path introduces a more complex and continuous coupled multidirectional loading with complex interactions between lateral displacements and rotations.

5.3 Verification based on HARM Modelling of Unidirectional Cyclic Loading

HARM Verification

The model is subjected to unidirectional loads. The simulations are performed to verify the HARM implementation and integration into the macro-element model. Generally, HARM is a force-controlled model, therefore, simulations performed under this section are mostly in force-controlled mode. The following are presented:

- Monotonic loading in displacement- and force-controlled modes coupled with ratcheting distortion correction.
- One-way cyclic loading of single amplitude at 20 cycles and 100 cycles, with and without acceleration.
- One-way cyclic loading of multiple amplitudes, up to 3 levels with monotonic loading and unloading at the end.

Monotonic Loads

Correction of the ratcheting distortion of the backbone curve typically requires manual adjustment and optimization of calibration parameters for HARM especially optimizing the hardening modulus H_n to fit experimental data and also the ratcheting parameters. This approach is not sustainable and will require modification when the condition of the experiment and loading changes.

Assuming force-controlled mode, ratcheting distortion can be rectified in an automated and efficient way by the distortion correction factor ($\boldsymbol{\kappa}$). Below is a pseudo-code showing the impact of $\boldsymbol{\kappa}$ in regulating R_0 based on certain conditions which ensures no distortion of the backbone curve at any point in a cyclic load.

$$\boldsymbol{\kappa} = 0 \Longrightarrow \text{Initialize } \boldsymbol{\kappa}$$

$$\boldsymbol{\kappa} = \max\left(|\sigma|, \boldsymbol{\kappa}\right)$$

$$\begin{cases} \text{if} & \sigma < \boldsymbol{\kappa} \quad \Longrightarrow R_0 \neq 0 \\ \text{else} & \sigma \geq \boldsymbol{\kappa} \quad \Longrightarrow R_0 = 0 \\ \text{end} & \text{Update } \boldsymbol{\kappa} \end{cases}$$

Maximum value of $\boldsymbol{\kappa}$ is the peak force at any load cycle. In displacement-controlled mode, stress/force (σ) is replaced by strain/displacement (ϵ). Figure 5.16 below shows monotonic load under 3 states – with ratcheting disabled, enabled but without $\boldsymbol{\kappa}$ and enabled with $\boldsymbol{\kappa}$ activated. The backbone curve with $\boldsymbol{\kappa}$ activated effectively corrects ratcheting distortion, and it applies to any loading condition.

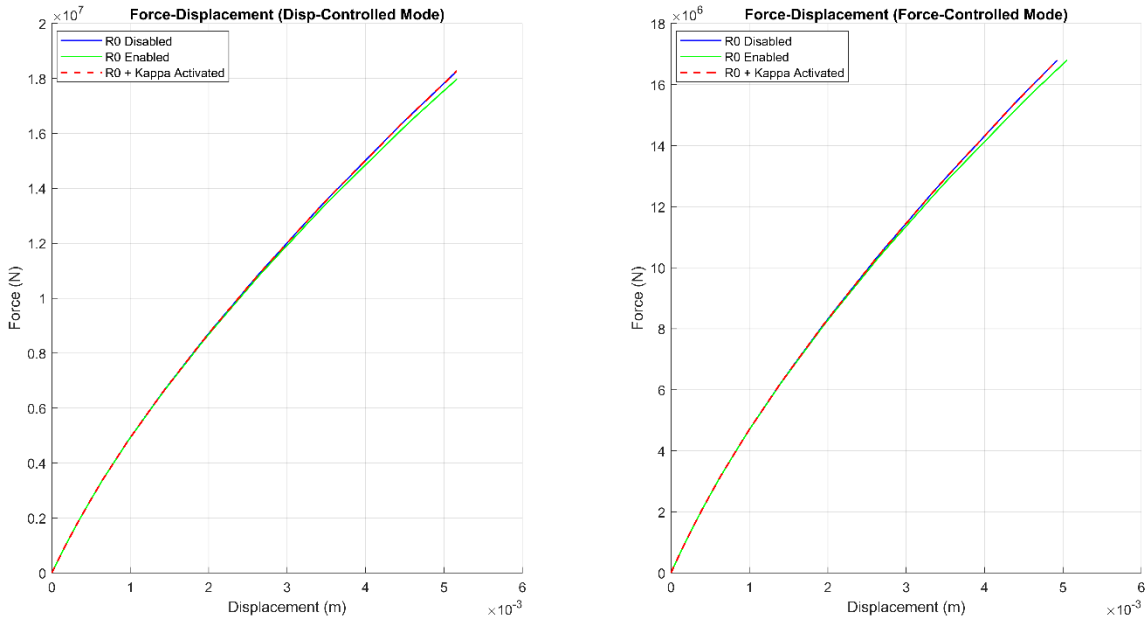

Figure 5. 16. Monotonic Response Showing Effect of Backbone Curve Distortion due to Ratcheting.

Single Amplitude Cyclic Load

Figure 5.17 shows 1-way cyclic loading of single amplitude at 20 cycles and 100 cycles, with and without acceleration i.e. cycle-by-cycle. The default equation of the ratcheting parameter R_n defining the rate of ratcheting is based on cycle-by-cycle response. To accelerate the simulation without loss of accuracy, R_n is further multiplied by an acceleration

factor R_{fac}. The R_{fac} represents the number of cycles to be skipped. This comes in very handy when assessing long-term cyclic loading i.e. over 1×10^5 cycles.

$$R_n = R_{\text{fac}}.R_0\left(\frac{k_n}{k_U}\right)\left(\frac{\beta}{\beta_0}\right)^{-m_r}\left(\frac{|\sigma|}{k_U}\right)^{m_s}$$

Simple implementation of the R_{fac} for 20 and 100 cycles of cyclic load is presented. Table 5.2 shows the acceleration scheme setup.

Table 5. 2. Acceleration Scheme for 1-Way Cyclic Loading.

20 Cycles of Cyclic Load			
Cycle-by-Cycle Scheme		**Acceleration Scheme**	
Number of Cycles	R_{fac}	Number of Cycles	R_{fac}
2	1	2	1
16	1	1	16
2	1	2	1
20 Cycles Computed		5 Cycles Computed	
100 Cycles of Cyclic Load			
Cycle-by-Cycle Scheme		**Acceleration Scheme**	
Number of Cycles	R_{fac}	Number of Cycles	R_{fac}
2	1	2	1
7	1	1	7
2	1	2	1
88	1	1	88
1	1	1	1
100 Cycles Computed		7 Cycles Computed	

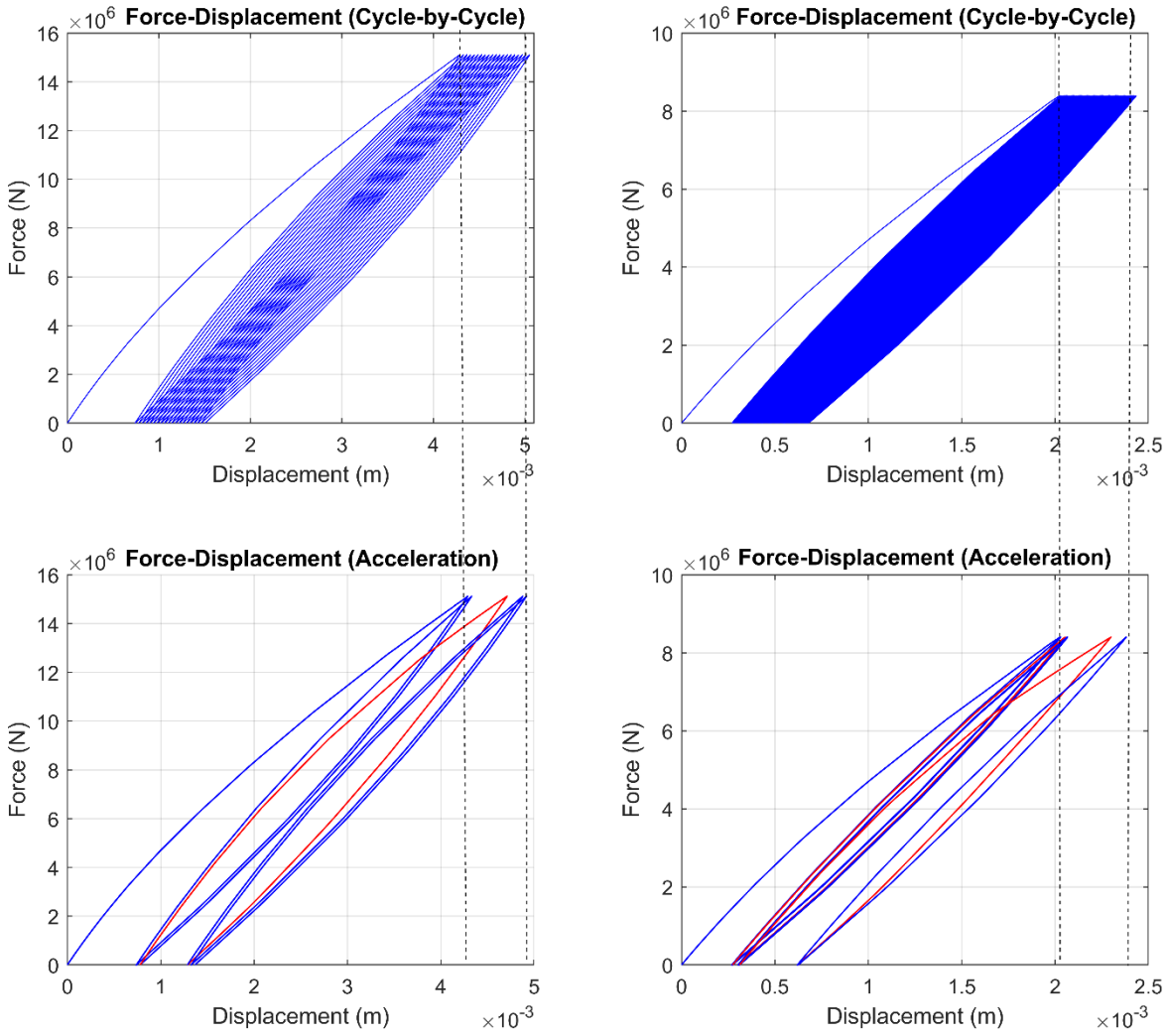

Figure 5. 17. 1-Way Cyclic Loading of Single Amplitude – 20 Cycles (Left) & 100 Cycles (Right).

Peak lateral force for 20 and 100 cycles simulations is set to H_R and $0.5H_R$ respectively. Figure 5.17 above indicates a good approximation of the acceleration scheme to the cycle-to-cycle approach. The accuracy of the acceleration scheme can be further improved by adjusting the ratcheting parameters.

Multi-Amplitude Cyclic Load

Figure 5.18 and Figure 5.19 show the 1-way multi-amplitude cyclic loading at 3 levels followed by monotonic loading and unloading for a total of 20 cycles – with and without ratcheting. The cyclic load is divided into 10 cycles for the first load level, 5 cycles for the second load level, 5 cycles for the third load level, and a cycle for the final level. Peak lateral force for the first, second, third, and the final level is set to $0.4H_R$, $0.55H_R$, $0.75H_R$ and $0.9H_R$ respectively.

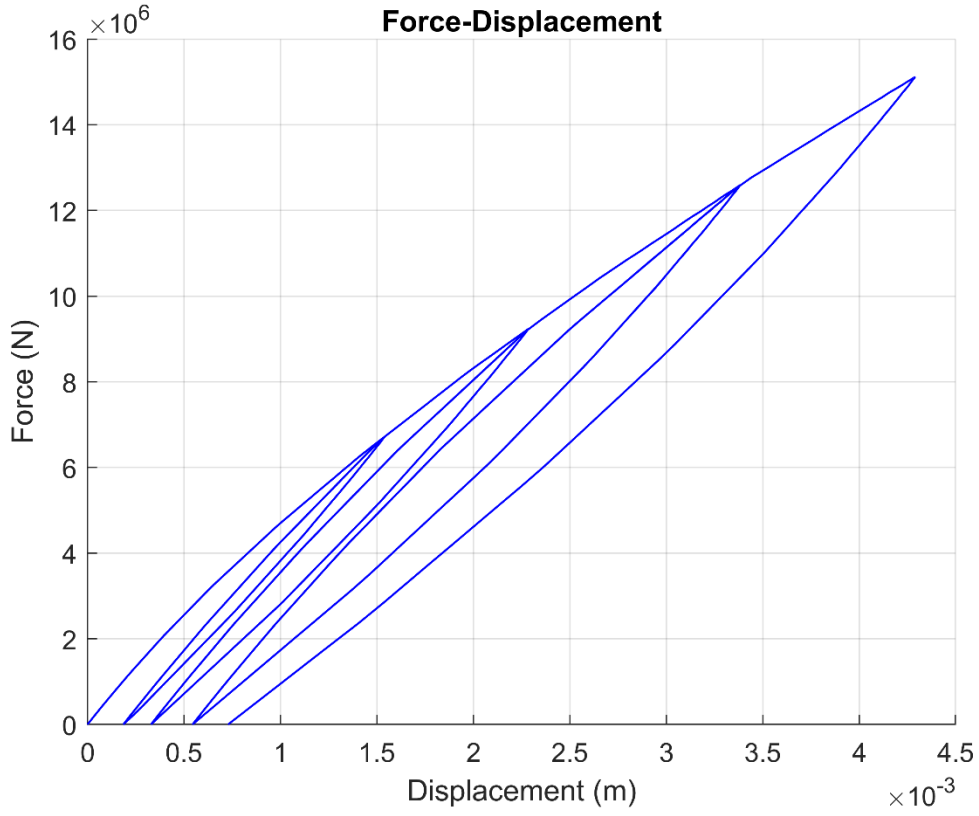

Figure 5. 18. 1-Way Cyclic Loading of Multiple Amplitudes with Ratcheting Disabled.

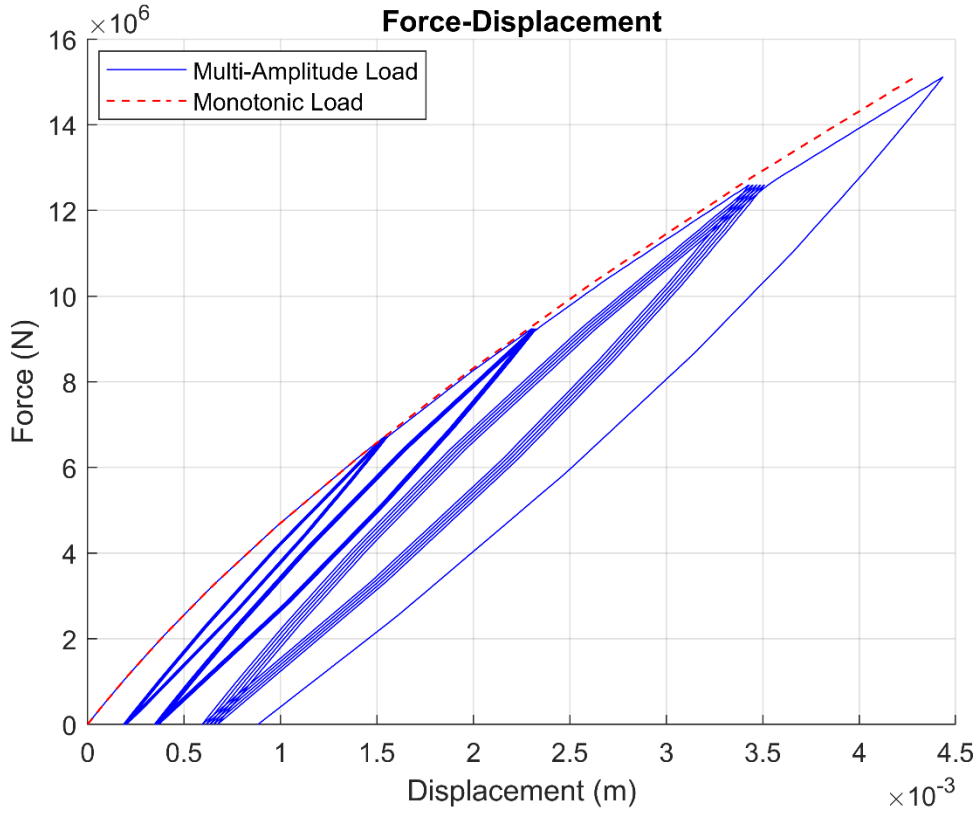

Figure 5. 19. 1-Way Cyclic Loading of Multiple Amplitudes with Ratcheting Enabled.

Figure 5.18 is without ratcheting, hence, the hysteresis loop is fully closed after each load level, while Figure 5.19 shows displacement accumulation due to ratcheting. Final residual deformation is 0.0007285 m and 0.0008829 m for $R_0 = 0$ and $R_0 \neq 0$ respectively. Likewise, peak total displacement is 0.0043 m and 0.0044 m for $R_0 = 0$ and $R_0 \neq 0$ respectively. Peak total displacement at monotonic load 0.00429 m indicates the same total response in the case where ratcheting is disabled.

Figure 5.19 shows that higher load amplitude increases the rate of ratcheting; ratcheting tends to move the response away from the monotonic curve; with each reloading at higher amplitude, the response tends to rejoin the monotonic curve and follow the same slope as the monotonic curve. This shows that the model obeys extended Masing rules even after cyclic loading.

5.4 Verification of Centrifuge Test Unidirectional Cyclic Loading

Experimental Verification

The macro-element model is subjected to two different kinds of 1-way cyclic loadings. The loading signals are based on the well-researched experiments of Rosquoët (Rosquoët, 2004). The first load signal is the P32 test which is a single pile unidirectional centrifuge experiment including static horizontal load (monotonic) at the initial stage followed by 1-way cyclic loads (12 cycles). The nature of the cyclic load is cyclic triangular loads having a maximum value of 960 kN and minimum value of 480 kN conducted with vertical monopile (0.72 m ∅) embedded in dry dense sand (Fontainebleau sand). The second signal is the P344 test with the same maximum load value but zero minimum value. Figure 5.20 reproduced the required signals. However, the bottom low-frequency signal (0.333 Hz) is the desired time history, though the high-frequency signal (1 Hz) has been included to verify if loading signal frequency influences the response of the macro-element model.

The purpose here is not to conduct an exact model-to-experiment comparison as this will require running 3D FEA simulations calibrated with the exact soil properties and pile geometric characteristics as the experiment data, then extraction of the stiffness matrix characteristic of the soil-pile interaction and the backbones curves to be used to recalibrate the macro-element model to fit the experimental data. This is beyond the scope of this study.

Considering that the macro-element model used in this study is calibrated based on dense sand as well, a global response study can be made to assess the macro-element performance via normalization of data. The normalization approach is based on the normalized lateral load and displacement relations below;

$$\bar{H} = \frac{H}{H_{max}}$$

$$\bar{u} = \frac{u}{u_{50}}$$

This indicates normalized force value ($\bar{H}$) is with respect to the peak load or reference load, while the normalized displacement value $\bar{u}$ is with respect to the displacement at 50 % of the monotonic force response. The macro-element model is subjected to unidirectional load at the full reference lateral force H_{max} (16.8 MN), thus for the P32 load signal, this will be 16.8 MN maximum and 8.4 MN minimum, while for the P344 signal, this will be the same but with zero minimum value.

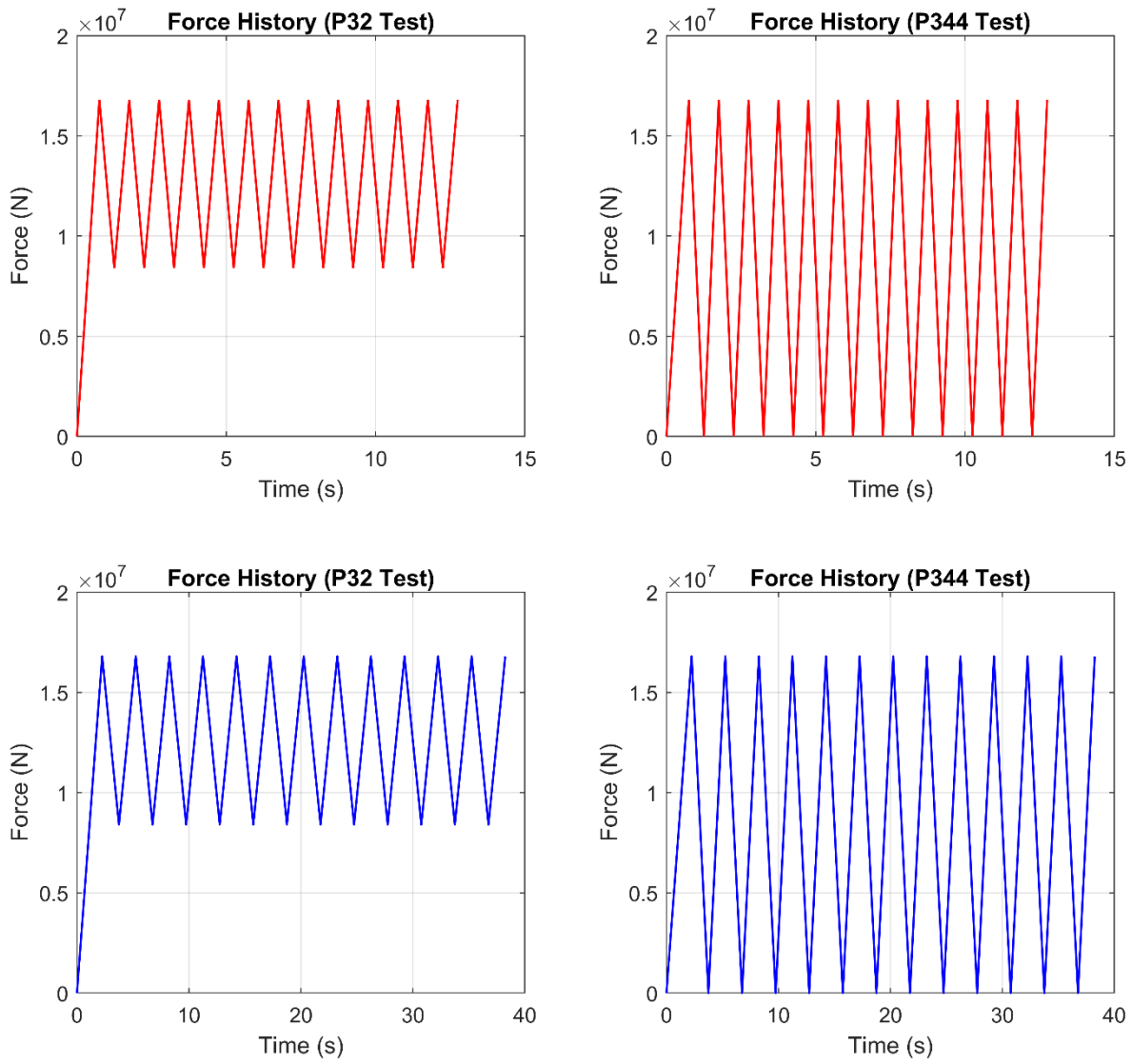

Figure 5. 20. Time History of P32 Test and P344 Test at High Frequency (Top) and Low Frequency (Bottom).

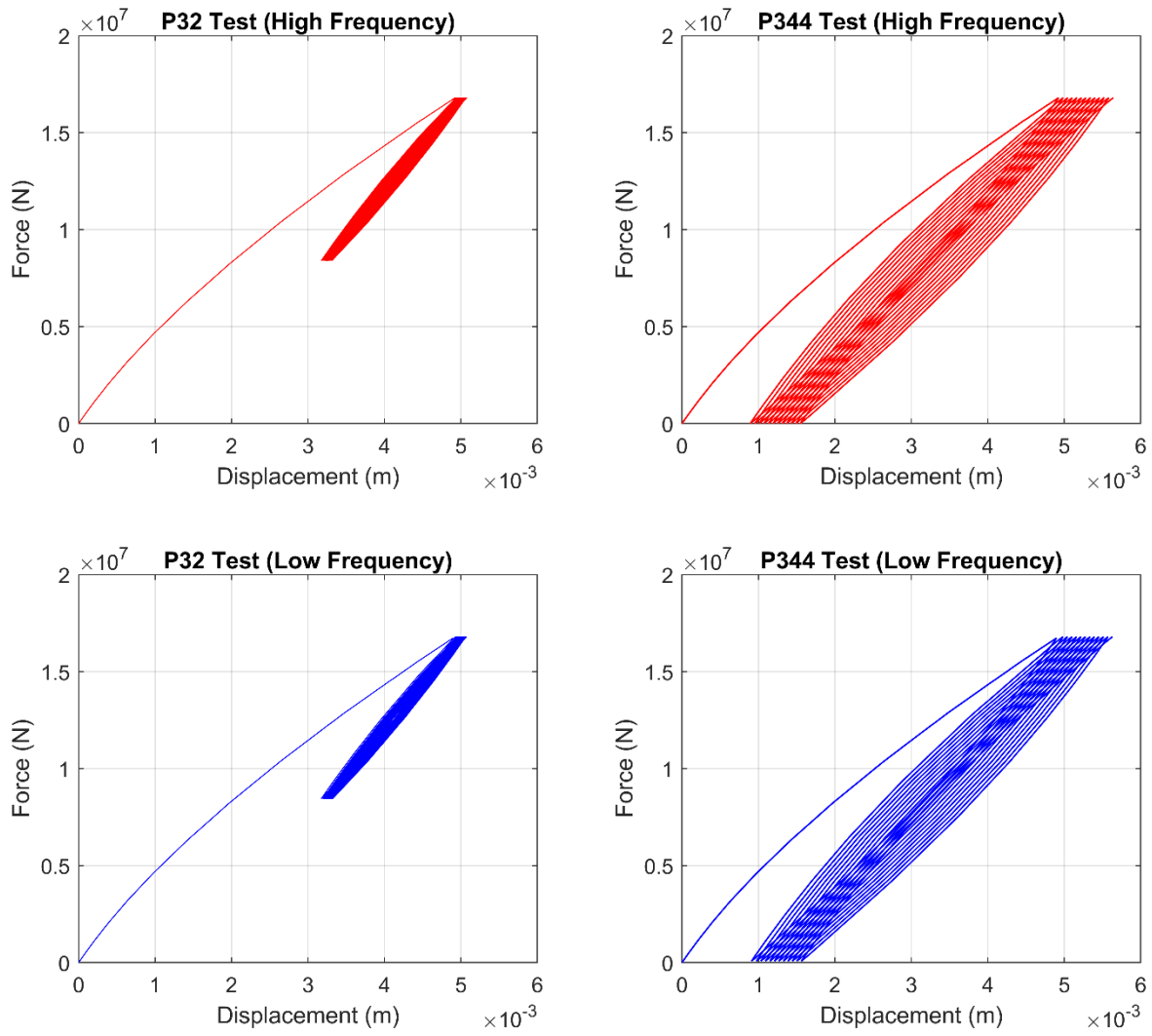

Figure 5. 21. P32 Test and P344 Test Monotonic + Cyclic Response at High Frequency (Top) and Low Frequency (Bottom).

The obtained response indicates insignificant difference in the response at high-frequency signal versus the low-frequency signal. For assessment of the model's global response, the normalization data are presented in Table 5.3 below.

Table 5. 3. Normalization Data for Macro-Element Model and Experiment.

	P32 Model	**P344 Model**	**P32 Experiment**	**P344 Experiment**
H_{max} **(N)**	16800000	16800000	960000	960000
u_{50} **(m)**	0.0020264	0.0020264	0.062577778	0.064044444

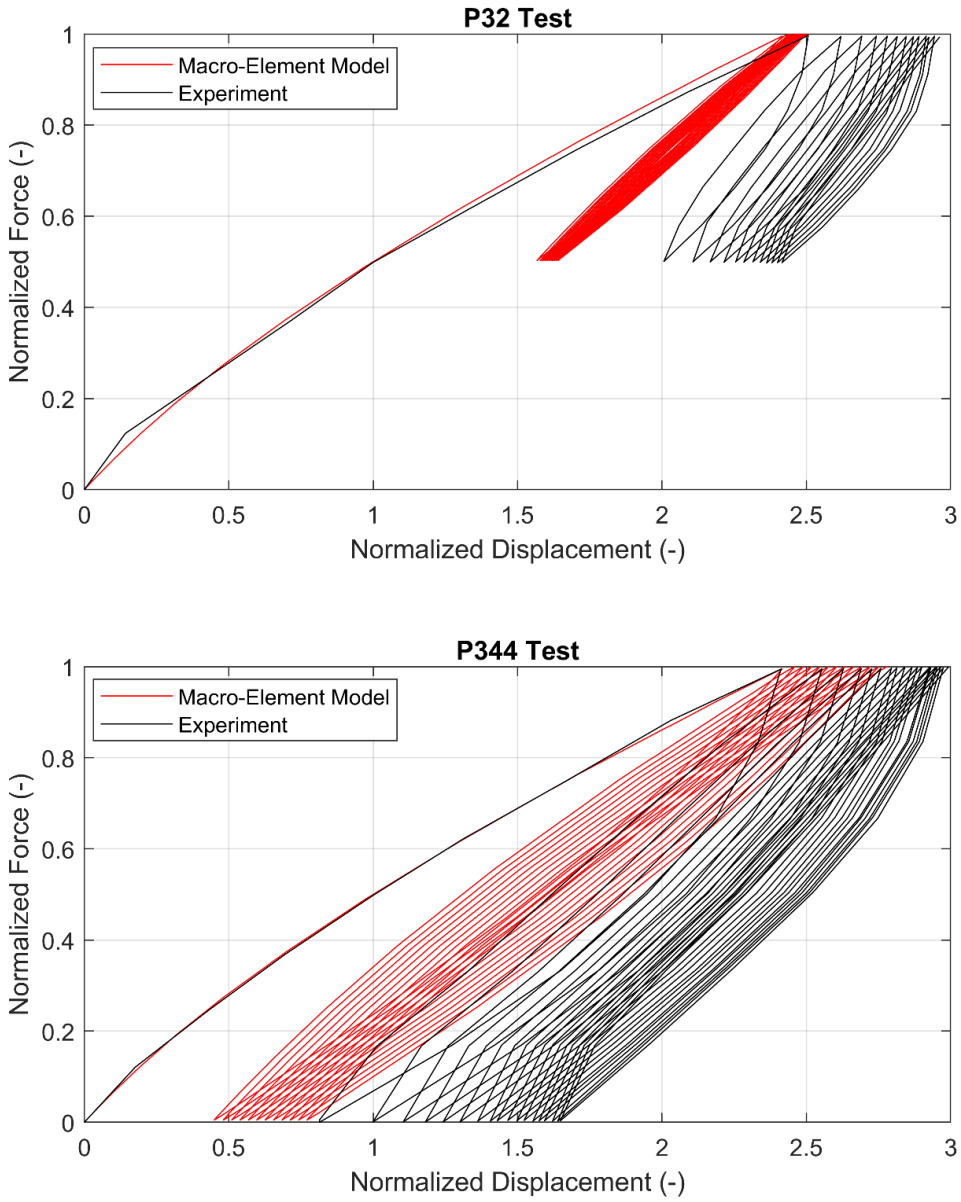

Figure 5. 22. Global Response Comparison of the Macro-Element Model to Centrifuge Tests for P32 and P344.

The source of the experiment data is from archived centrifuge experiment spreadsheet files of Rosquoët (Rosquoët, 2004). The outcome of Figure 5.22 showed that the macro-element model matches very closely to the experiment backbone curves for the P32 and P344 tests. Major discrepancies between the model and the experiment are in the accumulated response. Improvement in this response aspect can be made by modifying the ratcheting parameters. Tuning the ratcheting parameters to match the desired output is necessary depending on the soil-pile interaction characteristics.

Note that the experiment applies the forces as well as computes the displacements at the pile head. The location of the pile head above ground level is 1.6 m. The macro-element model focuses on computing force-displacement response lumped at a critical point/location in the structure which is at the ground level (seabed/mudline level) as this is the location where the reaction forces and moments are computed, and lateral resistance from the soil begins coupled with the presence of significant bending moments and shear forces.

6. MODELLING OF MULTIDIRECTIONAL CYCLIC LOADING

This section presents some examples on multidirectional cyclic loading including simple cases as the spiral loads, as well as complex cases having high degree of randomness like the earthquake load and short storm-type load.

6.1 Simple Cases of Multidirectional Cyclic Loading

6.1.1 Spiral Load Cases

The spiral load is a specific type of cyclic loading. Two kinds of spiral loads are presented in this section. Both spiral load types exhibit increasing load magnitude, where the load direction rotates while the magnitude increases with each cycle. The first is spiral load with a constant magnitude of load increment with each cycle while the second is with geometrically increasing magnitude with each cycle.

The two spiral load types could provide valuable insights into the monopile foundation's response under multidirectional and escalating loads. While not entirely realistic, these loads serve as important tools in research to evaluate the foundation's behavior under challenging conditions. The constant increment load path can offer a controlled and steady-state assessment and can be easily predictable, while the geometrical increment load path could test the foundation's ability to withstand rapidly increasing and potentially highly nonlinear forces. The latter is less predictable. The total load cycles considered in each case is 4.

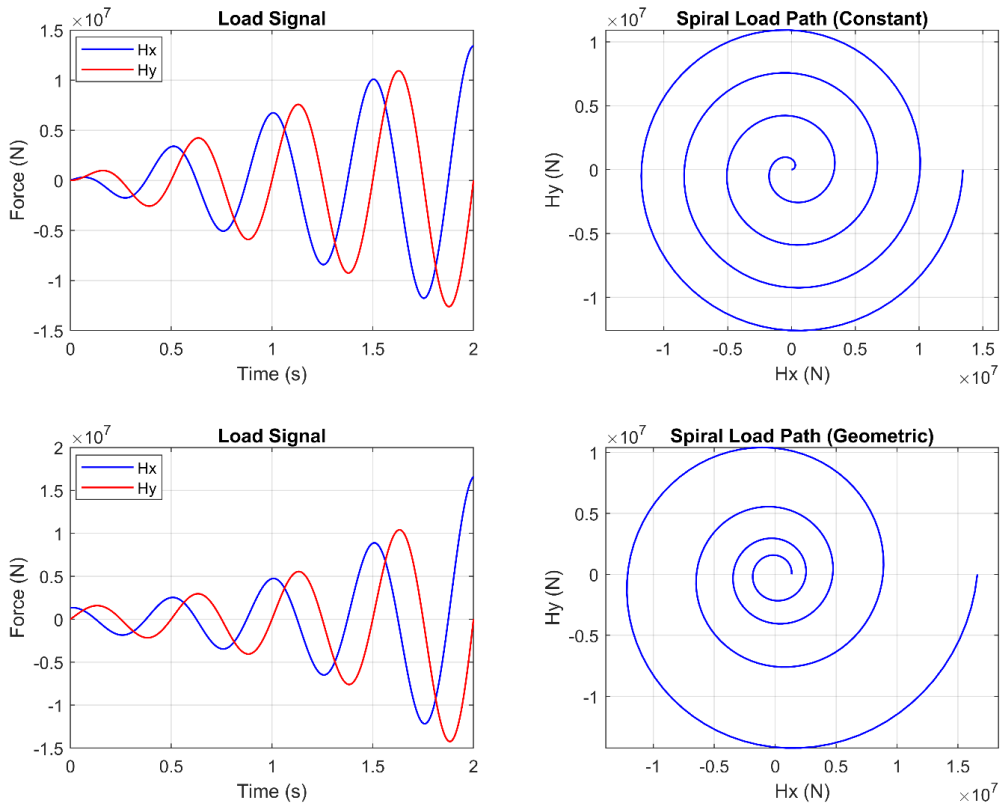

Figure 6. 1. Spiral Load Path with Constant Cyclic Increment Rate (Top) and Geometrical Cyclic Increment Rate (Bottom).

The geometrical increment case has increasingly varying increments with each increment in the cycle number. The constant increment rate implies a uniform and predictable increase in load magnitude with each cycle. This could be analogous to a steady-state increase in environmental forces, such as a gradually intensifying storm; but the geometrically

increasing increment could lead to a more aggressive and rapidly intensifying load scenario. This would result in a load path that is less predictable and more challenging for the foundation to resist.

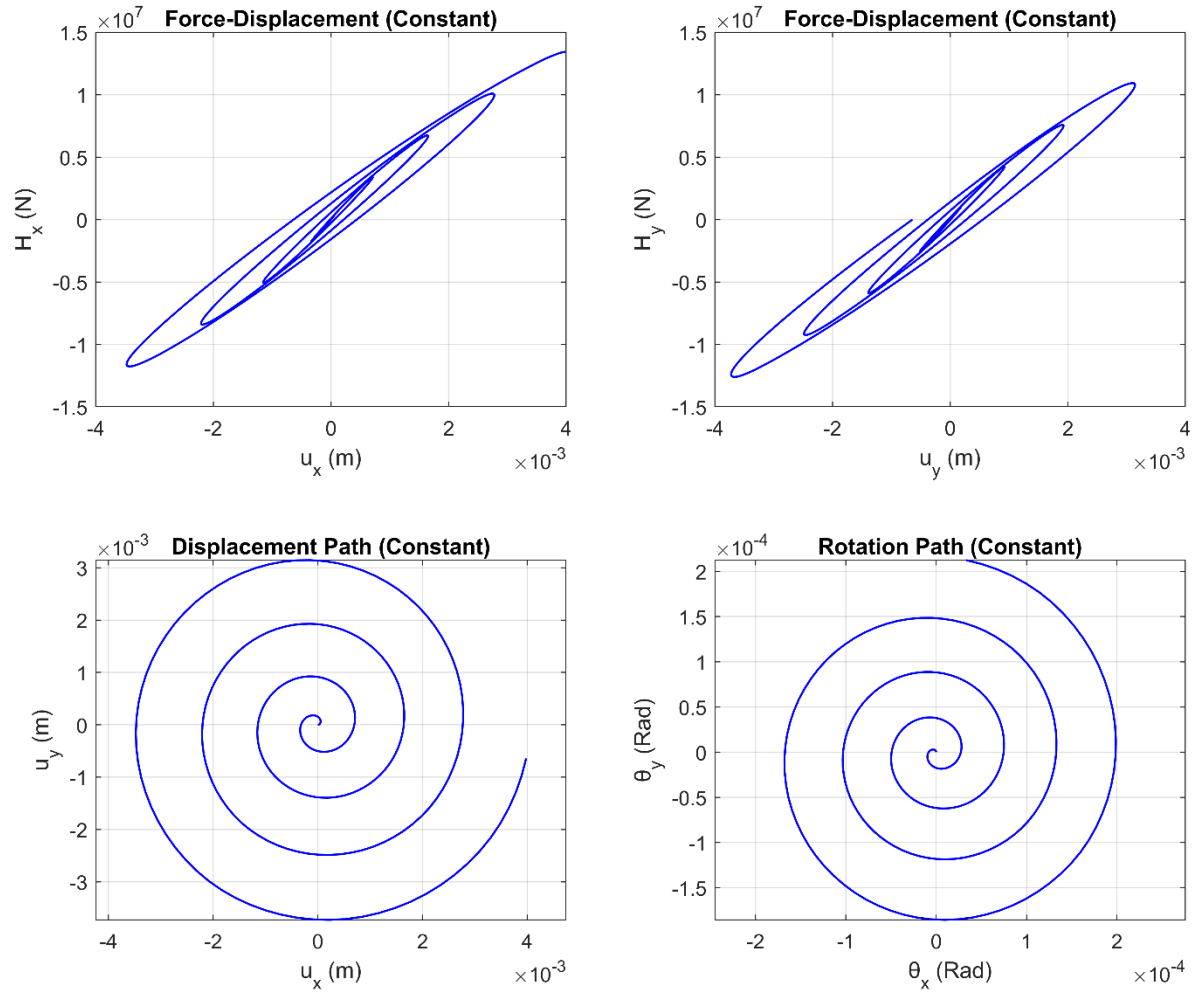

Figure 6. 2. Spiral Load Response with Constant Cyclic Increment Rate.

The response in Figure 6.2 shows a consistent pattern of deformation and stress distribution, with hysteresis loops. The hysteresis loops reflect energy dissipation during each cycle, indicating the damping characteristics of the monopile foundation.

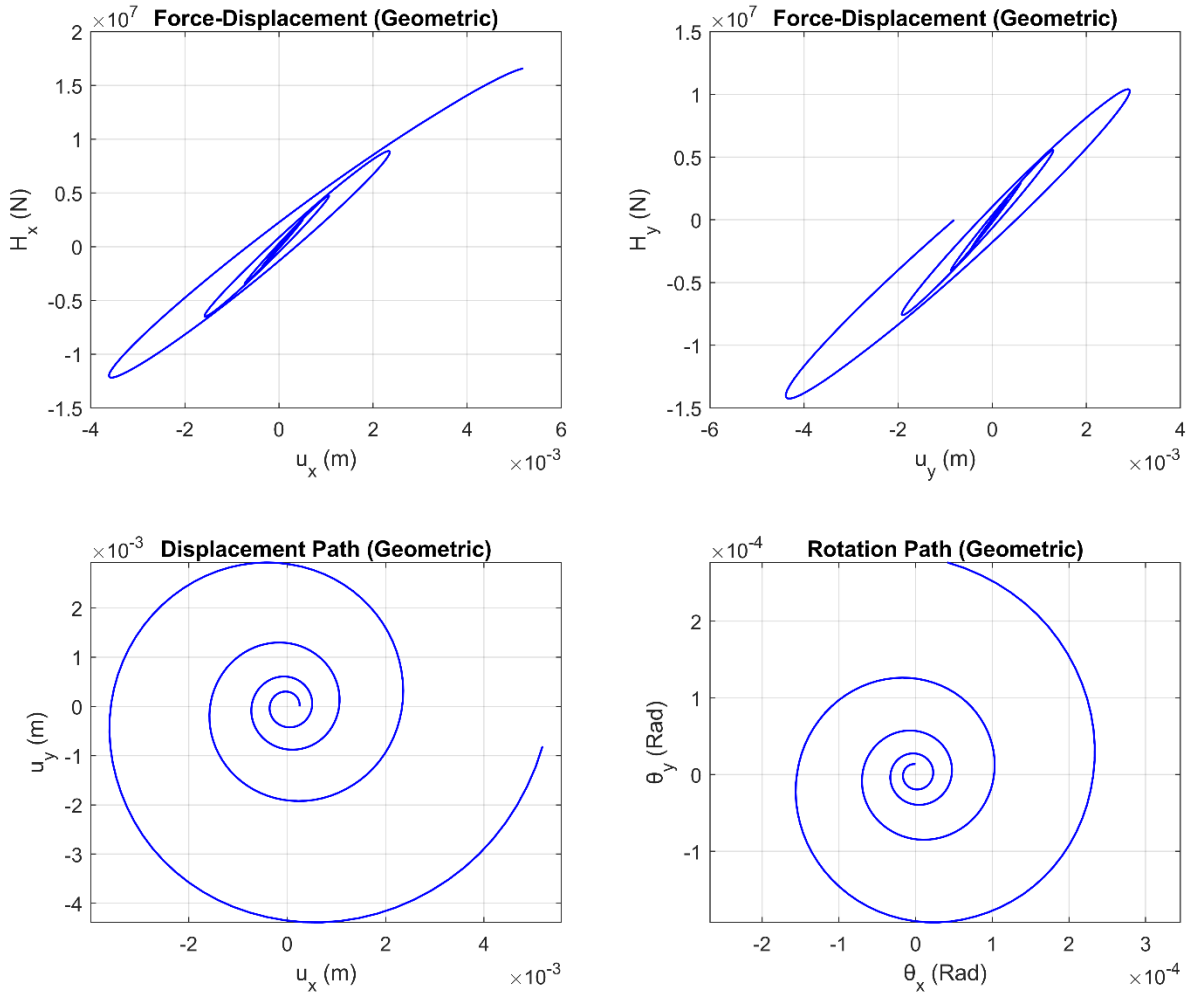

Figure 6. 3. Spiral Load Response with Geometrical Cyclic Increment Rate.

Increasing the total number of cycles beyond 4 obviously will rapidly escalate the response in the case with geometrical increment. The response in Figure 6.3 has high tendency of generating larger hysteresis loops, hence, greater energy dissipation compared to the constant increment case if a higher number of cycles is considered particularly as the load magnitude increases exponentially. This increasing load magnitude will lead to larger displacements, higher stress concentrations, and potentially more significant nonlinear effects.

Observed Phase Shift

The displacement path started in the first quadrant where both the u_x and u_y are positive, hence with the counterclockwise movement, the displacement initially increases in the positive sense in both x and y directions. Whereas, the rotation path started in the second quadrant where the θ_x and θ_y is negative and positive respectively, thus, the rotation is initially in a different phase. This means the displacement response leads rotation response by $90°$. The $90°$ phase difference means that displacement hits its peak in the positive x-direction before rotation shifts into the corresponding position.

This behavior of the foundation with lateral displacements u leading rotations θ could be due to the inertia and the distribution of mass. The monopile experiences lateral forces that push it in one direction, leading to a displacement, which is then followed by a rotational response as the foundation adjusts to maintain equilibrium.

The 90° phase difference between displacement and rotation paths could also suggest a harmonic relationship in the foundation's dynamic response to spiral loads. This phase shift is an indication of the foundation's structural dynamics, where both u and θ responses are coupled but out of phase due to the nature of the cyclic loading – the foundation is behaving in a dynamically coupled manner, where u and θ are interdependent, but not occurring simultaneously in phase. The phase difference also suggests that the foundation is effectively dissipating energy between the u and θ modes.

6.1.2 Coupled Force and Moment Response (P32 and P344 Tests)

To assess the effect of coupled multidirectional loading on the foundation's response, the P32 test signal is applied as a lateral force in the x-direction at the peak value of $0.5H_R$, and the P344 test signal is applied as a moment in the y-direction at the peak value of $0.5M_R$.

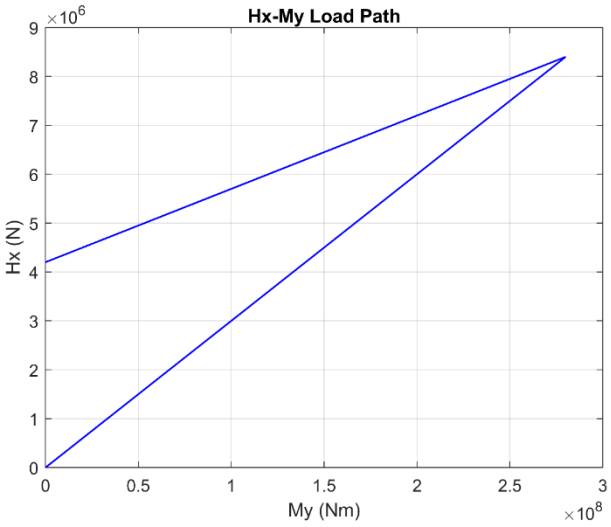

Figure 6. 4. Coupled Force-Moment Load Path (Bidirectional Loading).

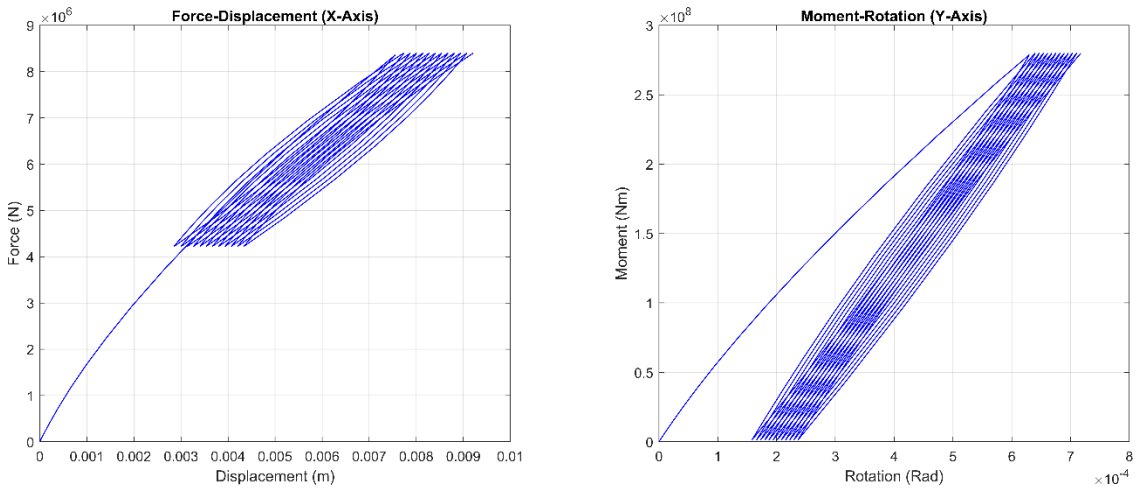

Figure 6. 5. Force-Displacement & Moment-Rotation Responses (Bidirectional Loading).

Larger hysteresis loops are generated in the multidirectional force-displacement response compared to the unidirectional case. Likewise, the peak displacement response in the P32 test-type signal (force-displacement response here) is about 1.813 times the peak value generated in the unidirectional response. Note that in the unidirectional case, full H_R value is

used, but here $0.5H_R$ and $0.5M_R$ are applied as bidirectional loads H_x and M_y respectively. Ratcheting acts in the direction of load, which in this case is more influenced and dominated by the moment load which uses the P344 test signal type.

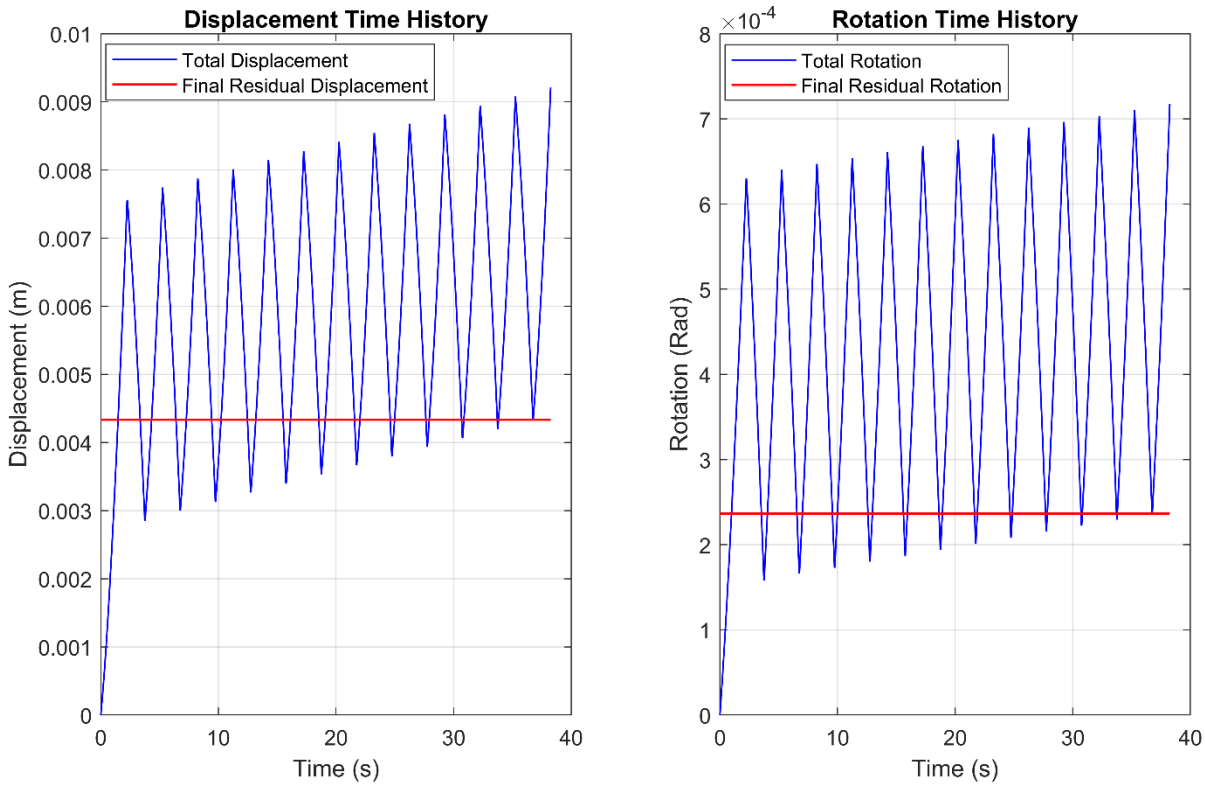

Figure 6. 6. Total Displacement and Rotation Evolution (Bidirectional Loading).

The Figure 6.6 above indicates that both the displacement u_x and rotation θ_y increases with cycle number.

6.2 Complex Cases of Multidirectional Cyclic Loading

For the numerical simulation to assess the response of the model to time-varying irregular waves based on the wind and wave spectrums, the load due to wind acting on the foundation has been made to be 7–10 times larger than that due to wave considering large OWT supported on a diameter monopile. This has been selected for numerical assessment of the model, though, depending the size and dimension of the OWT as well as the specific site condition under investigation, wave load could be significantly higher or lower than the wind load but the moment induced due to the wind is mostly significantly higher than that due to the wave considering higher lever-arm from the point of wind load assessment (typically the hub) to the seabed which could be over 110 m for large OWTs compared to the wave lever-arm which is dependent on the water depth above the seabed, wave height and wave period.

Earthquake bidirectional loading using Landers 0.05 g displacement history is also presented.

6.2.1 Earthquake

Earthquakes are a special case of irregular cyclic loading – offshore structures can experience significant dynamic forces during an earthquake due to ground motion. The earthquake load is typically characterized by high frequency, irregular, and cyclic dynamic forces. The load varies rapidly with time and includes components in multiple directions, leading to complex dynamic responses in structures. This section considers the event of an earthquake load on an OWT supported on a monopile foundation especially located in earthquake-prone regions of the world.

The Landers 0.05 g (low-intensity) earthquake is applied to the monopile foundation as ground motion. Numerical simulation done for the bidirectional earthquake load is in displacement-controlled mode. The response assumed that the OWT experienced an earthquake vibration immediately after installation.

Bidirectional earthquake ground motion is considered hence, the seismic waves are assumed to propagate in two orthogonal horizontal directions (x-axis i.e. the east-west, and y-axis i.e. the north-south) simultaneously during the earthquake. The vertical ground motion component has been ignored, as the two orthogonal horizontal components are assumed to cause the most devastating effect on the foundation. The bidirectional ground motion is crucial as the seismic forces do not occur in just one direction. Ignoring bidirectional effects can lead to underestimation of the forces acting on the monopile foundation during an earthquake, potentially leading to unsafe designs. Figure 6.7 shows the displacement time history of the earthquake. Furthermore, only half this time-history is applied as forces along the x- and y-components of the macro-element model.

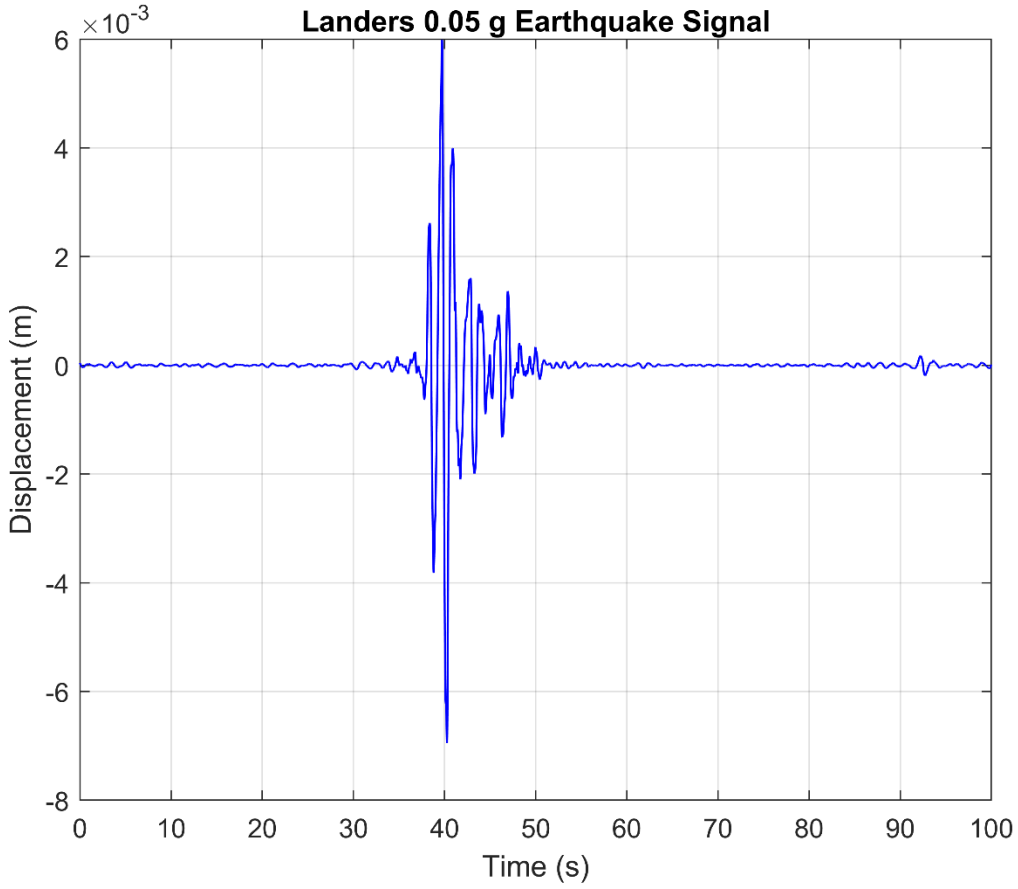

Figure 6. 7. Landers 0.05 g Earthquake Displacement Time History.

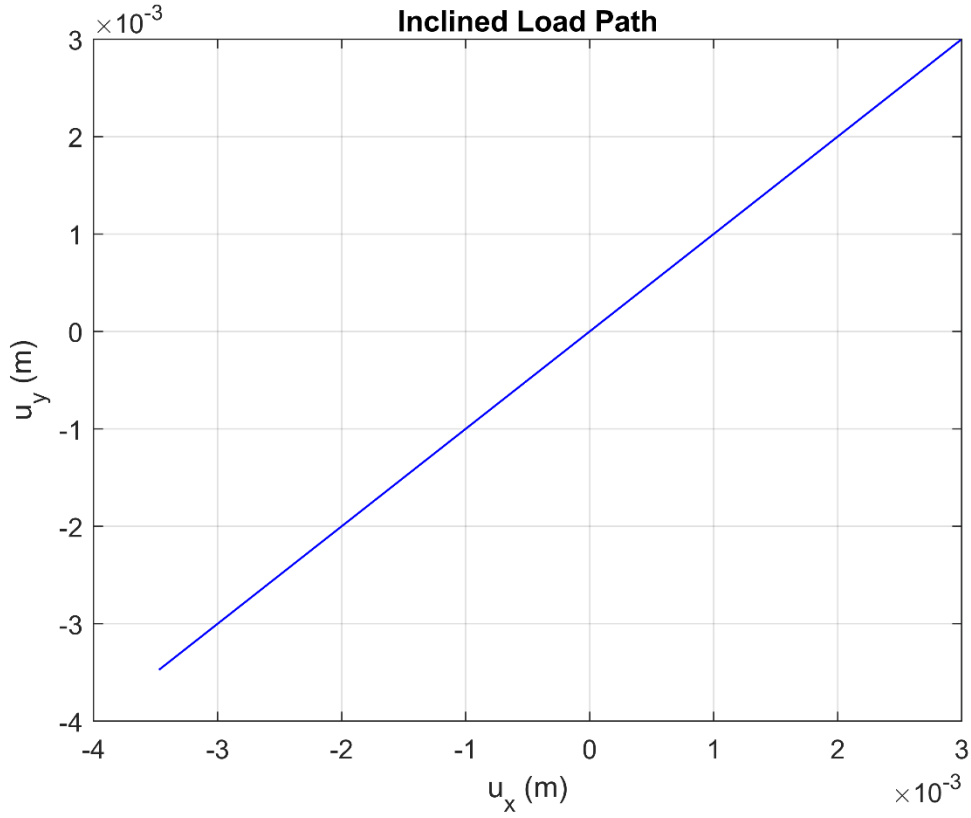

Figure 6. 8. Inclined Load Path at 45° (Bidirectional Loading).

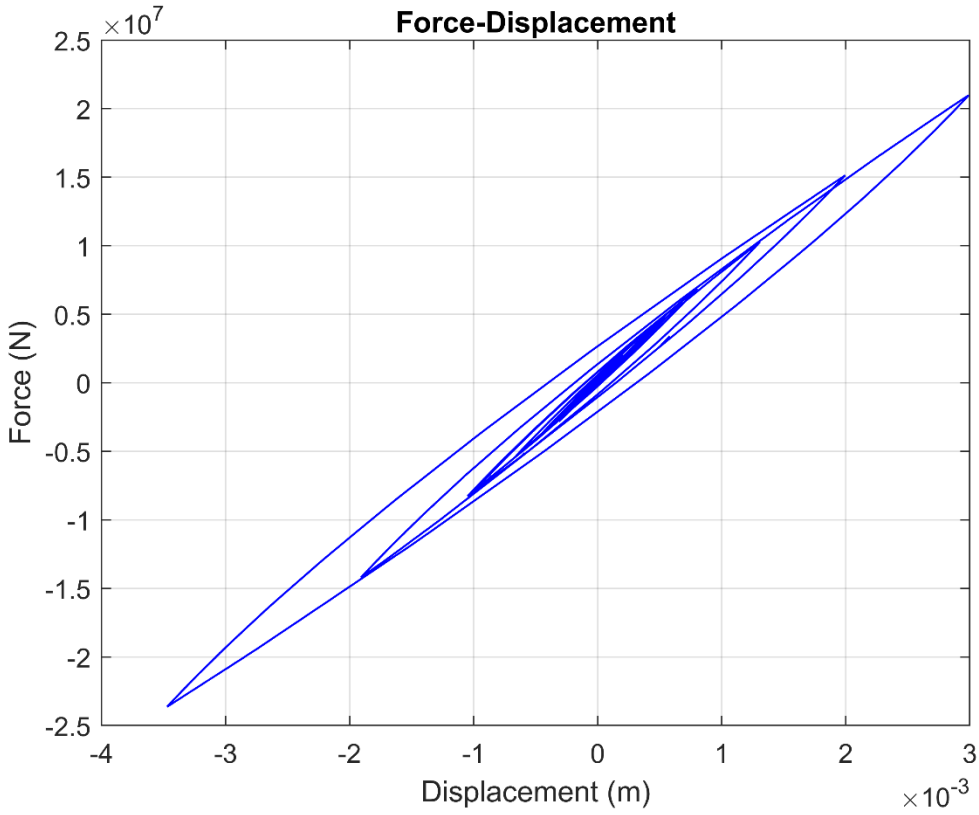

Figure 6. 9. Bidirectional Force-Displacement Response.

The $H_x - u_x$ and $H_y - u_y$ response plots are the same. This is primarily because the same earthquake time history and phase are applied simultaneously in the x and y directions. This leads to the load path being inclined at 45°, which reflects the equal contributions of the seismic load in both directions – assuming uniform and isotropic soil foundation properties. The hysteresis response is that of a 2-way irregular cyclic loading condition. Due to the coupled nature of the model, applied translational displacement under displacement-controlled mode will not only generate the force response but also the induced moments.

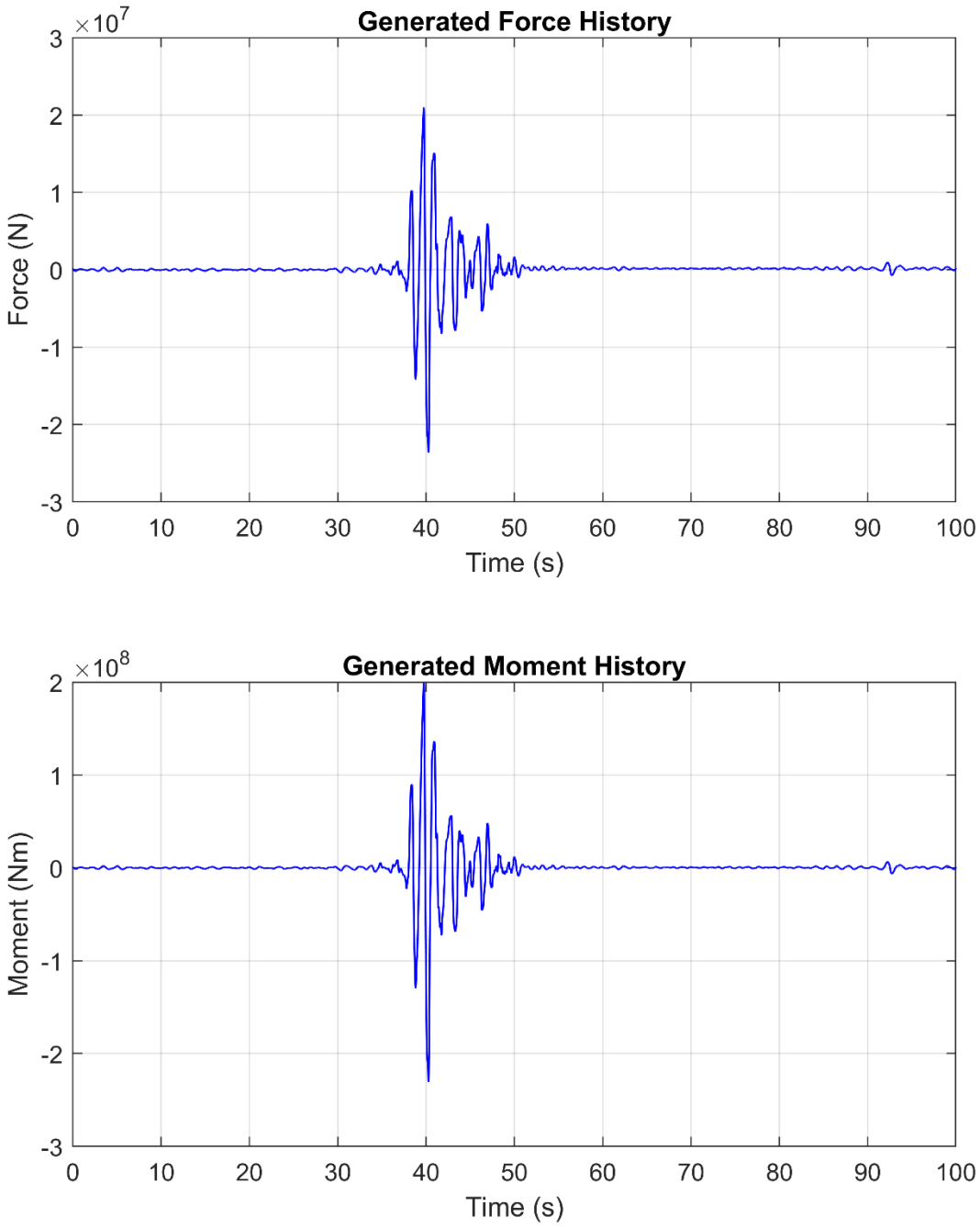

Figure 6. 10. Generated Coupled Force and Moment Time Histories.

The moment response is of an order of magnitude (10 times) higher than the force response.

Peak generated force and moment correspond to the peak ground motion. This results in generating the largest hysteresis loop in the force-displacement plot signifying a large amount of energy dissipated by the foundation during the earthquake. The peak force response is about $1.4H_R$, while the peak generated moment is about $0.4M_R$. Though 0.05 g ground motion is low-intensity, the results indicate that even small seismic events can generate significant moments on the foundation.

6.2.2 Wind and Wave Spectra Loads

To simulate realistic response under multidirectional irregular loading condition, stochastic wind and wave force time-series are generated from a given spectrum. The Kaimal spectrum is used for the wind time series, and the JONSWAP spectrum is used for the wave time series. The generated wave forces are calculated based on directional spectra, with the forces decomposed into x- and y-components. These components are a result of cumulative forces acting in each of the directions. The generated wind forces are added directly to the y-component of the wave forces, suggesting that the wind force is aligned with the y-axis. However, the wave forces are computed over a range of directions (θ_{wave}), which are evenly spaced around the full circle (0 to 2π) at interval of 10° i.e. 36 directions.

Taking into consideration directional misalignment, the wave forces are computed in multiple direction θ_{wave}, with the resultant wave force being a combination of the forces from all directions. The wave loads have components in both x and y directions, depending on the wave direction, while the wind force is only applied purely in the y-direction. The resultant direction of the wave force relative to the x-axis is computed based on the angle of the resultant force vector.

$$\theta_{wave,resultant} = \tan^{-1}\left(\frac{\sum H_{y,wave}}{\sum H_{x,wave}}\right)$$

The computed resultant wave direction is 3.0434 radians (174.3743°) with respect to the x-axis. This indicates that the resultant wave force is nearly opposite to the x-axis, aligning approximately with the negative direction relative to the x-axis.

JONSWAP Spectrum Equations

The equation for the JONSWAP spectrum which is a modification of the Pierson-Moskowitz spectrum is given below:

$$S(f) = \frac{5}{16}.\frac{H_s^2}{T_p^4}.f^{-5}.\exp\left(-\frac{5}{4}.\left(T_p.f\right)^{-4}\right).\gamma^{\alpha}$$

$$\alpha = \exp\left(-\frac{1}{2}.\left(\frac{f-f_p}{\sigma f_p}\right)^2\right)$$

Where H_s is significant wave height, T_p is peak wave period, f is frequency, f_p is peak frequency i.e. the inverse of T_p, γ is peak enhancement factor (3.3 for JONSWAP). The directional distribution which distributes the energy over the different directions is given as;

$$D(\theta_{wave}) = \frac{2}{\pi}\cos^2\theta_{wave}$$

The directional spectrum is given as:

$$S_d(f,\theta_{wave}) = S(f).D(\theta_{wave})$$

Kaimal Spectrum Equations

The Kaimal spectrum is typically used to describe the turbulence in the wind velocity field. Here a simplified formulation of the spectrum is given below.

$$S_u(f) = \frac{4.\sigma_u^2.L_u/U}{(1+6.f.L_u/U)^{\frac{5}{3}}}$$

Where σ_u is the standard deviation of the longitudinal wind speed fluctuations, L_u is turbulence length scale, U is mean wind speed, f is frequency.

Input Parameters

The H_s and T_p are 4 m and 10 s respectively. Water density is $1025\ \mathrm{Kg/m^3}$, monopile diameter is 10 m, wave drag coefficient (C_d) and inertia coefficients (C_m) are 0.7 and 1.2 respectively. The calculated wave frequency range is set from 0.01 Hz to 2 Hz. The width of the wave spectra peak on either side of the peak frequency defined by σ is given as follows;

$$\sigma = \begin{cases} 0.07 & for\ f \leq f_p \\ 0.09 & for\ f > f_p \end{cases}$$

The mean wind speed (U) is $10\ m/s$, σ_u is 1 m/s ($0.1U$). Turbulence length scale (L_u) characterizing the size of turbulent eddies is set to 60 m. The calculated wind frequency range is set from 0.01 Hz to 2 Hz. The wind drag coefficient is 1.2. The generated forces for wind and waves are computed based on Morison's equation.

The wind-induced load is made to be 7–10 times higher than the wave-induced load on the foundation. Considering the coupled nature of the macro-element model, the wind load is applied as a force. This will also generate high rotations equivalence of large moments expected at the foundation for a large OWT supported on a monopile 10 m $\emptyset$ having a long lever arm with respect to the hub (> 110 m i.e. hub to seabed) under extreme conditions.

Simplified Spectra Verification

The distinct wave and wind generation by components i.e. x- and y-component are shown in Figure 6.11 below.

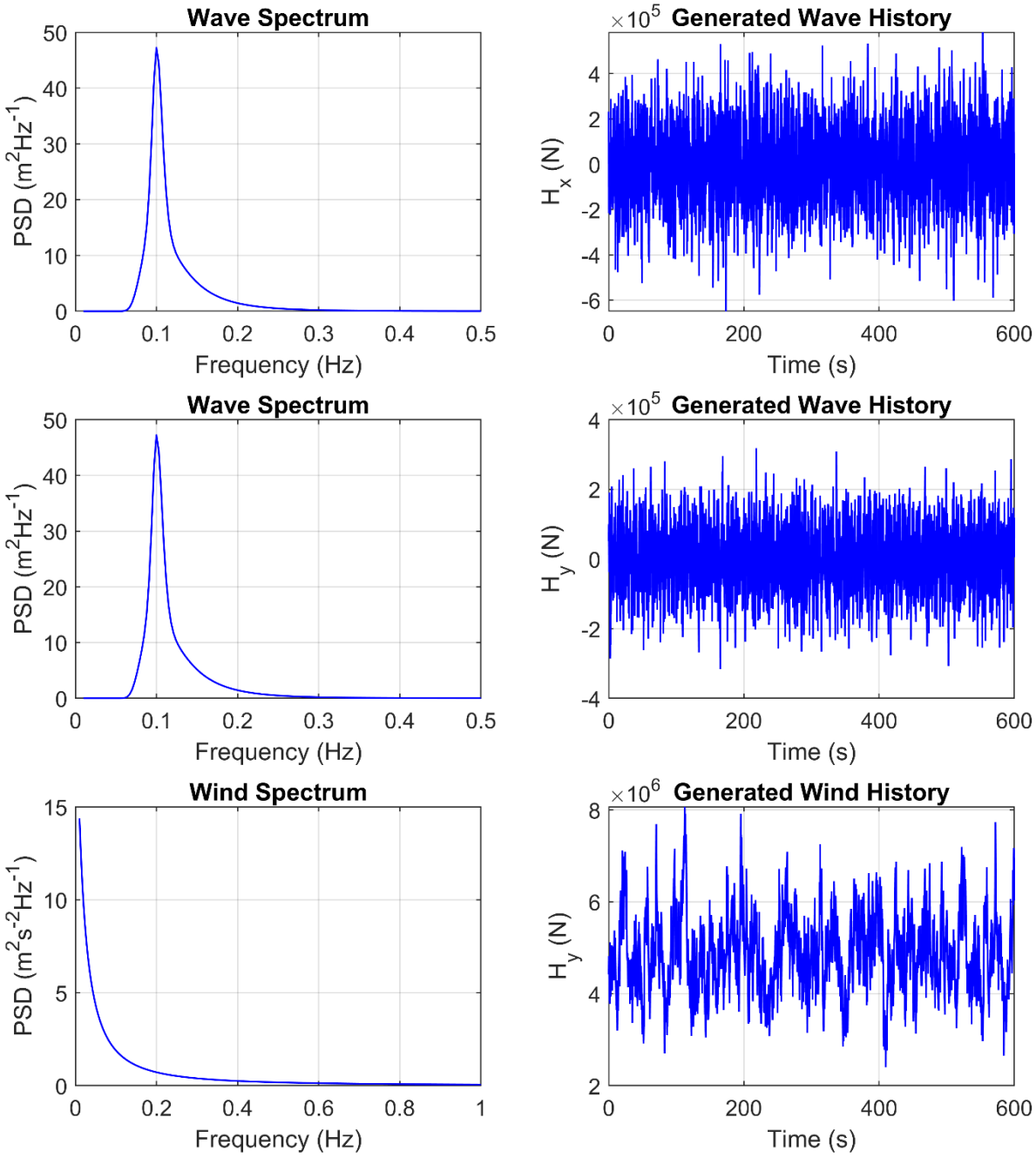

Figure 6. 11. Bidirectional Wave Loads and Unidirectional Wind Load Generation.

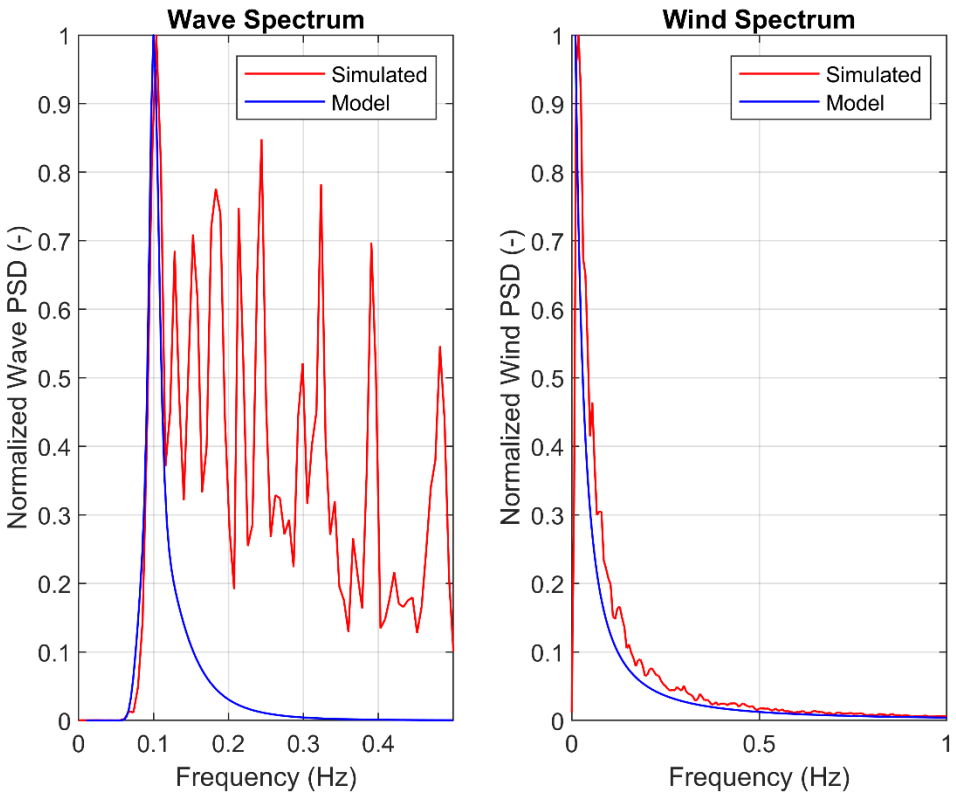

Figure 6. 12. Simple Verification of Simulated Spectra vs Model Spectra.

The peak JONSWAP wave spectrum is at 0.1 Hz with an energy content of $47.25\ \mathrm{m^2Hz^{-1}}$. The computed results indicated that the simulation of signals that tends to mimic real wind and wave signals does not exactly follow the model spectra but is a very close representation of realistic signals. Overall, the PSD comparison between model and simulated spectra indicates good approximation. In the wind spectrum, the comparison enables verification of the fluctuating component of the wind load. The dominant waves frequency is significantly higher than that of the wind as expected. The wind is at the lowest end (left) of the frequency spectrum.

Applied Spectra Loads

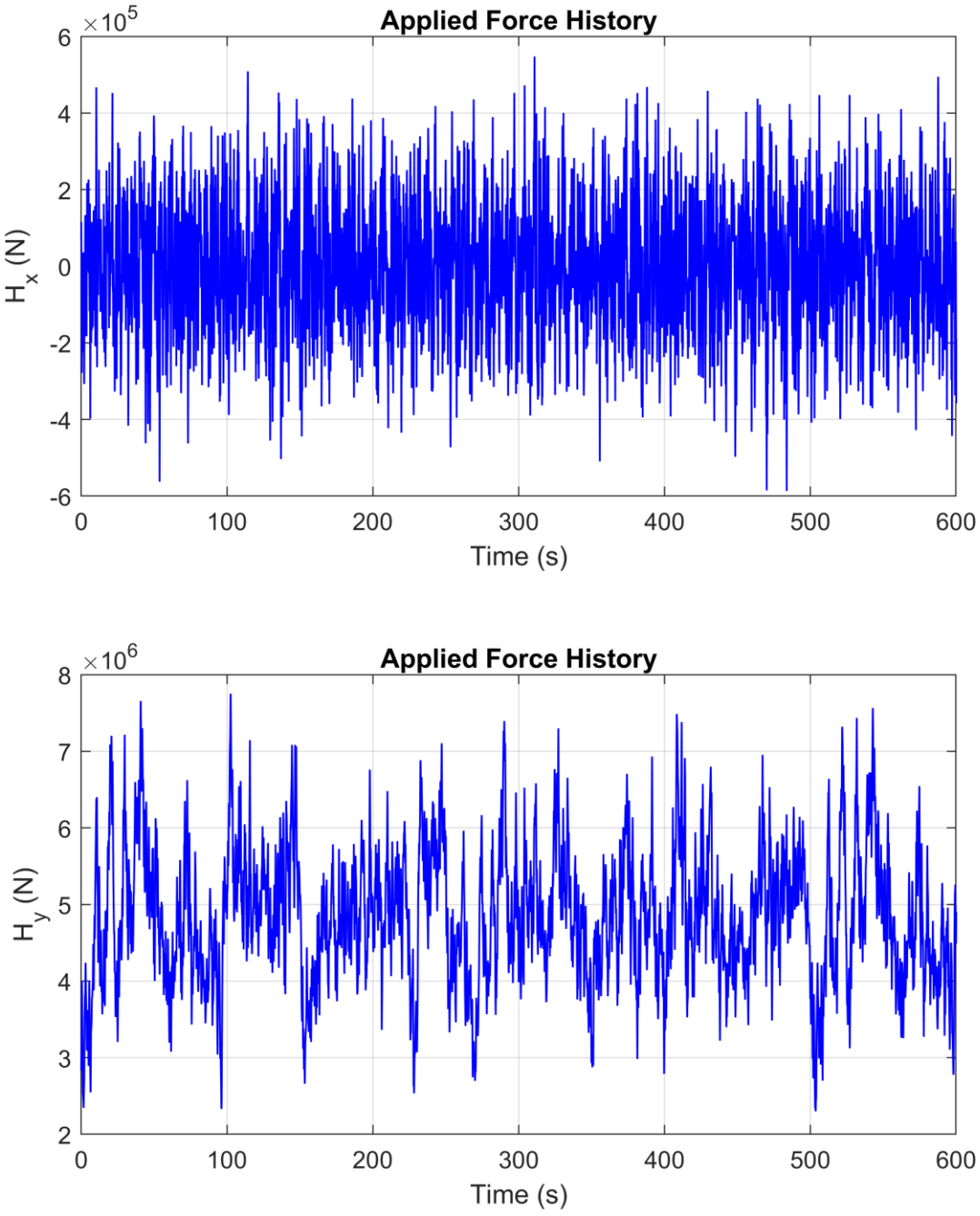

Figure 6. 13. Combined Bidirectional Load History Applied at the Seabed.

The combined load history from wind and wave forces are applied simultaneously in the x and y directions at the seabed level. This enables capturing the interaction between the wind and wave forces over time. The load duration is set to 10 minutes (600 s) sufficient enough to capture dynamic foundation's response to extreme loads, thus allowing for any transient effects to dissipate.

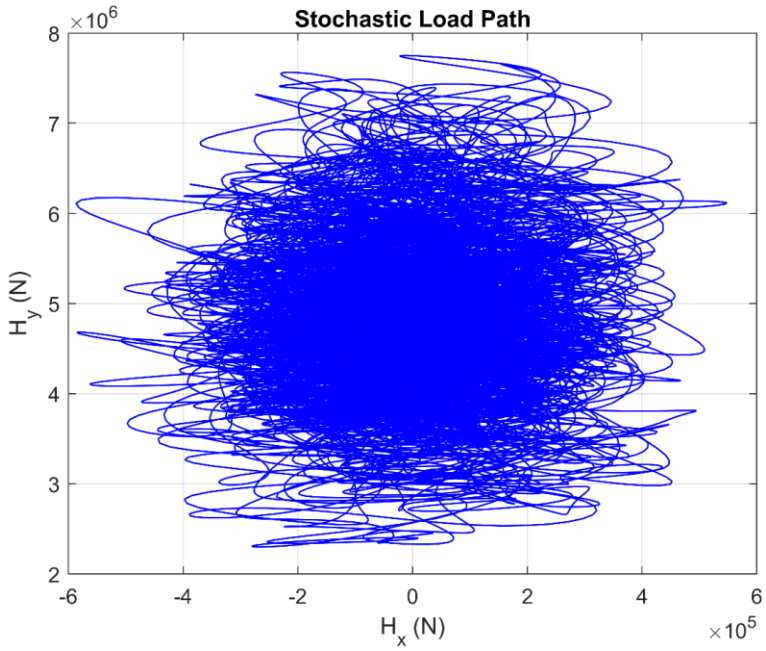

Figure 6. 14. Stochastic (Random) Load Path.

The load path is highly irregular, which is consistent with the stochastic nature of offshore environmental loading with characteristics typical of a short storm event. The bidirectional loading history and stochastic path provide insights into the variability and interaction of offshore environmental forces acting on the monopile foundation.

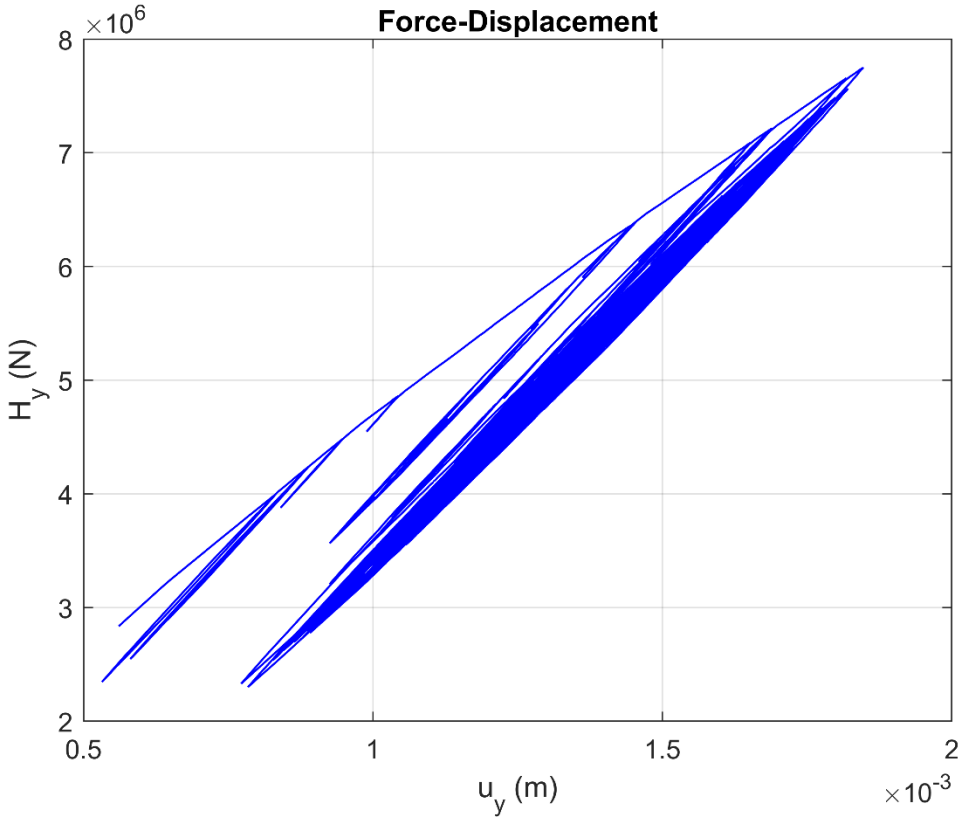

Figure 6. 15. Force-Displacement Response (Y-Component).

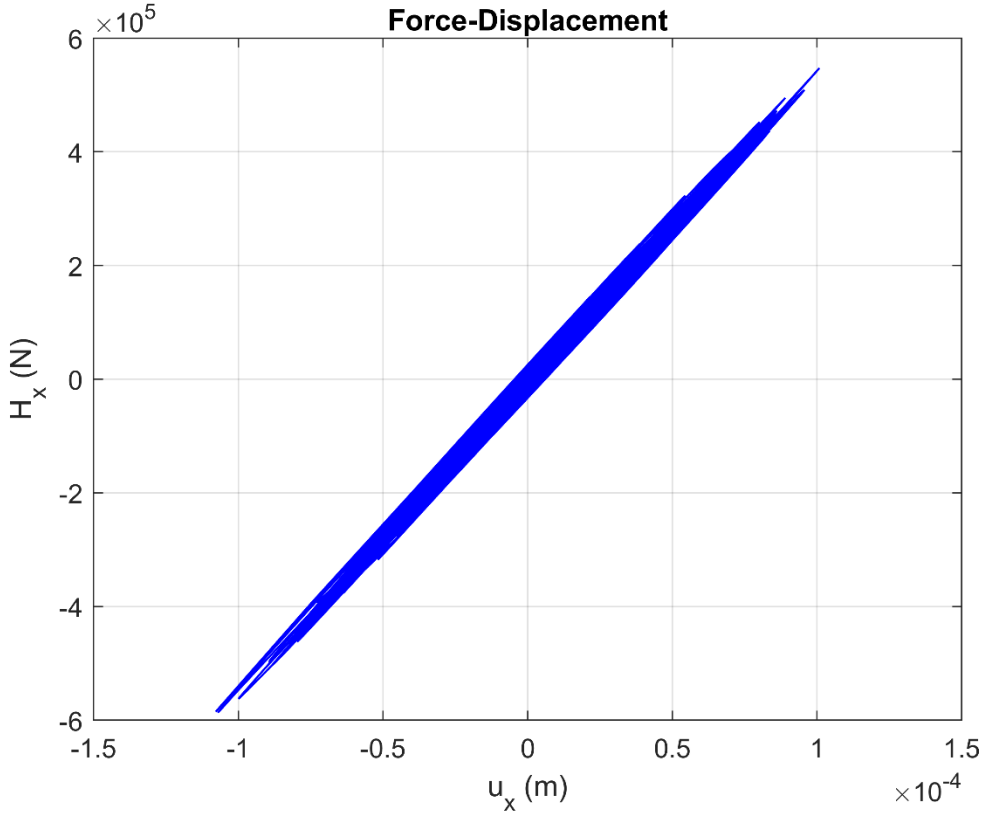

Figure 6. 16. Force-Displacement Response (X-Component).

The force-displacement responses reveal the foundation behavior under the combined load histories. The force-displacement responses are a combination of several loading scenarios including multi-amplitude load packets, with spikes in the load history likely to correspond to the occurrence of high-energy wave events or gusts of wind. The generated hysteresis loops indicate energy dissipation due to damping, which is critical for understanding fatigue behavior.

As expected, there are significant differences between the x and y responses indicating that the response along the y-direction which has the characteristics of a 1-way cyclic loading is of an order of magnitude higher than that of the x-direction which has the characteristic of a 2-way cyclic loading. Thus, significant accumulation of displacement is along the y-component where there's the combined effect of wave and wind loads acting on the foundation.

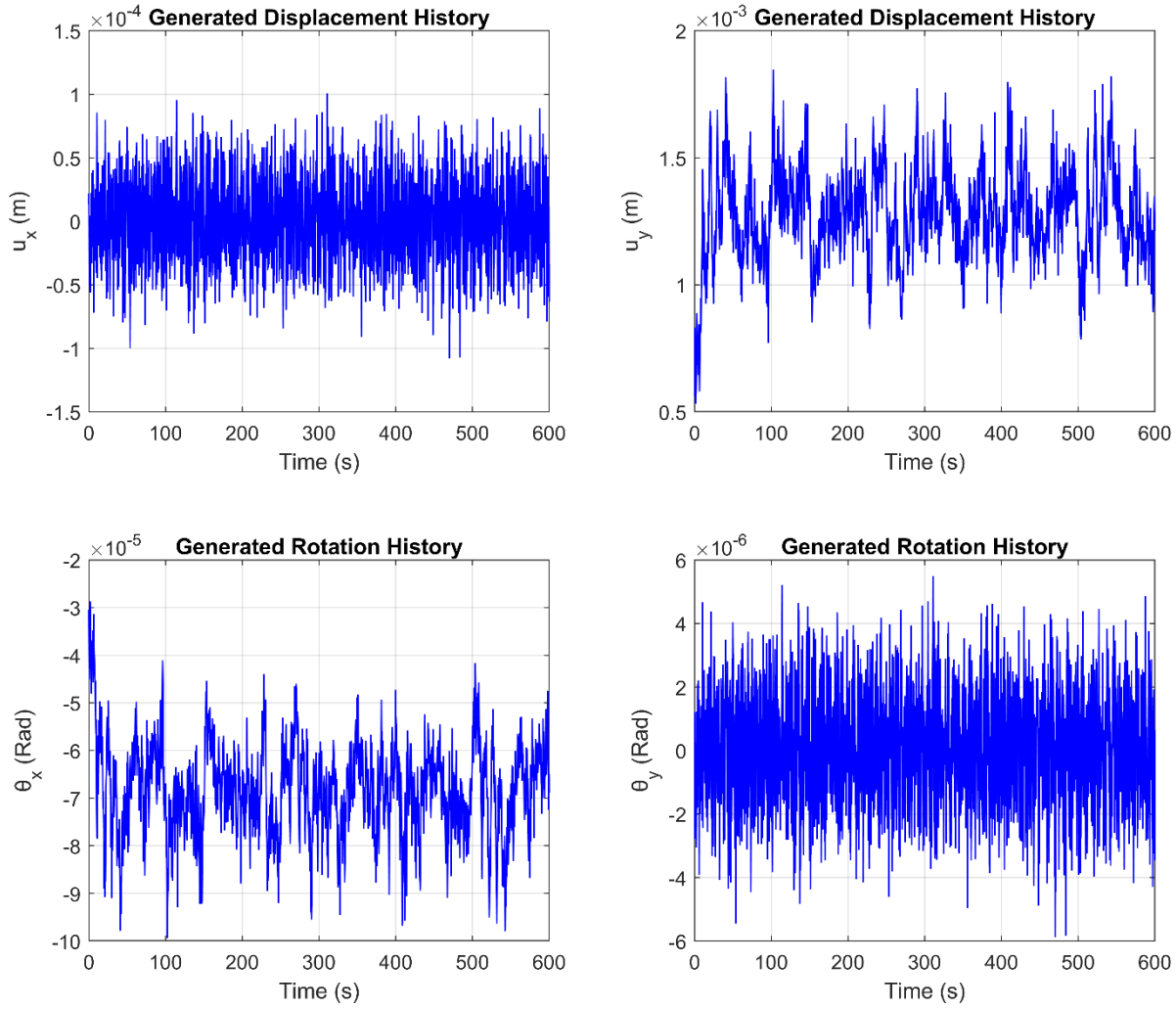

Figure 6. 17. Generated Coupled Displacement and Rotation Time Histories.

Figure 6.17 shows the time histories of generated displacement and rotation at the monopile foundation due to the combined loading condition. The coupled displacement and rotation indicate that the applied loads are causing both translational and rotational responses, which is expected in OWT supported on a monopile structure subjected to complex loading. The displacement time history enables the assessment of the maximum expected deflections, which are critical for determining SLS at small displacements not exceeding $0.0001D$ (one-ten thousandth of monopile diameter), and ULS not exceeding $0.1D$. The rotation history is crucial for understanding potential tilting or rotational instability due to ratcheting, under combined loading conditions acting along the dominant load direction. All these become very obvious under long-term combined cyclic considerations from 1×10^5 cycles to the potential lifetime of the OWT system say 1×10^8cycles typically common for the assessment of the fatigue limit state (FLS) which is composed of very large cycles of small amplitude loads, and then hundreds to thousands of extreme events (including storms). This is currently beyond the scope of the current study. PISA project suggestion is to assume the following limits – 0.1D as the displacement or rotation of 2° at ULS; then 0.25° and 0.5° design limits for tilt rotations at operational state (SLS) and over the lifetime respectively.

Again, peaks in displacement or rotation correspond to spontaneous high-energy events say large waves or strong wind gusts. These are important for identifying critical load cases. The coupled displacement and rotation histories show how these forces translate into physical movements and potential instabilities in the monopile foundation.

Key Coupled Response Effects Observed

The displacement and rotation responses u_x and θ_y are coupled; the same applies to u_y and θ_x. The monopile foundation exhibits coupled dynamic responses, where u_x induce rotations about the perpendicular axis θ_y. Thus, when the foundation experiences a horizontal force due to the wave action, it not only generates translational lateral displacement but also rotation due to corresponding moment generated by the force about it base, hence, the coupled displacement and rotational response.

The rotation θ_x is in the opposite sense relative to the displacement u_y, suggesting that the monopile foundation might be undergoing twisting or torsional response. Therefore, when u_y causes the structure to move horizontally in the y-directional, the torsional stiffness of the monopile foundation can induce a rotation θ_x in the opposite sense to maintain equilibrium. This observed twisting motion could be due to the complex interaction of forces particularly under non-collinear wind and wave loading, where the foundation must balance multiple competing forces, leading to a torsional response.

The x-component of the wave force primarily influences u_x and θ_y, implying that the wave loading in the x-direction drives this coupled response. The y-component which includes the combined low-frequency wind and wave forces influences u_y and θ_x, indicating that the combined wind-wave force in the y-direction drives this second coupled response. This second response is actually dominated by the low frequency wind forces. This wind forces varies more slowly over time compared to the wave loading, and generates corresponding lateral displacement and rotation. In addition, the combined effect of the wind and wave in the y-direction indicates that the foundation is responding to more sustained lower-frequency forces, hence, the u_y and θ_x is more pronounced – dominating the global response of the foundation.

7. RECOMMENDATION & CONCLUSION

7.1 Recommendation

The following are recommended:

(1) Accuracy at Extreme Load Levels: Caution is advised when applying the model at extreme load levels exceeding 50% of the reference values, due to potential approximation limitations of the 0D model at such levels. Nevertheless, the model remains suitable for preliminary global assessments of the foundation's response under these conditions.

(2) Integration with the PISA Model: Integrate the CLAP model with the PISA model by replacing the pushover 3D FEA backbone curves used in model calibration with field test data from PISA.

(3) Optimizing Computation Speed: Consider converting the CLAP implementation from Python/MATLAB to a compiled language such as FORTRAN to enhance computation speed. The compiled code could then be transformed into a Dynamic Link Library (DLL) for integration into design software, facilitating comprehensive aero-hydro-servo-elastic analysis of OWTs.

7.2 Conclusion

Approximately 80–90% of the time invested in this project was dedicated to the transformation and implementation of the HARM and REDWIN constitutive models into functional Python/MATLAB code, followed by the development of the CLAP model and continuous improvements to the code.

The novel model developed can be used in research to investigate the cyclic and complex load regimes experienced by OWT foundations, particularly monopiles and anchors supporting mooring lines. The model effectively captures both ratcheting and coupled lateral multidirectional loading, which, to the best of the author's knowledge, is not currently addressed in existing design guidelines. It also accounts for both stiffness degradation and damping.

In this study, vertical load components, particularly those from the OWT structure's weight and other vertical loads, have been assumed to be small and thus were neglected. However, these vertical components could be important in scenarios such as anchors supporting semi-taut mooring lines or during earthquake events with significant vertical forces. The model can be easily expanded to include vertical components, thereby utilizing the full 6×6 stiffness matrix.

ACKNOWLEDGEMENTS

I would like express deep gratitude to Prof. Philippe Rigo, and Prof. Lionel Gentaz for their invaluable and constructive suggestions during the preparations and development of the programme, their willingness to schedule a meeting when required, and also for the priceless theoretical and practical knowledge gained through offshore structural and hydrodynamics courses taken under them, which has greatly helped.

Thanks to the advisors of this project work – Dr. Christelle Abadie and Dr. Ana Page for their support. Thanks to Dr. Cristian Soriano Camelo (SHAREWIND MSCA Researcher) for his invaluable technical suggestions. I'm also grateful to the entire staff and Professors at LHEEA Department, Ecole Centrale de Nantes for been very supportive throughout the period of study in Marine Technology.

I would like to give my special thanks to my parents whose patience, love, prayers, and encouragement enabled me to complete this work. And finally, thanks to Almighty God who has always been my guide.

REFERENCES

ABADIE, C. N. (2015). Cyclic Lateral Loading of Monopile Foundations in Cohesionless Soils. PhD University of Oxford.

ABADIE, C. N., BYRNE, B. W., & HOULSBY, G. T. (2017). Modelling of Monopile Response to Cyclic Lateral Loading in Sand.

ABADIE, C. N., BEUCKELAERS, W. J. A. P., BYRNE, B. W., HOULSBY, G. T., BURD, H. J., & MCADAM, R. A. (2023). Modeling Lifetime Performance of Monopile Foundations for Offshore Wind Applications. *Journal of Geotechnical and Geoenvironmental Engineering*, *149*(8), 04023051. https://doi.org/10.1061/JGGEFK.GTENG-9833

ABADIE, C. N., BYRNE, B. W., HOULSBY, G. T., BURD, H. J., MCADAM, R. A., & BEUCKELAERS, W. J. A. P. (2020). Modelling of Offshore Wind Monopile Lifetime Performance. *4th International Symposium on Frontiers in Offshore Geotechnics (ISFOG)*. https://doi.org/10.17863/CAM.83193

ABADIE, C. N., BYRNE, B. W., & HOULSBY, G. T. (2018). Rigid Pile Response to Cyclic Lateral Loading: Laboratory Tests. *Géotechnique*, *69*(10), 863–876. https://doi.org/10.1680/jgeot.16.P.325

ABADIE, C. N., HOULSBY, G. T., & BYRNE, B. W. (2019). A Method for Calibration of the Hyperplastic Accelerated Ratcheting Model (HARM). *Computers and Geotechnics*, *112*, 370–385. https://doi.org/10.1016/j.compgeo.2019.04.017

ALBIKER, J., ACHMUS, M., FRICK, D., & FLINDT, F. (2017). 1 g Model Tests on the Displacement Accumulation of Large-Diameter Piles Under Cyclic Lateral Loading. *Geotechnical Testing Journal*, *40*(2), 173–184. https://doi.org/10.1520/GTJ20160102

BERGUA, R., ROBERTSON, A., JONKMAN, J., & PLATT, A. (2021b). Specification Document for OC6 Phase II: Verification of an Advanced Soil-Structure Interaction Model for Offshore Wind Turbines. https://doi.org/10.2172/1811648

BERGUA, R., ROBERTSON, A., JONKMAN, J., PLATT, A., PAGE, A., QVIST, J., AMET, E., CAI, Z., HAN, H., BEARDSELL, A., SHI, W., GALVAN, J., BACHYNSKI-POLIC, E., MCKINNON, G., HARNOIS, V., BONNET, P., SUJA-THAUVIN, L., HANSEN, A., ALONSO, I., ARISTONDO, A., BATTISTELLA, T., GUANCHE, R., SCHUNEMANN, P., PHAM, T-D., TRUBAT, P., ALARCON, D., HAUDIN, F., NGUYEN, M., & GOVEAS, A. (2021a). OC6 Phase II: Integration and Verification of a New Soil-Structure Interaction Model for Offshore Wind Design. *Wind Energy*, *25*(5), 793–810. https://doi.org/10.1002/we.2698

BEUCKELAERS, W. J. A. P. (2015). Fatigue Life Calculation of Monopiles for Offshore Wind Turbines using a Kinematic Hardening Soil Model. https://www.semanticscholar.org/paper/Fatigue-life-calculation-of-monopiles-for-offshore-Beuckelaers/ac9109b71c7a7a4164bf119ddf1cc782e6731141

BEUCKELAERS, W. J. P. (2017). Numerical Modelling of Laterally Loaded Piles for Offshore Wind Turbines. PhD, University of Oxford.

BEUCKELAERS, W. J. A. P., BURD, H. J., & HOULSBY, G. T. (2017). Integrated Design Method of Monopile Foundations for Offshore Wind Turbines using a Kinematic Hardening Soil Model. 1108–1115. https://doi.org/10.3723/OSIG17.1108

BURD, H. J., ABADIE, C. N., BYRNE, B. W., HOULSBY, G. T., MARTIN, C. M., MCADAM, R. A., JARDINE, R. J., PEDRO, A. M. G., POTTS, D. M., TABORDA, D. M. G., ZDRAVKOVIĆ, L., & ANDRADE, M. P. (2020). Application of the PISA Design Model to Monopiles Embedded in Layered Soils. *Géotechnique*, *70*(11), 1067–1082. https://doi.org/10.1680/jgeot.20.PISA.009

BURD, H. J., TABORDA, D. M. G., ZDRAVKOVIC, L., ABADIE, C. N., BYRNE, B. W., HOULSBY, G. T., GAVIN, K. G., IGOE, D. J. P., JARDINE, R. J., MARTIN, C. M., MCADAM, R. A., PEDRO, A. M. G., & POTTS, D. M. (2019).

PISA Design Model for Monopiles for Offshore Wind Turbines: Application to a Marine Sand. *Geotechnique*, *70*(11), 1048–1066. https://doi.org/10.1680/jgeot.18.P.277

BUTTERFIELD, R., HOULSBY, G. T., & GOTTARDI, G. (1997). Standardized Sign Conventions and Notation for Generally Loaded Foundations. *Géotechnique*, *47*(5), 1051–1054. https://doi.org/10.1680/geot.1997.47.5.1051

BYRNE, B. W., MCADAM, R. A., BEUCKELAERS, W. J. A. P., BURD, H. J., GAVIN, K., HOULSBY, G. T., IGOE, D. J. P., JARDINE, R., MARTIN, C. M., POTTS, D. M., TABORDA, D. M. G., & ZDRAVKOVIĆ, L. (2020a). Cyclic Laterally Loaded Medium Scale Field Pile Testing for the PISA Project. *Proceedings Fourth International Symposium on Frontiers in Offshore Geotechnics*, 1323–1332.

BYRNE, B. W., MCADAM, R. A., BURD, H. J., BEUCKELAERS, W. J. A. P., GAVIN, K. G., HOULSBY, G. T., IGOE, D. J. P., JARDINE, R. J., MARTIN, C. M., MUIRWOOD, A., POTTS, D. M., GRETLUND, J. S., TABORDA, D. M. G., & ZDRAVKOVIC´, L. (2020b). Monotonic Laterally Loaded Pile Testing in a Stiff Glacial Clay Till at Cowden. *Geotechnique*, *70*(11), 970–985. https://doi.org/10.1680/jgeot.18.PISA.003

BYRNE, B. W., MCADAM, R. A., BURD, H. J., HOULSBY, G. T., MARTIN, C. M., BEUCKELAERS, W., ZDRAVKOVIĆ, L., TABORDA, D. M. G., GAVIN, K., & JARDINE, R. J. (2017). PISA: New Design Methods for Offshore Wind Turbine Monopiles. *Proceedings of the 8th International Conference for Offshore Site Investigation and Geotechnics*.

CHALOULOS, Y. K., TASIOPOULOU, P., GIANNAKOU, A., CHACKO, J., AGHAKOUCHAK, A., & STERGIOU, T. (2024). Fully-Coupled Cyclic Time-History Analyses of Monopile Foundations in Sand. *Ocean Engineering*, *298*, 116691. https://doi.org/10.1016/j.oceaneng.2024.116691

COLLINS, I. F., & HOULSBY, G. T. (1997). Application of Thermomechanical Principles to the Modelling of Geotechnical Materials. *Proceedings of the Royal Society of London. Series A: Mathematical, Physical and Engineering Sciences*, *453*(1964), 1975–2001. https://doi.org/10.1098/rspa.1997.0107

FITZGERALD, B., & BASU, B. (2020). Vibration Control of Wind Turbines: Recent Advances and Emerging Trends. *International Journal of Sustainable Materials and Structural Systems*, *4*, 347. https://doi.org/10.1504/IJSMSS.2020.109090

FREDERICK, C. O., & ARMSTRONG, P. J. (2007). A Mathematical Representation of the Multiaxial Bauschinger Effect. *Materials at High Temperatures*, *24*(1), 1–26. https://doi.org/10.1179/096034007X207589

GAO, Z., YAN, L., & WHYTE, S. (2023). B-SDM: A Bounding Surface Stiffness Degradation Method for Modelling the Long-Term Ratcheting Response of Offshore Wind Turbine Foundations. *Computers and Geotechnics*, *154*, 105157. https://doi.org/10.1016/j.compgeo.2022.105157

GORINI, D. N., & CALLISTO, L. (2023). A Multiaxial Inertial Macro-element for Deep Foundations. *Computers and Geotechnics*, *155*, 105222. https://doi.org/10.1016/j.compgeo.2022.105222

HAIDERALI, A. E., MADABHUSHI, G. S. P., & NAKASHIMA, M. (2023). Numerical Investigation of Monopiles in Structured Clay under Cyclic Loading. *Ocean Engineering*, *289*, 116181. https://doi.org/10.1016/j.oceaneng.2023.116181

HONG, Y., YAO, M., & WANG, L. (2023). A Multi-Axial Bounding Surface p-y Model with Application in Analyzing Pile Responses under Multi-Directional Lateral Cycling. *Computers and Geotechnics*, *157*, 105301. https://doi.org/10.1016/j.compgeo.2023.105301

HOULSBY, G., & PUZRIN, A. (2006). Principles of Hyperplasticity: An Approach to Plasticity Theory Based on Thermodynamic Principles. (pp. 1–351). https://doi.org/10.1007/978-1-84628-240-9

HOULSBY, G. T. (2014). Dissipation Rate Functions, Pseudopotentials, Potentials and Yield Surfaces. In DEWAR, R. C., LINEWEAVER, C. H., NIVEN, R. K., & REGENAUER-LIEB, K. (Editors), *Beyond the Second Law: Entropy Production and Non-equilibrium Systems* (pp. 73–95). Springer. https://doi.org/10.1007/978-3-642-40154-1_4

HOULSBY, G. T., ABADIE, C. N., BEUCKELAERS, W. J. A. P., & BYRNE, B. W. (2017). A Model for Nonlinear Hysteretic and Ratcheting Behaviour. *International Journal of Solids and Structures*, *120*, 67–80. https://doi.org/10.1016/j.ijsolstr.2017.04.031

HOULSBY, G. T., & PUZRIN, A. M. (1999). A Thermomechanical Framework for Constitutive Models for Rate-Independent Dissipative Materials. *International Journal of Plasticity*, *16*(9), 1017–1047. https://doi.org/10.1016/S0749-6419(99)00073-X

HOULSBY, G. T., & PUZRIN, A. M. (2002). Rate-Dependent Plasticity Models Derived from Potential Functions. *Journal of Rheology*, *46*(1), 113–126. https://doi.org/10.1122/1.1427911

HOULSBY, G. T., & RICHARDS, I. A. (2023). Multi-Surface and Bounding Surface Models in Hyperplasticity. *Computers and Geotechnics*, *156*, 105143. https://doi.org/10.1016/j.compgeo.2022.105143

IWAN, W. D. (1967). On a Class of Models for the Yielding Behavior of Continuous and Composite Systems. *Journal of Applied Mechanics*, *34*(3), 612–617. https://doi.org/10.1115/1.3607751

KLINKVORT, R. T., STURM, H., PAGE, A., ZHANG, Y., & JOSTAD, H. (2020, August 16). A Consistent, Rigorous and Super-Fast Monopile Design Approach. *4th International Symposium on Frontiers in Offshore Geotechnics*. ISFOG.

KOITER, W. T. (1953). Stress-Strain Relations, Uniqueness and Variational Theorems for Elastic-Plastic Materials with a Singular Yield Surface. *Quarterly of Applied Mathematics*, *11*(3), 350–354. https://doi.org/10.1090/qam/59769

LETCHER, T. M. (Editor). (2017). Wind Energy Engineering: A Handbook for Onshore and Offshore Wind Turbines. *Academic Press, an imprint of Elsevier*.

LIU, H., JOSTAD, H., & SIVASITHAMPARAM, N. (2023). Validation of REDWIN Model in Sandy Soil under various Drainage Conditions. https://doi.org/10.53243/NUMGE2023-138

LIU, H., & KAYNIA, A. M. (2022). Monopile Responses to Monotonic and Cyclic Loading in Undrained Sand using 3D FE with SANISAND-MSu. *Water Science and Engineering*, *15*(1), 69–77. https://doi.org/10.1016/j.wse.2021.12.001

LIU, H., PISANÒ, F., JOSTAD, H. P., & SIVASITHAMPARAM, N. (2022). Impact of Cyclic Strain Accumulation on the Tilting behaviour of Monopiles in Sand: An Assessment of the Miner's Rule based on SANISAND-MS 3D FE Modelling. *Ocean Engineering*, *250*, 110579. https://doi.org/10.1016/j.oceaneng.2022.110579

LOPEZ-QUEROL, S., CUI, L., & BHATTACHARYA, S. (2023). Numerical Methods for Soil-Structure Interaction Analysis of Offshore Wind Turbine Foundations. In T. M. Letcher (Ed.), *Wind Energy Engineering (Second Edition)* (pp. 177–193). Academic Press. https://doi.org/10.1016/B978-0-323-99353-1.00003-7

LUO, R., LI, W., & YANG, M. (2016). Accumulated Response of Offshore Large-Diameter Monopile under Lateral Cyclic Loading. *37*, 607–612. https://doi.org/10.16285/j.rsm.2016.S2.076

MASING, G. (1926). Eigenspannungen und Verfestigung beim Messing. 332–335.

MATLOCK, H. (1970). Correlation for Design of Laterally Loaded Piles in Soft Clay. *Offshore Technology Conference*. https://doi.org/10.4043/1204-MS

MCADAM, R. A., BYRNE, B. W., HOULSBY, G. T., BEUCKELAERS, W. J. A. P., BURD, H. J., GAVIN, K. G., IGOE, D. J. P., JARDINE, R. J., MARTIN, C. M., MUIR WOOD, A., POTTS, D. M., SKOV GRETLUND, J., TABORDA, D. M. G., & ZDRAVKOVIĆ, L. (2020). Monotonic Laterally Loaded Pile Testing in a Dense Marine Sand at Dunkirk. *Géotechnique*, *70*(11), 986–998. https://doi.org/10.1680/jgeot.18.PISA.004

MENG, X., ZHAI, E., & XU, C. (2024). A Hypoplastic Macro-element Model for Offshore Wind Turbine Large-Diameter Monopiles in Sand. *Ocean Engineering*, *294*, 116744. https://doi.org/10.1016/j.oceaneng.2024.116744

MRÓZ, Z. (1967). On the Description of Anisotropic Workhardening. *Journal of the Mechanics and Physics of Solids*, *15*(3), 163–175. https://doi.org/10.1016/0022-5096(67)90030-0

NANDA, S., ARTHUR, I., SIVAKUMAR, V., DONOHUE, S., BRADSHAW, A., KELTAI, R., GAVIN, K., MACKINNON, P., RANKIN, B., & GLYNN, D. (2017). Monopiles Subjected to Uni- and Multi-Lateral Cyclic Loading. *Proceedings of the Institution of Civil Engineers - Geotechnical Engineering*, *170*(3), 246–258. https://doi.org/10.1680/jgeen.16.00110

NIGITHA, D., RATHOD, D., & KRISHNANUNNI, K. T. (2023). Finite-Element Analysis of a Monopile under One- and Two-Way Lateral Cyclic Loading. *Proceedings of the Institution of Civil Engineers - Maritime Engineering*, *176*(3), 138–157. https://doi.org/10.1680/jmaen.2021.027

PAGE, A. M., GRIMSTAD, G., EIKSUND, G. R., & JOSTAD, H. P. (2018). A Macro-element Pile Foundation Model for Integrated Analyses of Monopile-based Offshore Wind Turbines. *Ocean Engineering*, *167*, 23–35. https://doi.org/10.1016/j.oceaneng.2018.08.019

PAGE, A. M., GRIMSTAD, G., EIKSUND, G. R., & JOSTAD, H. P. (2019a). A Macro-element Model for Multidirectional Cyclic Lateral Loading of Monopiles in Clay. *Computers and Geotechnics*, *106*, 314–326. https://doi.org/10.1016/j.compgeo.2018.11.007

PAGE, A. M., NORÉN-COSGRIFF, K., SKAU, K. S., & KAYNIA, A. M. (2019b). REDWIN Foundation Models for Integrated Dynamic Analyses of Offshore Wind Turbines. *ASME 2019 38th International Conference on Ocean, Offshore and Arctic Engineering*. https://doi.org/10.1115/OMAE2019-96168

PAGE, A. M., SKAU, K. S., JOSTAD, H. P., & EIKSUND, G. R. (2017). A New Foundation Model for Integrated Analyses of Monopile-based Offshore Wind Turbines. *Energy Procedia*, *137*, 100–107. https://doi.org/10.1016/j.egypro.2017.10.337

PAUL, S. K. (2019). A Critical Review of Experimental Aspects in Ratcheting Fatigue: Microstructure to Specimen to Component. *Journal of Materials Research and Technology*, *8*(5), 4894–4914. https://doi.org/10.1016/j.jmrt.2019.06.014

PERZYNA, P. (1966). Fundamental Problems in Viscoplasticity. In CHERNYI, G. G., DRYDEN, H. L., GERMAIN, P., HOWARTH, L., OLSZAK, W., PRAGER, W., PROBSTEIN, R. F., & ZIEGLER, H. (Editors), *Advances in Applied Mechanics* (Vol. 9, pp. 243–377). Elsevier. https://doi.org/10.1016/S0065-2156(08)70009-7

PRAGER, W. (1949). Recent Developments in the Mathematical Theory of Plasticity. *Journal of Applied Physics*, *20*(3), 235–241. https://doi.org/10.1063/1.1698348

RICHARDS, I. A. (2019). Monopile Foundations under Complex Cyclic Lateral Loading. PhD, University of Oxford. https://ora.ox.ac.uk/objects/uuid:bc3fc931-1c15-4abf-a367-42b5b4971d2a

RICHARDS, I. A., BRANSBY, M. F., BYRNE, B. W., GAUDIN, C., & HOULSBY, G. T. (2021). Effect of Stress Level on Response of Model Monopile to Cyclic Lateral Loading in Sand. *Journal of Geotechnical and Geoenvironmental Engineering*, *147*(3), 04021002. https://doi.org/10.1061/(ASCE)GT.1943-5606.0002447

RICHARDS, I. A., BYRNE, B. W., & HOULSBY, G. T. (2020). Monopile Rotation under Complex Cyclic Lateral Loading in Sand. *Géotechnique*, *70*(10). https://ora.ox.ac.uk/objects/uuid:d6781f67-e65a-4b2b-b9b7-b860bcdf7bd0

ROSQUOËT, F. (2004). Pile Under Lateral Cyclic Load. PhD, Ecole Centrale & Université de Nantes.

SKAU, K. S., GRIMSTAD, G., PAGE, A. M., EIKSUND, G. R., & JOSTAD, H. P. (2018b). A Macro-element for Integrated Time Domain Analyses Representing Bucket Foundations for Offshore Wind Turbines. *Marine Structures*, *59*, 158–178. https://doi.org/10.1016/j.marstruc.2018.01.011

SKAU, K. S., PAGE, A. M., KAYNIA, A. M., LØVHOLT, F., NORÉN-COSGRIFF, K., STURM, H., ANDERSEN, H. S., NYGARD, T. A., JOSTAD, H. P., EIKSUND, G., HAVMØLLER, O., STRØM, P., & EICHLER, D. (2018a). REDWIN - REDucing Cost in Offshore WINd by Integrated Structural and Geotechnical Design. *1104*, 012029. *Journal of Physics Conference Series*. https://doi.org/10.1088/1742-6596/1104/1/012029

SUN, Y., XU, C., NAGGAR, M. H. E., DU, X., & DOU, P. (2023). Cumulative Cyclic Response of Offshore Monopile in Sands. *Applied Ocean Research*, *133*, 103481. https://doi.org/10.1016/j.apor.2023.103481

VAN HOOGSTRATEN, S. C., HERMAN, S. J., VERSTEIJLEN, W. G., PAGE, A. M., GRIMSTAD, G., PISANÒ, F., & METRIKINE, A. V. (2020). The Macro-element Method for Offshore Wind Turbines Exposed to Extreme Loads in the Asia-Pacific Region. *4th International Symposium on Frontiers in Offshore Geotechnics*. ISFOG.

XU, M., ZHOU, W., SHEN, K., ZHANG, Y., & GUO, Z. (2024). Enhanced Multi-Springs Model for Estimating Suction Caisson Responses under Cyclic Lateral Loading. *Ocean Engineering*, *302*, 117651. https://doi.org/10.1016/j.oceaneng.2024.117651

YANG, M., LUO, R., & LI, W. (2017). Numerical Study on Accumulated Deformation of Laterally Loaded Monopiles used by Offshore Wind Turbine. *Bulletin of Engineering Geology and the Environment*, *77*(3), 911–921. https://doi.org/10.1007/s10064-017-1138-9

ZHA, X., GUO, Z., WANG, L., & RUI, S. (2022). A Simplified Model for Predicting the Accumulated Displacement of Monopile under Horizontal Cyclic Loadings. *Applied Ocean Research*, *129*, 103389. https://doi.org/10.1016/j.apor.2022.103389

ZHA, X., LAI, Y., RUI, S., & GUO, Z. (2023). Fatigue Life Analysis of Monopile-Supported Offshore Wind Turbines based on Hyperplastic Ratcheting Model. *Applied Ocean Research*, *136*, 103595. https://doi.org/10.1016/j.apor.2023.103595

ZHANG, C., WANG, D., & ZHENG, J. (2023). A Cyclic-Softening Macro-element Model for Mono-Bucket Foundations Supporting Offshore Wind Turbines in Clay. *Computers and Geotechnics*, *161*, 105603. https://doi.org/10.1016/j.compgeo.2023.105603

ZIEGLER, H. (1959). A Modification of Prager's Hardening Rule. *Quarterly of Applied Mathematics*, *17*(1), 55–65.

ZIEGLER, H. (1977). An Introduction to Thermomechanics. http://archive.org/details/introductiontoth0021hans

APPENDIX

A. Glossary

(1) Back-stress: The back-stress represents the center of the yield surface and evolves with plastic deformation. It is the internal kinematic hardening variable which represents the internal stress that opposes the external loading, causing the yield surface to translate in space. It characterizes the material's internal state and its evolution under loading. The back-stress evolves with the accumulation of plastic strain.

(2) Bauschinger effect: The Bauschinger effect refers to the phenomenon where the material exhibits different yield strengths in tension and compression.

(3) Ratcheting: Ratcheting is the accumulation of plastic strain under asymmetric cyclic loading.

(4) The Principles of Elastoplasticity: The principles governing materials that exhibit both elastic (reversible) and plastic (permanent) deformation when subjected to stress.

(5) Homothetic: Refers to geometric transformations that expand or contract figures uniformly in all directions, preserving shape but not size.

(6) Anelastic: Describes a material behavior where strain lags behind stress, leading to time-dependent reversible deformation upon unloading.

(7) Cyclic Shakedown: A process in which a structure subjected to repeated loading cycles eventually stops accumulating plastic deformation and behaves elastically under further loading.

B. S-HARM Formulation: Using Gibbs Free Energy Function & Yield Function Approach (Rate Independent Method)

Derivation of HARM in series (S-HARM) based hyperplasticity framework according to the work of Houlsby et al. (2017) is presented here. There are different forms of energy potentials (energy functions) notably – Internal Energy (u), Helmholtz Free Energy (f), Enthalpy (h), and Gibbs' Free Energy (g). Only f and g are selected for derivation of the HARM constitutive model. Step-by-step derivation and explanation:

(1) Gibbs Free Energy Function:

The Gibbs free energy in series is given as;

$$g = -\frac{\sigma^2}{2H_0} - \sigma\left(\sum_{n=1}^{N_s}\alpha_n + \alpha_r\right) + \sum_{n=1}^{N_s}\frac{H_n}{2}\alpha_n^2$$

Where:
H_0: Initial modulus
σ: Stress
α_n: Internal strain variables (plastic strains)
α_r: Ratcheting strain
H_n: Hardening moduli for plastic strain components
(2) Derivatives of g:

$$\frac{\partial g}{\partial \sigma} = -\frac{\sigma}{H_0} - \sum_{n=1}^{N_s}\alpha_n - \alpha_r$$

$$\frac{\partial^2 g}{\partial \sigma^2} = -\frac{1}{H_0}$$

$$\frac{\partial g}{\partial \alpha_n} = -\sigma + H_n \alpha_n$$

$$\frac{\partial^2 g}{\partial \sigma \partial \alpha_n} = -1$$

$$\frac{\partial^2 g}{\partial \sigma \partial \alpha_r} = -1$$

$$\frac{\partial^2 g}{\partial \alpha_n^2} = H_n$$

$$\frac{\partial^2 g}{\partial \alpha_n \partial \alpha_m} = 0 \quad n \neq m$$

(3) Strain from Gibbs Free Energy:
This leads to;

$$\epsilon = -\frac{\partial g}{\partial \sigma} = \frac{\sigma}{H_0} + \sum_{n=1}^{N_s} \alpha_n + \alpha_r$$

(4) Back-Stresses:

$$-\dot{\bar{\chi}}_n = \frac{\partial^2 g}{\partial \sigma \partial \alpha_n}\dot{\sigma} + \frac{\partial^2 g}{\partial \alpha_n^2}\dot{\alpha_n}$$

$$\bar{\chi}_n = -\frac{\partial g}{\partial \alpha_n} = \sigma - H_n \alpha_n \qquad n = 1 \dots N_s$$

$$-\dot{\bar{\chi}}_r = \frac{\partial^2 g}{\partial \sigma \partial \alpha_r}\dot{\sigma}$$

$$\bar{\chi}_r = -\frac{\partial g}{\partial \alpha_r} = \sigma$$

(5) Yield Function:
The yield function is represented as;

$$y_n = |\chi_n| - k_n + R_n(|\chi_r| - |\sigma|) = 0$$

k_n: Yield stress threshold for each spring-slider unit
R_n: Ratcheting parameter for each spring-slider unit
(6) Plastic Strain Rates:
This leads to;
Flow rule

$$\dot{\alpha_n} = \lambda_n \frac{\partial y_n}{\partial \chi_n} = \lambda_n S(\chi_n)$$

Ratcheting Constraint

$$\dot{\alpha_r} = \sum_{n=1}^{N_s} \lambda_n \frac{\partial y_n}{\partial \chi_n} = \sum_{n=1}^{N_s} \lambda_n R_n S(\chi_r) = S(\sigma) \sum_{n=1}^{N_s} R_n |\dot{\alpha_n}|$$

Consistency Condition

$$\dot{y_n} = \frac{\partial y_n}{\partial \sigma}\dot{\sigma} + \sum_{m=1}^{N_s} \frac{\partial y_n}{\partial \chi_m}\dot{\chi_m} + \frac{\partial y_n}{\partial \chi_r}\dot{\chi_r} \sum_{m=1}^{N_s} \frac{\partial y_n}{\partial \alpha_m}\dot{\alpha_m} + \frac{\partial y_n}{\partial \alpha_r}\dot{\alpha_r} = 0$$

With Ziegler's orthogonality condition;

$$\chi_n = \bar{\chi}_n$$

And;

$$\frac{\partial y_n}{\partial \chi_m} = 0 \qquad m \neq n$$

We have the following when combining all the above equations for the model to obtain λ_n;

$$\frac{\partial y_n}{\partial \sigma}\dot{\sigma} - \frac{\partial y_n}{\partial \chi_n}\left(\frac{\partial^2 g}{\partial \sigma \partial \alpha_n}\dot{\sigma} + \frac{\partial^2 g}{\partial \alpha_n^2}\lambda_n \frac{\partial y_n}{\partial \chi_n}\right) - \frac{\partial y_n}{\partial \chi_r}\frac{\partial^2 g}{\partial \sigma \partial \alpha_r}\dot{\sigma} = 0$$

$$\lambda_n = \frac{\frac{\partial y_n}{\partial \sigma} - \frac{\partial y_n}{\partial \chi_n}\frac{\partial^2 g}{\partial \sigma \partial \alpha_n} - \frac{\partial y_n}{\partial \chi_r}\frac{\partial^2 g}{\partial \sigma \partial \alpha_r}}{\frac{\partial y_n}{\partial \chi_n}\frac{\partial^2 g}{\partial \alpha_n^2}\frac{\partial y_n}{\partial \chi_n}}\dot{\sigma}$$

Given:

$$\frac{\partial y_n}{\partial \sigma} = -R_n S(\sigma)$$
$$\frac{\partial y_n}{\partial \chi_n} = S(\chi_n)$$
$$\frac{\partial y_n}{\partial \chi_r} = R_n S(\chi_r)$$

Substituting into the partial derivatives:

$$\lambda_n = \frac{-R_n S(\sigma) - S(\chi_n).(-1) - R_n S(\chi_r).(-1)}{\left(S(\chi_n)\right)^2.H_n}\dot{\sigma}$$
$$\chi_n \neq 0$$
$$\lambda_n = \frac{-R_n S(\sigma) + S(\chi_n) + R_n S(\chi_r)}{(1).H_n}\dot{\sigma}$$
$$\lambda_n = \frac{S(\chi_n) + R_n(S(\chi_r) - S(\sigma))}{H_n}\dot{\sigma}$$

(7) Incremental Stress-Strain Relationship:

$$-\dot{\epsilon} = \frac{\partial^2 g}{\partial \sigma^2}\dot{\sigma} + \sum_{n=1}^{N_s}\frac{\partial^2 g}{\partial \sigma \partial \alpha_n}\dot{\alpha_n} + \frac{\partial^2 g}{\partial \sigma \partial \alpha_r}\dot{\alpha_r}$$
$$-\dot{\epsilon} = -\frac{\dot{\sigma}}{H_0} - \sum_{n=1}^{N_s}\dot{\alpha_n} - \dot{\alpha_r}$$
$$\dot{\epsilon} = \frac{\dot{\sigma}}{H_0} + \sum_{n=1}^{N_s}\dot{\alpha_n} + \dot{\alpha_r}$$

From here the following are obtained;

$$\dot{\sigma} = H_0\left(\dot{\epsilon} - \sum_{n=1}^{N_s}\dot{\alpha_n} - \dot{\alpha_r}\right)$$

Substituting the expressions for $\dot{\alpha_n}$ and $\dot{\alpha_r}$:

$$\dot{\sigma} = H_0\left(\dot{\epsilon} - \frac{1}{\mu}\sum_{n=1}^{N_s}\langle|\chi_n| - k_n + R_n(|\chi_r| - |\sigma|)\rangle \times (S(\chi_n) + R_n S(\chi_r))\right)$$

For small increments in δt:

The above equation can be represented in case of a small increment with the replacement of some derived results as;

$$\delta\sigma = H_0\delta\epsilon - \frac{H_0\delta t}{\mu}\sum_{n=1}^{N_s}\langle|\sigma - H_n\alpha_n| - k_n\rangle\,(S(\sigma - H_n\alpha_n) + R_n S(\sigma))$$

This latter formulation is very useful for incremental analysis implementation. Given the current state of σ and α_n as well as incremental strain $\delta\epsilon$ or incremental stress $\delta\sigma$ within a small time interval δt, then it is possible to solve $\delta\epsilon$ or $\delta\sigma$ directly.

(8) Updating Internal Variables:

Completion of the full solution also requires updating the internal variables. Thus, the set of equations completing the incremental update is clearly expressed below.

$$\delta\alpha_n = \frac{\delta t}{\mu}\langle|\sigma - H_n\alpha_n| - k_n\rangle S(\sigma - H_n\alpha_n) \qquad n = 1 \dots N_s$$

$$\delta\alpha_r = S(\sigma)\sum_{n=1}^{N_s} R_n\,|\delta\alpha_n|$$

(9) Complete Incremental Update:

$$\delta\sigma = H_0\left(\delta\epsilon - \sum_{n=1}^{N_s}\delta\alpha_n - \delta\alpha_r\right)$$

(10) Ratcheting Parameter:
Note that R_n is given as;

$$R_n = R_0\left(\frac{k_n}{k_U}\right)\left(\frac{\beta}{\beta_0}\right)^{-m_r}\left(\frac{|\sigma|}{k_U}\right)^{m_s}$$

R_0: Initial ratcheting parameter
k_U: Upper value of k_n
β, β_0: Hardening parameters
m_r, m_s: Exponents

C. P-HARM Formulation: Using Gibbs Free Energy Function & Yield Function Approach (Rate Independent Method)

Derivation of HARM in parallel (P-HARM) based hyperplasticity framework according to the work of Houlsby et al. (2017) is presented here. Step-by-step derivation and explanation:

(1) Gibbs Free Energy Function:

The Gibbs free energy in parallel is given as;

$$g = -\frac{\left(\sigma + \sum_{n=1}^{N_s} H_n\alpha_n\right)^2}{2E_0} - \sigma\alpha_r + \sum_{n=1}^{N_s}\frac{H_n}{2}\,\alpha_n^2$$

Where;

$$E_0 = \sum_{n=1}^{N_s+1} H_n$$

This function accounts for the energy stored due to both elastic and plastic strains, and the ratcheting strain.
(2) Strain from Gibbs Free Energy:
This leads to;

$$\epsilon = -\frac{\partial g}{\partial\sigma} = \frac{\left(\sigma + \sum_{n=1}^{N_s} H_n\alpha_n\right)}{E_0} + \alpha_r$$

(3) Back-Stresses:

$$\bar{\chi}_n = -\frac{\partial g}{\partial\alpha_n} = H_n\frac{\left(\sigma + \sum_{n=1}^{N_s} H_n\alpha_n\right)}{E_0} - H_n\alpha_n \qquad n = 1 \dots N_s$$

$$\bar{\chi}_n = H_n(\epsilon - \alpha_n - \alpha_r) \qquad n = 1 \dots N_s$$

$$\bar{\chi}_r = -\frac{\partial g}{\partial\alpha_r} = \sigma$$

The rest of the formulation follows very closely similar approach as in the HARM series formulation.
(4) Yield Function:
The yield function is represented as;

$$y_n = |\chi_n| - k_n + R_n(|\chi_r| - |\sigma|) = 0$$

(5) Plastic Strain Rates:
This leads to;

$$\dot{\alpha}_n = \lambda_n \frac{\partial y_n}{\partial \chi_n} = \lambda_n S(\chi_n)$$

$$\dot{\alpha}_r = \sum_{n=1}^{N_s} \lambda_n \frac{\partial y_n}{\partial \chi_n} = \sum_{n=1}^{N_s} \lambda_n R_n S(\chi_r) = S(\sigma) \sum_{n=1}^{N_s} R_n |\dot{\alpha}_n|$$

(6) Incremental Stress-Strain Relationship:
From here the following are obtained;

$$\dot{\sigma} = E_0 \left(\dot{\epsilon} - \sum_{n=1}^{N_s} \frac{H_n \dot{\alpha}_n}{E_0} - \dot{\alpha}_r \right)$$

Substituting the expressions for $\dot{\alpha_n}$ and $\dot{\alpha_r}$:

$$\dot{\sigma} = E_0 \left(\dot{\epsilon} - \frac{1}{\mu} \sum_{n=1}^{N_s} \langle |\chi_n| - k_n + R_n(|\chi_r| - |\sigma|) \rangle \times (S(\chi_n) + R_n S(\chi_r)) \right)$$

For small increments in δt:
The above equation can be represented in case of a small increment with the replacement of some derived results as;

$$\delta\sigma = E_0 \delta\epsilon - \frac{E_0 \delta t}{\mu} \sum_{n=1}^{N_s} \langle |\sigma - H_n \alpha_n| - k_n \rangle \, (S(\sigma - H_n \alpha_n) + R_n S(\sigma))$$

(7) Updating Internal Variables:
Completion of the full solution also requires updating the internal variables. Thus, the set equations completing the incremental update are clearly expressed below.

$$\delta\alpha_n = \frac{\delta t}{\mu} \langle |\sigma - H_n \alpha_n| - k_n \rangle S(\sigma - H_n \alpha_n) \qquad n = 1 \dots N_s$$

$$\delta\alpha_r = S(\sigma) \sum_{n=1}^{N_s} R_n |\delta\alpha_n|$$

(8) Complete Incremental Update:

$$\delta\sigma = E_0 \left(\delta\epsilon - \sum_{n=1}^{N_s} \frac{H_n \delta\alpha_n}{E_0} - \delta\alpha_r \right)$$

(9) Ratcheting Parameter:
Note that R_n is given as;

$$R_n = R_0 \left(\frac{k_n}{k_U} \right) \left(\frac{\beta}{\beta_0} \right)^{-m_r} \left(\frac{|\sigma|}{k_U} \right)^{m_s}$$

R_0: Initial ratcheting parameter
k_U: Upper value of k_n
β, β_0: Hardening parameters
m_r, m_s: Exponents

To avoid ambiguity with the dissipation function d, the incremental response has been represented as δ. These formulations extend the parallel and series HARM models, using Gibbs free energy and the yield function approach to handle complex ratcheting and plastic deformation behaviors in a rate-independent manner.

D. REDWIN Formulation for Unidirectional Loading

REDWIN formulation under unidirectional loads based on MSKH framework according to the work of Page et al. (2018) is presented here. The unidirectional formulation of the REDWIN model as per Page et al. (2018) is a precursor to the multidirectional formulation (Page et al., 2019a). The unidirectional formulation is very vital for model calibration based on the input load-displacement curves and the foundation's stiffness matrix.

(1) Generalized Load and Displacement Vectors
Here, implementation in two degrees of freedom (2-DOFs) is presented. Generalized load vector σ and work-conjugate generalized displacement vector ϵ is given as;

$$\sigma = \begin{bmatrix} M/D \\ H \end{bmatrix}; \qquad \epsilon = \begin{bmatrix} D.\theta \\ u \end{bmatrix}$$

(2) Plastic Work-done
The plastic work-done W^p is calculated as;

$$W^p = \int_0^{\theta^p} M.d\theta^p + \int_0^{u^p} H.du^p$$

(3) Incremental Contributions
Incremental contributions from elastic and plastic displacements are;

$$d\epsilon = d\epsilon^e + d\epsilon^p$$

Where ϵ^e and ϵ^p are the generalized elastic and plastic displacement respectively.
(4) Elastic Response
Elastic response in 2 degrees of freedom (DOFs) is given as;

$$\sigma = \boldsymbol{K}.\epsilon^e; \qquad \boldsymbol{K} = \begin{bmatrix} k_{11} & k_{12} \\ k_{21} & k_{22} \end{bmatrix}$$

Where $\boldsymbol{K}$ is the elastic stiffness matrix.
(5) Yield Criterion
The yield criterion f is given as;

$$f(\sigma, \alpha) = f(M/D, H, \alpha_M, \alpha_H)$$

Given an arbitrary number of yield surface i;

$$f_i(\sigma, \alpha_i) = \left(\frac{\left(\frac{M}{D} - \alpha_{M,i}\right).sin\beta + \left(H - \alpha_{H,i}\right).cos\beta}{b_i} \right)^2 + \left(\frac{-\left(\frac{M}{D} - \alpha_{M,i}\right).cos\beta + \left(H - \alpha_{H,i}\right).sin\beta}{a_i} \right)^2 - 1 = 0$$

Where;

$$\frac{a}{b} \approx \frac{a_i}{b_i}$$

(6) Flow Rule
Flow rule definition;
The flow rule defines the direction of the generalized plastic displacement increment dv^p.

$$d\epsilon^p = d\lambda.\frac{\partial \mathrm{g}}{\partial \sigma}$$

Here g in the flow rule formulation is the plastic potential surface. The flow rule equation becomes associative when g is equal to the yield surface f.
For each yield surface i;

$$d\epsilon_i^p = d\lambda_i.\frac{\partial f_i}{\partial \sigma}$$

Assuming Koiter's rule applied to the sum of plastic contributions from active yield surfaces gives;

$$d\epsilon^p = \sum_{i=1}^{j} d\epsilon_i^p = \sum_{i=1}^{j} d\lambda_i.\frac{\partial f_i}{\partial \sigma}$$

Where j indicates the number of active yield surfaces.
(7) Hardening Rule
Ziegler's KH rule;

$$d\alpha_i = d\mu_i.(\sigma - \alpha_i)$$

Where $d\mu_i$ is a function of the scalar $d\lambda_i$ defining the magnitude of $d\epsilon^p$ in the flow rule.
The hardening rule is reformulated as follows;

$$d\alpha_i = \boldsymbol{K}_i^p . d\epsilon^p = d\lambda_i . \boldsymbol{K}_i^p . \frac{\partial f_i}{\partial \sigma}$$

(8) Consistency Condition
The consistency condition assuming a single yield surface is given as;

$$df = \left(\frac{\partial f}{\partial \sigma}\right)^T . d\sigma + \frac{\partial f}{\partial \alpha} . \frac{\partial \alpha}{\partial \lambda} d\lambda = 0$$

$$df = \left(\frac{\partial f}{\partial \sigma}\right)^T . d\sigma + (-A d\lambda) = 0$$

Where A represents the plastic resistance. The above equation can be re-written as follows;

$$A . d\lambda = \left(\frac{\partial f}{\partial \sigma}\right)^T . d\sigma \approx f; \qquad f \approx A . d\lambda$$

The consistency condition is very useful to obtain $d\lambda_i$ for a given yield surface i.
For an arbitrary number of active yield surface(s) j, the consistency condition can be represented as;

$$f = \begin{bmatrix} f_1 \\ f_2 \\ \vdots \\ f_j \end{bmatrix} \approx \begin{bmatrix} a_{11} + A_1 & a_{12} & \cdots & a_{1j} \\ a_{21} & a_{22} + A_2 & \cdots & a_{2j} \\ \vdots & \vdots & \ddots & \vdots \\ a_{j1} & a_{j2} & \cdots & a_{jj} + A_j \end{bmatrix} = \Xi . d\lambda$$

Where;

$$a_{ik} = \left(\frac{\partial f_i}{\partial \sigma}\right)^T . \boldsymbol{K} . \left(\frac{\partial g_k}{\partial \sigma}\right)$$

And;

$$A_k = \left(\frac{\partial f_k}{\partial \sigma}\right)^T . \boldsymbol{K}_k^p . \left(\frac{\partial g_k}{\partial \sigma}\right)$$

Step-by-Step Numerical Implementation Procedure

Numerical implementation of the macro-element model in incremental response follows the relation;

$$\sigma = \sigma_0 + \Delta\sigma = \sigma_0 + \boldsymbol{K} . \Delta\epsilon^e = \sigma_0 + \boldsymbol{K} . (\Delta\epsilon - \Delta\epsilon^p)$$

Where the generalized force at the beginning of the step is σ_0. Enforcement of $f \approx 0$ is enabled at the end of the step. If $f \approx 0$ is not achieved at the end of the step after a certain number of iterations, sub-stepping algorithm is enforced.

For easy implementation of the macro-element model, the elliptical yield surface is transformed into a circular yield surface via a change in coordinate system with yield criterion formulation assuming circular shape, and then to be re-transformed back into elliptical shape after computation completion via transformation of the computed generalized forces back to the elliptical coordinate system.

Thus, the formulation of the yield criterion done assuming a circular shape with radius defined a stress invariant which is a function two stress components. This circular yield surface is presented further under the multidirectional REDWIN implementation.

$$\sigma' = R . \sigma = \begin{bmatrix} cos\beta & a/bsin\beta \\ sin\beta & a/bcos\beta \end{bmatrix} . \sigma$$

Where R is the linear transformation matrix, transformed generalized force vector is σ'. The orientation β and elliptical yield surface shape/sizing ratio a/b is assumed to be constant (homothetic) for each of the surfaces for the above equations and computation to be valid. This homothetic condition is true for certain load levels, say low to moderate load intensity; but this may not hold in certain high load intensity which could result in each yield surface shape and orientation to vary. The transformed incremental generalized displacement $\Delta\epsilon'$ is given as;

$$\Delta\epsilon' = (R^T)^{-1}.\Delta\epsilon$$

It is worth noting that the plastic work done remains constant (does not change) irrespective of changes in coordinate systems. The incremental plastic work done is given as;

$$\Delta W^p = (\sigma')^T.\Delta\epsilon'_p = (R.\sigma)^T.((R^T)^{-1}.\Delta\epsilon_p)$$

$$\Delta W^p = \sigma^T.R^T.(R^T)^{-1}.\Delta\epsilon_p$$

$$\Delta W^p = \sigma^T.\Delta\epsilon_p$$

In summary, solving the constitutive equation requires a transformation of $\Delta\epsilon$ and loads from the previous load step σ_0 via R and $(R^T)^{-1}$. The solution to the constitutive relation is done in the transformed coordinate system, the computed generalized forces are transformed back to the elliptical coordinate system.

E. Description of Programming Functions & Mathematical Equations

(1) Elastic Stiffness Matrix

This subroutine constructs the elastic stiffness matrix using the provided input stiffness coefficients. The subroutine takes four input parameters representing the stiffness coefficients and assembles them into a 4x4 elastic stiffness matrix. The matrix is fundamental in modeling the elastic behavior of the foundation under applied loads. The elastic stiffness matrix characterizes the offshore soil foundation's resistance to deformation under applied loads in different directions and interactions between these directions. The construction of the stiffness matrix ensures that both diagonal and cross-coupling terms are accurately represented, providing a comprehensive elastic model for subsequent analyses.

The diagonal coefficients in the stiffness matrix typically represent the foundation's resistance to deformation along the principal axes. These are the direct stiffness components describing how a displacement or rotation in a particular direction affects the force or moment in that same direction respectively. Here, K11 and K22 are translational stiffness components representing the stiffness in the x-direction and y-direction respectively. Similarly, K33 and K44 are rotational stiffness components in the x-direction and y-direction respectively.

The cross-coupling coefficients i.e. off-diagonal coefficients in the stiffness matrix represent the interaction between different types of displacements and forces or moments. They describe how a displacement or rotation in one direction affects the force or moment in a different direction.

Here, the K12 and K21 represent the coupling between translational and rotational components. K12 and K21 coefficients describe the coupling between the displacement in the x and y directions and the moments about the y and x directions respectively. Physically, it indicates how much force in the x and y directions is required to produce a unit rotation about the y and x axes respectively, or vice versa. On the other hand, –K12 and –K21 terms represent the coupling between the displacement in the y and x directions and the forces in the x and y directions respectively. It indicates how much force in the y and x directions are required to produce a unit displacement in the x and y directions respectively, but with an opposite effect due to the negative sign.

The stiffness matrix can be used to predict how the foundation will respond to complex loading conditions. For instance, translational loads say forces applied horizontally or vertically to the foundation can cause it to move or tilt, while rotational loads say moments applied to the foundation can cause it to twist or rotate. However, coupled loads which is the combinations of forces and moments that interact usually result in complex deformations of the foundation. A detailed understanding of the stiffness matrix helps in designing and analyzing the foundation's performance, ensuring it can withstand operational and environmental loads. This is the kind of load typically experienced by the OWT foundation. Therefore, by accurately constructing and utilizing the elastic stiffness matrix, engineers can better understand and predict the behavior of the foundation under various loading scenarios, ensuring stability and integrity.

The matrix is a 4 x 4 elastic stiffness matrix **K** using the provided stiffness coefficients K_{11}, K_{12}, K_{21} and K_{22}.

$$\boldsymbol{K} = \begin{pmatrix} K_{11} & 0 & 0 & K_{12} \\ 0 & K_{11} & -K_{12} & 0 \\ 0 & -K_{21} & K_{22} & 0 \\ K_{21} & 0 & 0 & K_{22} \end{pmatrix}$$

$$K_{ij} = \begin{cases} K_{11} & for\ i = j = 1{,}2 \\ K_{22} & for\ i = j = 3{,}4 \\ K_{12} & for\ (i,j) = (1{,}4) \\ K_{21} & for\ (i,j) = (4{,}1) \\ -K_{12} & for\ (i,j) = (2{,}3) \\ -K_{21} & for\ (i,j) = (3{,}2) \\ 0 & Otherwise \end{cases}$$

(2) Force and Displacement Interpolation

The force interpolation subroutine computes the interpolated force value for a given displacement query point. The interpolation is based on a piecewise linear relationship between a set of given displacements and their corresponding forces using a linear interpolation approach. The query displacement has to be within the range of the input displacement values, otherwise, an error is raised indicating that the value to interpolate is outside the input range. Similarly, the displacement interpolation subroutine does the same thing as the force interpolation subroutine but in reversed order – the force query point is considered instead of the displacement query point.

In the context of the CLAP model, given a plastic displacement (not rotation) due to moment and given another plastic displacement value due to force, a forecast or prediction can be done to obtain an equivalent moment value to reproduce the plastic displacement due to force, and vice-versa.

Generally, the force interpolation function allows the determination of the force corresponding to a given displacement and is useful for predicting the load on the foundation based on observed or expected displacements. Conversely, this function allows the determination of the displacement corresponding to a given force and is useful for predicting how much the foundation will move or deform under a specific load.

(3) Read Stiffness Parameters

This subroutine reads stiffness settings and data from a specified input text file. This file contains several stiffness coefficients that define the stiffness characteristics of the OWT foundation and other parameters like the specified number of yield surfaces, number of iteration limits, and convergence tolerance required for the model.

(4) Compute Contours Angle

This subroutine calculates the angle of the contours of plastic displacements or plastic rotations in the plane defined by the horizontal force (x-axis) and the moment (y-axis). It computes the angle between these contours and the x-axis in radians. The angles for each of the contours are calculated and the average is taken.

Interpolation is performed between axes to determine the points that define each contour based on force interpolation to find the corresponding moment value that gives plastic displacement due to force (u_{HP}) equal to plastic displacement due to moment (u_{MP}) for each of the given horizontal forces (H) and u_{HP} in the horizontal axis, or the corresponding horizontal force value that gives u_{HP} equal to u_{MP} for each of the given moments (M) and u_{MP} in the vertical axis.

These plastic displacement/rotation contours represent the relationship between plastic deformations (displacement or rotation) and applied loads (horizontal force and moment). The angle of these contours provides insight into the coupling effects between different loading directions. The calculated angles help in understanding the directional dependency of the foundation's plastic behavior, which is crucial for accurately modeling and predicting the foundation's response under

complex loading conditions. This is particularly important for designing foundations that can withstand multidirectional and cyclic loads.

This finds the angle of the contours in the horizontal load-moment plane by interpolating the required values and then calculating the angles and their average. This is expressed mathematically as:

$$\emptyset_u = \frac{1}{N-2}\sum_{i=3}^{N} \arctan\left(\frac{H_i}{M_i}\right)$$

Where N is the number of data points in the force-displacement curve or the moment-rotation curve.

(5) Compute Ellipse Parameters

This subroutine calculates the parameters of an ellipse (b/a and β) that represent the yield surface in the horizontal force-moment plane. These parameters are derived from the angles of the contours of plastic displacement and plastic rotations. The ratio b/a is the ratio between the major and minor axis of the elliptical yield surfaces defining the shape of the yield surface whether elliptical or circular, while β is the angle between the vertical axis and the major axis of the elliptical yield surfaces defining the orientation of the yield surface, and indicating the directional dependency of the yield surface.

If the absolute difference in the average angle between the contours of plastic displacement ($\emptyset_u$) and the plastic rotation ($\emptyset_\theta$) with respect to the horizontal axis in the horizontal force-moment plane is less than the specified tolerance (tol), then this means that the contours are nearly parallel, and an error is raised. This condition is unreasonable and not desirable for the computation process. These angles $\emptyset_u$ and $\emptyset_\theta$ represent the orientation of the yield contours in the force-moment plane. The contours depict how the plastic deformation or rotation evolves under combined loading conditions. The subroutine ensures the physical validity of the input angles and the resulting ellipse parameters, hence, is crucial for defining the yield surface in the force-moment plane.

Given the average $\emptyset_u$ and $\emptyset_\theta$, the ellipse parameters $\frac{b}{a}$ and β are computed.

$$C_1 = (tan\emptyset_u tan\emptyset_\theta - 1)^2 + 4\tan^2\emptyset_u$$

$$C_2 = tan\emptyset_u tan\emptyset_\theta + 1$$

$$C_3 = tan\emptyset_u tan\emptyset_\theta - 1$$

$$\alpha = -0.5.\arctan\left(\frac{2tan\emptyset_u}{C_3}\right)$$

Valid for $\alpha \geq \emptyset_u$ or $\alpha \leq \emptyset_\theta$

$$\beta = \frac{\pi}{2} - \alpha$$

$$\frac{b}{a} = \sqrt{\frac{C_2 - \sqrt{C_1}}{C_2 + \sqrt{C_1}}}$$

Valid for $\emptyset_\theta > \emptyset_u$

(6) Matrix Transformation 2 x 2

This computes the transformation matrix R for transitioning from the original axes at the mudline to a transformed axes system, its transpose R^T, inverse R^{-1}, and the transpose of the inverse $(R^{-1})^T$. The formulation is 2×2 matrix. The mathematical formulation given the parameters $\frac{b}{a}$ and β are presented below:

Transformation matrix R in 2×2:

$$R = \begin{pmatrix} sin\beta & cos\beta \\ -\left(\frac{b}{a}\right)cos\beta & \left(\frac{b}{a}\right)sin\beta \end{pmatrix}$$

Transpose of R:

$$R^T = \begin{pmatrix} sin\beta & -\left(\frac{b}{a}\right)cos\beta \\ cos\beta & \left(\frac{b}{a}\right)sin\beta \end{pmatrix}$$

Inverse of R:

$$R^{-1} = \begin{pmatrix} sin\beta & -\left(\frac{a}{b}\right)cos\beta \\ cos\beta & \left(\frac{a}{b}\right)sin\beta \end{pmatrix}$$

Transpose of the inverse of R:

$$(R^{-1})^T = \begin{pmatrix} sin\beta & cos\beta \\ -\left(\frac{a}{b}\right)cos\beta & \left(\frac{a}{b}\right)sin\beta \end{pmatrix}$$

(7) Matrix Transformation 4 x 4

Similar to the case of the 2×2 matrix, this extends the transformation matrix calculation to a 4×4 transformation matrix R to move from the original axes at the mudline to a transformed axes system. Additionally, it calculates the transpose of R (R^T), the inverse of R (R_{inv}), and the transpose of the inverse of R (R_{T_inv}).

The mathematical formulation given the parameters $\frac{b}{a}$ and β are presented below:

The transformation matrix R:

$$R = \begin{pmatrix} sin\beta & 0 & 0 & cos\beta \\ 0 & \sin(-\beta) & \cos(-\beta) & 0 \\ 0 & -\left(\frac{b}{a}\right)\cos(-\beta) & \left(\frac{b}{a}\right)\sin(-\beta) & 0 \\ -\left(\frac{b}{a}\right)cos\beta & 0 & 0 & \left(\frac{b}{a}\right)sin\beta \end{pmatrix}$$

Transpose of R:

$$R^T = \begin{pmatrix} sin\beta & 0 & 0 & -\left(\frac{b}{a}\right)cos\beta \\ 0 & \sin(-\beta) & -\left(\frac{b}{a}\right)\cos(-\beta) & 0 \\ 0 & \cos(-\beta) & \left(\frac{b}{a}\right)\sin(-\beta) & 0 \\ cos\beta & 0 & 0 & \left(\frac{b}{a}\right)sin\beta \end{pmatrix}$$

Inverse of R:

$$R^{-1} = \begin{pmatrix} sin\beta & 0 & 0 & -\left(\frac{a}{b}\right)cos\beta \\ 0 & \sin(-\beta) & -\left(\frac{a}{b}\right)\cos(-\beta) & 0 \\ 0 & \cos(-\beta) & \left(\frac{a}{b}\right)\sin(-\beta) & 0 \\ cos\beta & 0 & 0 & \left(\frac{a}{b}\right)sin\beta \end{pmatrix}$$

Transpose of the inverse of R:

$$(R^{-1})^T = \begin{pmatrix} sin\beta & 0 & 0 & cos\beta \\ 0 & \sin(-\beta) & \cos(-\beta) & 0 \\ 0 & -\left(\frac{a}{b}\right)\cos(-\beta) & \left(\frac{a}{b}\right)\sin(-\beta) & 0 \\ -\left(\frac{a}{b}\right)cos\beta & 0 & 0 & \left(\frac{a}{b}\right)sin\beta \end{pmatrix}$$

These matrices are used to transform coordinate systems. Specifically, they are used to convert from the original axes at the mudline to a new transformed coordinate system – which is essential for transforming between different coordinate systems (circular and elliptical) in the model.

(8) Soil (Sand) Calibration for Kp & S

The subroutine calibrates the stiffness (K_P) and strength (S) of each yield surface in the MSKH model based on the von Mises criterion with circular yield surfaces. It uses the force-displacement curve(s) to determine these parameters. The subroutine ensures the input force-displacement curve is monotonically increasing. If a non-monotonic behavior is detected, the force is slightly adjusted. This curve represents the relationship between the applied force and the resulting displacement of the system. Ensuring it is monotonically increasing is crucial for accurate interpolation and calibration. Load intervals are created with the total range of force is divided into Ns intervals, and the corresponding maximum force level for each interval is calculated. These load intervals divide the total load range into segments, thereby facilitating a step-by-step calibration of the model parameters. Also, for each load level the corresponding displacement is found using the interpolation subroutine for displacement.

For calculating K_P and S – the tangent stiffness K_T for each of the segments (piece-wise curve) is first calculated. K_P of each yield surface, is derived from the tangent stiffness, while S of each yield surface, is set to the load level. A section of the subroutine is created to handle numerical instability by adjusting the load intervals. This section checks if the ratio of stiffness between yield surfaces is excessively large and adjusts the intervals if necessary to avoid numerical issues. It recalibrates if an adjustment is made. Based on the analyses conducted so far, this section of the subroutine proved not to be very effective.

The stiffness of the last spring is set to zero to indicate that the model is outside its calibration range, and it 'fails' at the maximum force. The stiffness (K_P) reflects the resistance of each yield surface to deformation under load. The calibration ensures that the stiffness values accurately represent the physical behavior of the foundation, while the strength (S) indicates the load level at which each yield surface yields or fails. This helps in understanding the progressive failure behavior of the system.

In terms of application, this subroutine is particularly useful in calibrating models for foundations that exhibit plasticity such as sands in geotechnical engineering. It ensures that the model parameters are tuned to match observed force-displacement behavior, leading to more accurate predictions of foundation response under loading conditions. In OWT foundations, calibrating these parameters helps in designing foundations that can withstand the complex loading conditions experienced in marine environments, enhancing the reliability and safety of the structures.

(9) MSKH Model Calibration

The subroutine is created to read a table of forces and displacements from a text file containing moment and horizontal force data along with corresponding displacements and rotations, calibrate the MSKH model and determine the necessary parameters like S and K_P in the transformed coordinate for describing the foundation's plastic behavior under cyclic loading conditions. The steps followed are described below.

Moment and horizontal force data, including corresponding displacements and rotations are read. These are the moment, horizontal displacement, and rotation for zero horizontal load, as well as the horizontal force, horizontal displacement, and rotation for zero moment. The coefficients of the elastic flexibility matrix from the given stiffness matrix components are computed. The plastic displacements and plastic rotations are calculated by subtracting the elastic contributions – this helps to isolate the plastic behavior. If negative values are obtained for the plastic displacements and rotations, these are set to zero. The angles of plastic horizontal displacement and rotation contours are calculated, and the ellipse orientation β and shape based b/a the ratio is estimated.

The load-displacement curves are transformed to a new axis system to obtain the hardening curve using the calculated ellipse parameters and transformation matrices – these transformations align the data with a more convenient reference frame, improving the efficiency of the analyses. The vectors for horizontal force and plastic displacement or moment and corresponding plastic displacements are created. The sand calibration subroutine is called to calibrate the MSKH model based on the geometrically transformed data – this helps to predict the material response under cyclic loads.

This subroutine is a crucial part of the CLAP model as it calibrates the MSKH model based on the input data. The calibrated model can then be used to simulate the behavior of OWT foundations, accounting for the complexities of multidirectional loading and cyclic effects. The calibration process account for the unique characteristics of the foundation, ensuring that the model accurately represents the real-world behavior of the foundation. The calibrated model is crucial for predicting the long-term performance and stability of OWT foundations.

Flexibility Matrix

The flexibility matrix is the inverse of the stiffness matrix. Thus, the off-diagonal terms of the inverse of a 2x2 matrix are negations of the off-diagonal terms of the original matrix, divided by the determinant of the original matrix. In this case, K12 and K21 are the off-diagonal terms of the stiffness matrix, so –K12 and –K21 are the corresponding off-diagonal terms of the flexibility matrix.

The elastic flexibility matrix calculation:

$$\boldsymbol{A} = \begin{bmatrix} A_{11} & A_{12} \\ A_{21} & A_{22} \end{bmatrix} = \begin{bmatrix} \dfrac{K_{22}}{K_{11}K_{22} - K_{12}K_{21}} & \dfrac{-K_{12}}{K_{11}K_{22} - K_{12}K_{21}} \\ \dfrac{-K_{21}}{K_{11}K_{22} - K_{12}K_{21}} & \dfrac{K_{11}}{K_{11}K_{22} - K_{12}K_{21}} \end{bmatrix}$$

(10) Hyper-Ellipsoid Yield Function

This function calculates the equivalent value of the 4D ellipsoid function which is the hypersphere function f in the transformed coordinate system for a given strength S (yield surface radius), transformed force σ_T and the transformed position of the yield surface (back-stress) α_T.

The second stress invariant J2 is calculated as the sum of the squares of the differences ($\Delta\sigma_T$) between σ_T and α_T. If the absolute value of S is significantly larger than the specified tolerance, f is computed as the difference between the Euclidean norm of the $\Delta\sigma_T$ and S – mathematically equivalent to calculating f as the square root of J2 minus S given that J2 represents the sum of the squares of the components of $\Delta\sigma_T$.

(a) Euclidean Norm of $\Delta\sigma_T$:

$$\|\Delta\sigma_T\| = \sqrt{\Delta\sigma_{T1}^2 + \Delta\sigma_{T2}^2 + \Delta\sigma_{T3}^2 + \Delta\sigma_{T4}^2}$$

(b) J2 as Stress Invariant:

$$J2 = \Delta\sigma_{T1}^2 + \Delta\sigma_{T2}^2 + \Delta\sigma_{T3}^2 + \Delta\sigma_{T4}^2$$

(c) Relationship between Euclidean Norm and J2:

$$\|\Delta\sigma_T\| = \sqrt{J2}$$

(d) Computing f:

$$f = \|\Delta\sigma_T\| - S = \sqrt{J2} - S$$

The J2 represents the second invariant of the deviatoric stress tensor, a crucial concept in plasticity theory, particularly for materials that follow the von Mises yield criterion. This stress constant is critical in plasticity theory as it characterizes the yielding and flow rules, and it provides a scalar measure of the stress state. The Euclidean norm of $\Delta\sigma_T$ gives the magnitude of the stress vector in the transformed coordinate system.

The subroutines ensure that f quantifies the difference between the current state and the yield surface, which is essential for determining whether the material has yielded and by how much. It determines whether a given load lies inside, outside, or on the yield surface. The value f indicates the distance from the load point to the yield surface in the transformed coordinate system, which is essential for understanding the plastic behavior of the foundation.

(11) Compute Flow Potential Gradient

This subroutine computes the derivative of the yield function f with respect to the transformed load σ_T. If absolute J2 is non-zero, the derivative of f with respect to σ_T (stress tensor) is computed for each component of the vector $\Delta\sigma_T$. This subroutine provides the sensitivity of the yield function with respect to the load variations. The computed derivative is crucial for numerical integration schemes used in the constitutive equations of the HARM-REDWIN model, helping to update the state variables accurately. Likewise, J2 plays a pivotal role in determining the magnitude of the stress state and its direction in the stress space.

The yield function derivative:

$$\frac{\partial f}{\partial \sigma_{T_i}} = \frac{\Delta\sigma_{T_i}}{\sqrt{J_2}} \qquad if \qquad |J_2| > 0$$

(12) Compute Plastic Stiffness Matrix

This subroutine constructs the plastic stiffness matrix K_{Pl} for a single yield surface. It contains the parameters K_{Pl} and K_P which is the plastic stiffness associated with the yield surface. Here K_{Pl} is initialized as a zero matrix and then the diagonal elements are populated with K_P.

The K_{Pl} matrix represents the foundation's stiffness in the plastic regime. By constructing this matrix, the subroutine ensures that the plastic response is correctly incorporated into the overall stiffness of the foundation, which is essential for accurate macro-element analysis of the foundation's behavior under load. The diagonal form of the matrix indicates that the plastic stiffness is the same in all principal directions, assuming isotropic plastic behavior.

Generally, the 3 subroutines for the computation of the yield function (yield criterion), the gradient of flow potential (or the yield function due to the associative flow rule) and the plastic stiffness matrix collectively aid in modeling the plastic behavior of the foundation, particularly under complex loading conditions, by accurately computing the yield function, its derivatives, and the plastic stiffness matrix.

F. Challenges in Implementing & Improving the CLAP Model

Only a few of the most important challenges faced by the author in implementing and improving the CLAP model are presented here.

(1) Calibrate Sand Subroutine

Major numerical challenges in running the CLAP model are traced to this subroutine. The subroutines meant to calibrate nonlinear load-displacement curves but well robust in the event of presence of nearly linear (or linear) segments in the curve.

Typically, each spring-slider unit in series based on the Iwan (Iwan, 1967) model represents a yield surface. Also, the K_P (stiffness) value is supposed to decrease continuously from the value obtained after the first spring-slider unit has yielded to zero after the nth yield surface has yielded. But the challenge is that instead of K_P to be decreasing, it is oscillating. This is a numerical instability problem in the implementation of the subroutine for the calibration process.

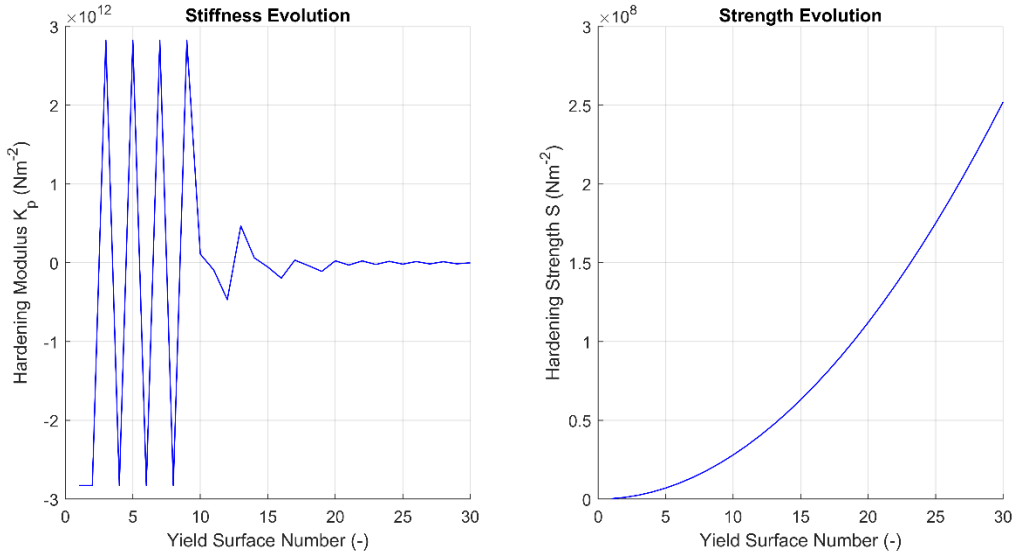

Figure F. 1. K_P vs N_s Plot in the Original Coordinate (N_s = 30).

The oscillation in the stiffness K_P values mostly is a result of the input force-displacement curve being almost linear in some regions, leading to numerical instability. There also the possibility of having multiple spring-slider units (yield surfaces) positioned at locations where the force-displacement curve is nearly linear which can lead to oscillations or instability in the stiffness values. In these regions, small variations in displacement can cause large variations in calculated stiffness, which can result in numerical instability. The specified number of yield surface N_s discretizes the force-displacement curve for the monotonic load response (back-bone curve). The larger the number specified, the smoother the response curve will be. This is analogous to FEA discretization for a beam in 1D. Three (3) specific culprits to look out for causing the instability comes from the following:

- Linear (or nearly linear) segments in the input curve.
- Errors or inaccuracies arising from the displacement interpolation.
- Insufficient data points relative to the number of yield surfaces specified.

In the case of linearity in the input curve segment(s) when part(s) of the force-displacement curve are almost linear, the differences in the displacement between successive points become very small. This can cause the calculated tangent stiffness (K_T) to become very large or unstable, leading to oscillations in K_P. Also, interpolation of displacement values at specific force levels could introduce numerical error or inaccuracies especially if the force-displacement data points are sparse or have large gaps. Furthermore, having more yield surfaces (N_s) than data points (N) can make the calibration

sensitive to small changes in the input data, leading to oscillations in the derived stiffness values. Possible ways to improve the numerical stability is to do one or more of the following:

- Smoothening the input force-displacement curve.
- Numerical regularization.
- Introducing significant N with respect to N_s.
- Load intervals adjustment.
- Weighted averaging.
- Introducing more efficient interpolation algorithms and validation of interpolated values.

A smoothing algorithm based on a simple moving average (or even spline smoothing) can be applied to the force-displacement curve to reduce the effects of the linear segments and make the curve more continuously differentiable. A very small constant can be introduced to the denominator (change in displacement) in the calculation of the tangent stiffness (K_T) to prevent extremely large values when the displacement difference is very small or insignificant – this called numerical regularization.

Increasing the number of data points in the force-displacement curve can provide more detailed information and reduce the impact of any linear segments. Also, recalculating the load intervals to avoid regions where the input curve is nearly linear can be done by dynamically adjusting the intervals based on the slope of the curve, thus, ensuring a monotonically increasing force-displacement curve. Weighted averaging of the obtained stiffness values over adjacent intervals can be utilized to smooth out oscillations. Furthermore, a more efficient displacement interpolation algorithm can be introduced, and the interpolated displacement values validated to ensure that they are accurate and do not introduce errors. This is because if the interpolation subroutine used to find the displacements corresponding to the load levels is not handling nearly linear segments well, it can also introduce errors.

To achieving a more stable calibration of the stiffness values, the author has focused on replacing the existing force and displacement interpolation subroutines with more robust and efficient algorithms. The load intervals adjustment mechanism in the code is maintained while a significant number of data points (N) with respect to N_s is always ensured. Number of yield surfaces N_s = 4 is unconditionally stable because the K_P values under this state continuously decrease with each yielding of the surface.

This numerical instability has been existing under the pure REDWIN model. The NGI team has implemented some significant fixes to improve the stability of the REDWIN model by including an RDP (Ramer–Douglas–Peucker) algorithm linked to the subroutine coupled with a new subroutine that updates the flexibility matrix. Though, this update appeared to bring some stability to the REDWIN model it has its deficiencies as well. The changes through the RDP algorithm automatically overwrite the initially specified number of yield surfaces. The algorithm updates this value depending on the number of the final optimized data point for the force-displacement curve(s). Furthermore, compared to the original state of the REDWIN code, these changes worsened the numerical instability of the CLAP implementation with the introduction of ratcheting.

With these observations, the author focused on improving the original state of the REDWIN code such that numerical instability is minimized for the CLAP model. A twin subroutine that is stable for the same purpose has also been implemented with some modifications in the way K_P is generated based on the Iwan (Iwan, 1967) formulation for springs in series. A MATLAB code snippet showing an alternative implementation that fits into the subroutine has been included:

```
% Calculate the stiffness and strength of each yield surface

    % Ns: Number of yield surfaces
    % sumKp: Sum of the inverse of the tangent stiffness
    % Kt: Tangent stiffness of load interval k
    % Fmaxk, dispk: Load and displacements level at the end of the interval k
    % S, Kp: Radius (strength) and stiffness of each yield surface
```

```
sumKp = 0; % Sum of the inverse of the stiffness from 1 to k-1
Kp = []; % Stiffness of each yield surface
for k = 1:Ns - 1
   if abs(dispk(k+1) - dispk(k)) <= 0
      Kt(k) = 1.0e20;
   else
      Kt(k) = (Fmaxk(k+1) - Fmaxk(k)) / (dispk(k+1) - dispk(k));
   end
   if k == 1
      Kp_0 = Kt(k);
   end
   if abs(1/Kt(k) - sumKp) <= 1e-20
      Kp(k) = Kt(k);
   else
      if Kp_0 == Kt(k) || abs(sum(1./Kp)) <= 1e-20
         Kp(k) = Kt(k);
      else
         Kp = [Kp, (inv(1/Kt(k) - (sum(1./Kp) + 1/Kp_0)))];
      end
   end
   sumKp = sumKp + (1/Kp(k));
   S(k) = Fmaxk(k);
end
Kp(Ns) = 0; % The stiffness of the last spring is zero
S(Ns) = Fmaxk(Ns); % The strength of the last yield surface
```

As earlier stated, in the computation of tangent stiffness, if the displacement difference is very small (nearly linear segment), the tangent stiffness can become extremely large, leading to numerical instability. Likewise, in the computation of spring stiffness, it involves the inverse of tangent stiffness. If the tangent stiffness is very large, the inverse becomes very small which can cause oscillations in the generated values for spring stiffness.

A conditional statement has been added to take into account the situation whereby Kp heads to infinity caused when Kp_0 value equals Kt(k) value, and sum(1./Kp) equals 0.

(2) Direct Solver for Linear Algebraic Equations

The computation of the incremental plastic multiplier is done by iteratively solving the system of equations:

$$f = A.d\lambda$$

This is done iteratively using the linear algebraic computation subroutine.

The constraint in the equation is the plastic resistance matrix A relating f with $d\lambda$. The matrix is prone to singularity. It is an ill-conditioned, singular or nearly singularity matrix depending on the selected number of yield surfaces in the MSKH model.

To determine the best solver implementation approach for the matrix, four key matrix properties to assess the nature of the matrix are checked. These are:

- Degree of singularity;
- Symmetrical/non-symmetrical;
- Positive/semi-positive/non-positive definite, and
- If sparse/dense (sometimes it's sparse during iteration).

To assess the degree of singularity, both the condition number and the determinant where checked. The condition number is at infinity while the determinant is zero both indicating matrix singularity. The matrix is approximately symmetric depending on the tolerance i.e. it is non-symmetrical within a tolerance value of 1×10^{-10} and symmetrical within a tolerance value of 1×10^{-5}. With the matrix accepted as been symmetric, Eigen value approach was adopted to assess the matrix definiteness indicating that the matrix is indefinite type. Also, a sparse matrix check showed that it is not sparse.

Following the above matrix properties, several techniques have been tried indicating that direct solvers or conventional linear algebraic solvers are not capable of handling such computation. An iterative solver like the preconditioned conjugate gradient (PCG) approach is quite suitable for such a matrix. However, a more accurate and robust solver based on the least-square approach is implemented and adopted to effectively handle the equation and ensure accurate computation of the incremental plastic multiplier, which in turn leads to accurate force or displacement computation at the end of the incremental step.

This least-square solver approach is particularly efficient in dealing with underdetermined or rank-deficient systems of linear equations. It computes the minimum-norm least-squares solution to the linear system $f = A.d\lambda$, where A is the matrix of coefficients i.e. the plastic resistance matrix and $d\lambda$ is the incremental plastic multiplier vector of observed values or outcomes.

Table F. 1. Comparison of the PCG and Least-Square-based Solvers for CLAP Model.

Preconditioned Conjugate Gradient (PCG)	Least Square Approach
Efficiency (Speed)***	Accuracy***
Accuracy is limited and varies depending on the nature of the load-displacement calibration inputs	Efficiency is Moderate

The asterisks indicate the strength of each solver.

(3) Frequency-Dependent Approach for Applied Loads

Convergence in the incremental response of the constitutive model depends not only on the nature of the applied load but also on the sampling frequency Fs and frequency of vibration F of the signals. The higher the frequency of the signal, the higher the sampling frequency required to ensure convergence and vice-versa. Likewise, the number of prescribed yield surface N_s is very important. Increasing the N_s value results will require a geometrical increment in Fs for a given signal frequency especially in the case of displacement-controlled mode, hence, increased computation time. An arbitrary number of N_s can be used for the CLAP model provided the desired signal is tuned correctly with F and Fs. However, the minimum number of N_s required to obtain smooth response curves for the constitutive model is 15. This minimum value is found to be optimal and has been used in all the simulations conducted in this project.

(4) Newton-Raphson Algorithm for Force-Controlled Simulation

Below is a MATLAB code snippet for a simple Newton's optimization algorithm.

```
Fx = Fx_Wave;
Fy = Fy_Wave + F_Wind;

   % Optional for visualization
   Force_Disp_Fx = zeros(length(Fx), 2);
   Force_Disp_Fy = zeros(length(Fy), 2);

   % Initialization
   Disp = zeros(6, 1); % Global displacement vector in 6 DOF Format
```

```
% Force-controlled analysis using the Newton-Raphson method
tol = 1e-5; % Convergence tolerance
max_iter = 1000; % Maximum number of iterations

fprintf(fid1, 'Force-Controlled Analysis\n');
fprintf(fid1, '  ForceX      ForceY    DispX    DispY    RotationX    RotationY\n');

for i = 1:length(Fx)
    % F1_GLOB = [Fx(i); 0; 0; 0; My(i); 0]; % Global force vector in 6 DOF Format
    F1_GLOB = [Fx(i); Fy(i); 0; 0; 0; 0]; % Global force vector in 6 DOF Format

    U1 = Disp; % Initial guess (Trial) for displacement
    iter = 0;
    res = inf;

    while (norm(res) > tol) && (iter < max_iter)
        [PROPS, STVAR, F1_INT, D_GLOBAL] = Foundation(TEXTFILE1, TEXTFILE2, ID, U1);

        F1_GLOB_4 = F1_GLOB([1 2 4 5]); % Global force vector in 4 DOF Format
        F1_INT_4 = F1_INT([1 2 4 5]); % Change 6 DOF to 4 DOF Format
        U1_4 = U1([1 2 4 5]); % Change 6 DOF to 4 DOF Format

        res = F1_GLOB_4 - F1_INT_4; % Residual force
        dU = D_GLOBAL \ res; % Displacement increment
        U1_4 = U1_4 + dU; % Update displacement

        % Update the global displacement vector
        U1([1 2 4 5]) = U1_4;
        Disp = U1;

        iter = iter + 1;
    end

    if iter >= max_iter
        warning('Newton-Raphson did not converge within the maximum number of iterations.');
    end

    % Data storage for later writing to a text file
    Write_Data(i, :) = [Fx(i), Fy(i), U1_4(1), U1_4(2), U1_4(3), U1_4(4)];

    % Store data for plotting (optional)
    Force_Disp_Fx(i, 1) = U1_4(1);
    Force_Disp_Fx(i, 2) = F1_GLOB_4(1);

    Force_Disp_Fy(i, 1) = U1_4(2);
    Force_Disp_Fy(i, 2) = F1_GLOB_4(2);


    fprintf(fid1, '%12.3e %12.3e %12.3e %12.3e %12.3e %12.3e\n', Write_Data(i, :));
end
```